WAPD-TM-628
AEC RESEARCH AND
DEVELOPMENT REPORT

BEHAVIOR OF AN INTENTIONALLY DEFECTED FUEL ROD WHICH RUPTURED DURING IRRADIATION

(ROD BETT 79-64D)

(LWBR Development Program)

JULY 1969

CONTRACT AT-11-1-GEN-14

BETTIS ATOMIC POWER LABORATORY, PITTSBURGH, PA.,
OPERATED FOR THE U. S. ATOMIC ENERGY COMMISSION
BY WESTINGHOUSE ELECTRIC CORPORATION

UC-25: Metals, Ceramics, and Materials
Special Distribution

BEHAVIOR OF AN INTENTIONALLY DEFECTED FUEL ROD WHICH RUPTURED DURING IRRADIATION (ROD BETT 79-64D)

(LWBR Development Program)

B. A. Hersey
H. B. Meieran

July 1969

Contract AT-11-1-GEN-14

Printed in the United States of America
Available from
Clearinghouse for Federal Scientific and Technical Information
National Bureau of Standards, U. S. Department of Commerce
Springfield, Virginia 22151
Price: Printed Copy $3.00; Microfiche $0.65

NOTE

This document is an interim memorandum prepared primarily for internal reference and does not represent a final expression of the opinion of Westinghouse. When this memorandum is distributed externally, it is with the express understanding that Westinghouse makes no representation as to completeness, accuracy, or usability of information contained therein.

BETTIS ATOMIC POWER LABORATORY, PITTSBURGH, PA., OPERATED FOR THE U. S. ATOMIC ENERGY COMMISSION BY WESTINGHOUSE ELECTRIC CORPORATION

SPECIAL EXTERNAL DISTRIBUTION (UC-25)

	No. Copies
AEC Library, Washington for J. M. Simmons	1
Ames Laboratory (AEC)	2
Argonne National Laboratory (AEC)	9
Atomics International (AEC)	4
Babcock and Wilcox Company (AEC)	2
Battelle Memorial Institute (AEC)	2
Battelle-Northwest (AEC)	6
Brookhaven National Laboratory (AEC)	2
Bureau of Mines, Albany (INT)	1
Combustion Engineering, Inc. (AEC)	1
Combustion Engineering, Inc. (NRD) (AEC)	1
Du Pont Company, Aiken (AEC)	4
Gulf General Atomic Incorporated (AEC)	2
General Electric Company, Cincinnati (AEC)	2
General Electric Company, San Jose (AEC)	2
IIT Research Institute (AEC)	1
Knolls Atomic Power Laboratory (AEC)	3
Lawrence Radiation Laboratory, Livermore (AEC)	2
Los Alamos Scientific Laboratory (AEC)	3
Mound Laboratory (AEC)	1
Oak Ridge National Laboratory (AEC)	5
Westinghouse Electric Corporation (AEC)	1
DTIE	3
Manager, PNR	3
Manager, PNR, Attention: H. Hughes for AECL	2
Total	65

CONTENTS

TABLES

FIGURES

An intentionally defected Zircaloy-4 clad ceramic pelleted fuel rod (BETT 79-64D) was irradiated in the ETR reactor L-12 loop to a depletion of 8 x 10^{20} fissions/cc. This work was done as part of the LWBR/LSBR fuel element development program. This rod was intentionally defected with a 0.0062-inch diameter defect hole located near the top of the rod. The ZrO_2 + 29.6 w/o U^EO_2 fuel material in this rod was in the form of combined-void-volume pellets. The rod failed after 121.2 EFPD of test operation. The purpose of the defect hole was to provide information regarding the effect of defect operation on the performance of a fuel rod with respect to cladding stability, waterlogging potentials, hydrogen pickup in the cladding, and corrosion behavior of an irradiated ceramic fuel material. The post-irradiation examination of this rod and evaluation of its irradiation behavior are described in this report.

BEHAVIOR OF AN INTENTIONALLY DEFECTED FUEL ROD WHICH RUPTURED DURING IRRADIATION (ROD BETT 79-64D)

(LWBR Development Program)

B. A. Hersey
H. B. Meieran

I. INTRODUCTION

The L-12 irradiation test was designed as part of the Bettis Laboratory LWBR/LSBR Fuel Element Development effort. The test was designed as a screening test in which Zircaloy-4 rods containing four fully enriched fuel materials in four pellet geometries were to be irradiated at high heat fluxes within the ETR L-12 loop. The fuels that were compared were of the following nominal compositions: ZrO_2 + 29.6 w/o U^EO_2; ThO_2 + 20.5 w/o U^EO_2; ZrO_2 + 6.1 w/o CaO + 33.2 w/o U^EO_2 and; serving as a control, UO_2 (17.7 w/o U^{235} in total uranium). Because of the high depletion objective, 25 x 10^{20} fissions/cc compartment, substantial void volume was incorporated within the fuel pellets to accommodate the irradiation induced swelling.

Four methods of including the porosity within the pellets were investigated, and the resulting configurations are shown in Figure 1. The methods were: (1) to uniformly distribute the void within the fuel in solid low density pellets, (2) to distribute the void axially within the pellets in annular pellets, (3) to distribute the void incrementally near pellet interfaces in dished-end pellets,

and (4) to distribute the void volume in a combination of all three preceding locations. This void volume was in addition to the modest diametral and axial void space normally allowed for thermal expansion and assembly tolerances. The evaluation of highly fission depleted PWR 2 Seed 1 type ZrO_2 + (26 to 47) w/o $U^E O_2$ ceramic fuel materials indicated that an irradiation induced growth of 0.7 percent $\Delta V/10^{20}$ fissions/cc could be expected in plate type fuel elements (Reference 1) operated to peak steady-state temperatures of 2500 F and a hydrostatic pressure of 2000 psi. Based on this assumption a pellet void volume of approximately 17.5 percent (0.7 percent $\Delta V/10^{20}$ fissions/cc x 25 x 10^{20} fissions/cc) was selected for these elements to accommodate anticipated irradiation induced fuel swelling at the intended burnup. (It should be noted that fuel swelling is now considered to be highly temperature dependent, and volume increases will be greater than 0.7 percent $\Delta V/10^{20}$ fissions/cc at temperatures greater than $\approx$2500 F.) The four pellet configurations of Figure 1 were fabricated to include void volumes equal to or greater than this amount.

The U^{235} content was adjusted in the various compositions and geometries to provide a common nominal loading of 35 x 10^{20} U^{235} atoms/cc compartment which includes the volume of the fuel, associated void, and fuel-sheath gap for the height of the fuel stack.

Test rod BETT 79-64D was intentionally defected with a 0.0062-inch diameter defect hole located near the top of the rod (in the plenum chamber region incorporated for the storage of fission gases in a nondefected rod). During the irradiation period of this rod, it was noted that bulging was occurring near the top of the rod where the fission gas plenum chamber was located. This bulging was attributed to a waterlogging type phenomenon in which the steam within the rod cannot escape in a sufficiently short time and causes the ceramic material to fragmentize and/or causes the cladding to bulge. Eight days after the rod had been reinserted into the L-12 loop with a 0.022 inch diametral increase in the plenum chamber region, the cladding of the rod ruptured in the bulged region.

Nondestructive (neutron radiography) and destructive examination revealed the fragmentation of one or more fuel pellets at the top of the fuel stack and some fuel redistribution. Some of this fragmented fuel material may have been periodically lodged within the internal surface of the defect hole, thereby blocking the free passage of the existing steam. A computer program, GLUB-1, (Reference 11) indicated that the defect hole had to be plugged to a diameter of less than 0.0001 inch before excessive stresses would develop within the rod. Metallographic examination also indicated that the ceramic material had been operating in the molten state for some time during its initial irradiation period. The

original annulus was no longer present. There did not appear to be any areas of massive hydriding in the rod although localized regions of the cladding did exhibit hydrogen concentrations of up to 500 ppm.

II. DESCRIPTION OF FUEL ELEMENT

A. Fuel

Powders of appropriate ZrO_2 and U^EO_2 proportions were mixed and prepared by Bettis Laboratory, as shown in the process flow diagram in Figure 2. The mixed powder was then agglomerated with 3 1/2 w/o Carbowax 6000 and 40 w/o Oxylene M-6. This mixture was screened to -12, -30, and -40 mesh sizes and oven dried for 2 hours at 122 F (50 C). The product was then blended with a mixture of 1 part -120 mesh Emersol 132 and 3 parts Methocel cps 4000 which had been screened to -120 mesh and pressed into pellets. The green pellets were given a CO_2 pretreatment in Inconel boats at 1652 F (900 C) for 3 hours and were sintered in molybdenum boats for 14 hours in a 3137 to 3182 F (1725 to 1750 C) dry hydrogen atmosphere. The pellets were centerless ground to a diameter of 0.2120 ± 0.0005 inch, and the pressed pellet lengths were 0.212 inch; thus the length-to-diameter (L/D) ratio was 1:1. The complete fabrication process outline is shown in Figure 3. Chemical analysis of a representative ZrO_2 + 29.6 w/o U^EO_2 pellet is given in Table A-1 of Appendix A and photomicrographs of the fuel structure are shown in Figure A-1. The fuel pellets had an average vacuum density of 92-percent theoretical density (T.D.), with 5.2-percent open porosity. The total void volume, including the center hole and dishes, was 13.2 percent. The fissile material loading was 42.5×10^{20} U^{235} atoms/cc of fuel. A summary of the pre-irradiation dimensional and weight data for the 38 pellets in rod BETT 79-64D is given in Appendix A, Table A-2.

B. Tubing and End Caps

Annealed Zircaloy-4 tubing was purchased to the ASTM-B-353-62 specification. The dimensions were 0.2173-inch ID with an 0.0177-inch wall. The inside of the tubing was pickled and the tube was annealed at 1450 F for 4 hours to minimize residual cold work from the final draw. Typical Zircaloy structures from an unirradiated tube are given in Figure A-3. The grain size range was ASTM numbers 6-8. The principal characteristics of the tubing are listed in Table A-3. The material properties for the Zircaloy-4 end caps are given in Table A-4.

C. Fuel Element

A total of 38 pellets, each with a nominal length of 0.212 inch, were loaded into the Zircaloy-4 tubing in a helium atmosphere. An axial plenum of 1.195 inches or 13 percent of internal rod volume, was included to accommodate 100 percent of the released fission gases in a nondefected rod without causing any clad deflections. As-fabricated characteristics of the pellets are listed in Table A-2. The range of pellet diameters was 0.2120 to 0.2128 inch and the tube ID was 0.2173 inch; the fuel clad diametral gap ranged from 0.0045 to 0.0053 inch along the fuel column. The end caps were welded to the tube in a 14.7-psi helium atmosphere and then machined to dimensions illustrated in Figure 4. The final fuel rod was 11.20 inches long.

The loaded rod was helium leak tested, corrosion tested for 3 days in 680 F, 2700-psi water, intentionally defected with a 0.0062-inch hole, and then corrosion tested for one additional day in 680 F, 2700-psi water. The rod was then Vidigaged for wall thickness, radiographed, and replicated. Diameter measurements were taken along the length of the rod at discrete elevations along two axes using a DR-25B optical micrometer and 0.125-inch diameter flat anvils (Reference 2). The locations of the diameter measurements are illustrated in Figure B-1 in Appendix B. Length measurements were taken with an ultramicrometer (Reference 2). A compilation of pre-irradiation measurements is given in Table B-2, Appendix B. A photograph and radiograph of the unirradiated rod are presented in Figure 5 along with a summary of the as-fabricated parameters.

III. DESCRIPTION OF TEST ASSEMBLY AND ENVIRONMENTAL CONDITIONS

A. Test Assembly

Rod 79-64D was placed into a holder designed for the 2000 psi pressurized water L-12 loop of the Engineering Test Reactor (ETR) at the National Reactor Testing Station (NTRS), Idaho. The failed rod, BETI 79-64D, was located in the "N" radial position of holder number 1 at the bottom of a multitiered test train. The holder assembly is illustrated in Figure 6. Radial orientation of the 10 rods in the holder assembly was maintained by the spired and wedged type end caps (Figure 4), and Inconel-X springs were placed on each of the fuel rods. Although there was an initial compressive load imposed on all spring collars, which were located 0.5 inch from the top shoulder of the rod, the spacing between the rods was not dependent upon the collars which were mutually contacting.

Holders within the test train were shrouded with hafnium-Zircaloy alloys of varying hafnium contents to maintain the design thermal conditions. The

shrouds for holder number 1 of the test train in which rod BETT 79-64D resided, were 100 v/o Hf + 0 percent Zircaloy and 40 v/o Hf + 60 v/o Zircaloy as shown in Table 1. The two shrouds were used to program heat flux levels.

B. Loop Environmental Conditions

Typical design environmental conditions for the L-12 loop are given in Table 2. The test was irradiated in pressurized water (2000 psi) at temperatures ranging from 325 to 510 F.

IV. IRRADIATION HISTORY AND ACTUAL TEST CONDITIONS

A. Chronological History

Rod BETT 79-64D was placed into test in the L-12 loop of the ETR reactor at NRTS, Idaho in June 1964, during the ETR Cycle-64 shutdown. During the subsequent irradiation testing program, rod BETT 79-64D was periodically examined during reactor shutdowns (see Tables 1 and B-1). The examinations were conducted to characterize the dimensional and visual performance of the rod during its irradiation period. The irradiation of rod BETT 79-64D continued satisfactorily until March 1965, when it was removed because of a 0.022-inch swelling in the plenum chamber region noted during an interim examination. Total exposure at this time was 112.4 effective full power days (EFPD). A complete nondestructive examination was made at Bettis Laboratory at this time, including neutron radiography.

Following this examination; rod BETT 79-64D was reinserted into the L-12 loop test during the ETR Cycle 75 shutdown on September 13, 1965, to obtain more data on the operation of an intentionally defected rod.

At 4:12 A.M. on October 9, 1965, a large activity burst was noted in the L-12 loop 2.1 hours after a startup in which the ETR was being returned to power from a midcycle shutdown. At the time of the activity burst the ETR power level had been increased from 60 Mw (34.3 percent) to 80 Mw (45.8 percent). After reaching 175 Mw at 7:26 A.M., the ETR ran at full power for 3.73 hours (to 11:10 A.M.) before being scrammed. The reactor was returned to partial power at 11:24 A.M. with accompanying high levels of activity in the L-12 loop. After operating at 100 to 106 Mw for 6.55 hours, the reactor was scrammed at 5:57 P.M. and the L-12 loop test was removed from the ETR. A complete power history of ETR at the time of the failure of rod BETT 79-64D is illustrated in Figure 7. Total exposure at the time of failure was 121.2 EFPD. Upon examination of the test train, it was found that the bulged area in the plenum region of rod BETT 79-64D

effective full power days

had developed a cladding split 1.5 inches long. The failed specimen was immediately returned to Bettis Laboratory, where a complete destructive examination of the rod was performed.

B. Radiochemistry

Radiochemistry data are gathered in the form of standard water sample surveys, continuous gamma monitoring, gross β-γ (before ion exchange column), gross iodine (before and after ion exchange column), and Cs^{138}. Figure 7 illustrates a comparison between the activity levels in the L-12 loop in the presence of an intentionally defected rod specimen for a normal reactor startup and one with a failure. The L-12 and M-13 loops shared a common water system; thus activity levels from samples in the L-12 loop were correspondingly illustrated in the M-13 loop.

The gamma monitor chart shows a small sharp peak in the activity of the L-12 loop during a normal startup and during subsequent reactor power transients. These peaks are caused by the emission of some fission products through the intentional defects of three rods which were in test in the L-12 loop. Very severe activity bursts (higher by one order of magnitude) occurred in the L-12 loop during reactor power transients with the failure (clad rupture) of a fuel rod.

C. L-12 Loop and Rod BETT 79-64D Thermal, Hydraulic, and Chemistry Conditions

The cycle average heat fluxes of the peak and average positions for rod BETT 79-64D are given in Table 1 along with accumulative compartment burnup (fissions/cc) and integrated fast neutron flux (>1 Mev). The burnup and heat flux histories, which are illustrated in Figures 8 and 9, are based on L-12 loop calorimetric data. Rod BETT 79-64D experienced 93 ETR reactor power transients to and from zero power.

A tabulation of bulk water and average clad surface temperatures for each cycle of operation is given in Table 3.

D. Interim Examinations

A total of four interim examinations was performed on rod BETT 79-64D at the Expended Core Facility (ECF) at the NRTS prior to its failure (Table 1), and one post-shutdown examination was conducted at Bettis Laboratory. These examinations included visual and dimensional examination, gamma scanning, neutron radiography, and leak testing (Table B-1). A tabulation of all interim and post-irradiation dimensional data can be found in Appendix B. Rod diameter

and length measurements were taken with the same type of instruments used for the pre-irradiation data (Section II.C). The location of each of the diameter measurement points is given in Figure B-1.

V. EVALUATION OF DATA

A. Visual Examinations and Observations of Loss of Fuel

During each interim examination, and the final post-irradiation examination, the rod was visually examined under a stereo microscope for any surface defects. The only visible change in the rod noted during the first three examinations was the formation of a small flow pattern around the defect hole and some light crud deposits. A typical photograph of the defect hole is illustrated in Figure 10. There was no apparent visible bulging in the vicinity of the defect hole during this period. During the examination which took place at ECF after the end of ETR cycle 70A on March 8, 1965, a bulged region was noted under the spring collar near the top of the rod; this corresponded to the elevation of the plenum chamber region (Figure 11). A black flow pattern around the defect hole and the presence of heavy corrosion buildup around the collar region was also noted at this time (Figure 11). The rod was returned to Bettis Hot Laboratory for further examination, and the ECF observations were confirmed (Figure 12). There appeared to be a whiter corrosion film on the clad surface under the collar than that noted over the rest of the rod. There was no discernable weight loss of the rod as determined by weight measurements and, therefore, no significant loss of fuel.

Rod BETT 79-64D was returned to test in September, 1965, and subsequently failed on October 9, 1965. Initial visual examination at ECF (Figure 13) noted a 1-inch long rupture in a severely bulged region of the rod with several pieces of fuel wedged in the cladding rupture. Figure 14 shows the condition of the rod after arriving at the Bettis Hot Laboratory. All but one large piece of fuel, which was originally observed wedged in the cladding rupture, was lost during subsequent handling. The rupture did not extend all the way to the intentional defect hole which is visible below the Inconel-X collar. Additional examination revealed no further cladding breaks.

B. Dimensions

The location of the diameter measurements for rod BETT 79-64D, which were taken in 12 positions along each of 2 axes (90 degrees to each other), are illustrated in Figure B-1. Diameter measurements were taken with the DR-25B optical micrometer, as in the case of the unirradiated rod, at elevations corresponding to the bottom

end cap, the as-fabricated center line of pellets 4, 8, 12, 16, 20, 24, 28, 32, 36, and 38, and the plenum chamber. The diameter measurements, which were corrected for clad surface temperatures (α_{Zirc} = 3.6 x 10^{-6} in/in/°F), are presented in Tables B-2 and B-3 and are illustrated in Figure B-2. The measurements have an accuracy of ±0.00020 inch. Diametral changes are illustrated in Figure 15 as a function of position and in Figure 9 as a function of burnup. Diameter measurements over the plenum chamber region were not taken during interim examinations since the Inconel-X collar was located over position number 12. Length measurements were taken at 90 degree rotations of the rod with a remotely controlled ultramicrometer, as in the case of the unirradiated rod, and have an accuracy of ±0.00050 inch. The length measurements are given in Table B-4 and the length changes are illustrated in Figure 16 as a function of exposure time (EFPD) and integrated fast neutron flux exposure time (nvt for neutrons having an energy of >1 Mev) and in Figure 9 as a function of burnup. Length measurements were also temperature corrected.

The diameter changes for rod BETT 79-64D in the cladding over the fuel stack (positions 2 through 11 at elevations of 1.81 to 9.01 inches) ranged from -0.0007 to +0.0024 inch (Table B-2 and Figure 15) prior to the time that the bulge was first noted over the plenum chamber in March 1965. Although the average diameter change during this first 88.5 EFPD irradiation period was generally less than +0.0010 inch, there was a slight indication of a progressive increase in rod diameter, with the maximum changes occurring in the upper fuel stack elevations (Figure 9). Maximum changes in the cladding over the top pellet (number 38) increased from +0.0003 to +0.0024 inch ΔD. Significant diameter changes were noted over the whole fuel stack in March 1965. Since the bulge was located at axial position number 12 (9.71 inches from the bottom of the rod) and under the Inconel-X collar, a diameter measurement was not possible at ECF. A measurement at Bettis Laboratory after the collar had been removed indicated that the diameter increase at position number 12 was 0.0097 inch. Since this change did not appear to be the maximum over the bulge, additional DR-25 measurements were obtained which indicated that the diameter increase over the bulge was up to +0.0216 inch. These measurements are further discussed and tabulated in Appendix B, Table B-3. Recording profilometer measurements also indicated that the diameter change over the bulge was in excess of +0.0200 inch and that it was circumferentially uniform and limited to the plenum chamber region (Figure 17).

The diameter change after the clad rupture occurred was similar to that measured prior to failure. The average diameter change after failure was +0.0015 inch ΔD. Again diameter measurements over the bulge and ruptured region were not

obtained, since it was impossible to remove the Inconel-X collar. Measurements from a photograph did indicate, however, that maximum diametral changes of up to +0.045 inch (18-percent circumferential strain) had developed. This estimated change included the subtraction of the crack width.

The length changes for rod BETT 79-64D exhibited a continuous increase for the first 79 EFPD's of irradiation to an average burnup of 5.8×10^{20} fissions/cc (Figure 16). The length appears to have decreased thereafter until and after rod failure occurred. The length change was caused by two components: (1) the irradiation induced growth of Zircaloy and (2) fuel-clad interactions. Kreyns* has found that the irradiation induced growth of annealed Zircaloy tubing saturates out at approximately 0.06 percent $\Delta\ell$ at an integrated fast neutron flux exposure of 10×10^{20} nvt. It appears that the measured residual axial strain for rod BETT 79-64D largely reflects the irradiation induced growth, since a maximum length change of 0.011 inch, or 0.1 percent $\Delta\ell$, was reached after an integrated fast neutron flux exposure of 13×10^{20} nvt. The effect of fuel-clad interactions was probably minimized, since the fuel material, as it will be shown later, was largely molten and very plastic; therefore, a minimum fuel-clad contact frictional force would be expected during the early stages of irradiation. The rod decreased in length after the second interim examination until the bulging and subsequent rod rupture occurred. The final length change was -0.020 inch or a net decrease of -0.026 inch (-0.3 percent $\Delta\ell$) from the previous examination before failure.

Assuming constant volume, the sum of the strains in the radial, circumferential, and the axial directions can be set equal to zero or:

$$\text{radial strain} + \text{circumferential strain} + \text{axial strain} = 0.$$

It can be seen that the decrease in length of -0.3 percent $\Delta\ell$ is quite possible, since a considerable diameter change (+18 percent) and a finite amount of clad thinning (up to -18 percent or approximately 0.004 inch) occurred.

Bow measurements were frequently taken during interim examinations. The measurements were taken with the DR-25B optical micrometer using one anvil. The method of measurements is described in Reference 18. The measurements, which were taken on both diametral measurement axes, indicated maximum bows of up to 0.014 inch after the first bulge was noted. Furthermore, there did not appear to be any significant levels of bowing even after the clad rupture occurred (Figure 14). The largest axial expansion was noted during the second interim

*P. H. Kreyns, Bettis Atomic Power Laboratory.

examination; at this time the largest axial and thrust between the rod and the holder would be expected. The presence of large axial end thrust along with a large radial thermal gradient have been known to promote significant bowing in fuel rods. A treatment by Newman of the thermal gradient bowing of rod type fuel elements subjected to an axial thrust is presented in Reference 18. The absence of a large radial thermal gradient in rod 79.64D along with no significant axial end thrust probably did contribute to the lack of bowing in the rod. The bulge at the top of the fuel rod was uniform (Figure 17) and significant differential circumferential stresses would not be present to increase the degree of bowing.

C. Gamma Scans

In order to determine the overall condition of the fuel rod and the extent of any axial fuel redistribution, continuous or point-count gamma scans were obtained along the fuel rod length. The specific gamma energy examined during the scans was the 1.59 Mev Ba^{140}/La^{140} gamma ray. Figure 18 illustrates the gamma scan traces obtained during the various examination periods.

The scan made during the first examination after 10 EFPD of operation shows peaks of activity which were not apparent during examinations 2, 3, or 4. During the Bettis Laboratory examination (number 5) after March 8, 1965, three scans (using gross activity) were obtained (Figure 19). The top scan was the first and is nearly identical to the scan obtained at ECF on March 8, 1965, except for a sharp peak at the top of the plenum chamber indicating the presence of fuel material and/or fission products. The rod was tapped in an attempt to move the fuel to the top of the plenum chamber. The trace indicated by a dashed line confirmed the fact that the fuel had moved into the plenum chamber. A neutron radiograph taken after the scan of March 25, 1965, did not indicate the presence of fuel at the upper end of the plenum chamber (Figure 20).

The final gamma scan (Figure 18) taken after the failure of the element still indicated the presence of fuel material at the upper end of the plenum chamber, as well as the fragments observed in the cladding rupture (Figures 13 and 14). The scan indicated less activity in the plenum chamber region than prior to the failure, thus indicating the loss of some fuel material. This observation was confirmed by the fact that three pieces of fuel were visibly wedged in the crack when the rod was examined at ECF, whereas the Bettis Laboratory examination noted only one small piece of fuel in the crack (Figure 13).

Metallography of the upper fuel region and the plenum chamber confirmed the observations made from the gamma scans (Section V.F.1). It thus appears that at least one whole pellet at the top of the fuel stack was entirely fragmentized.

Large pieces of fuel were allowed to move without restriction in the plenum chamber. It appears that the peaks noted during selected examinations reflect only the periodic movement of fuel within the plenum chamber. Steam would further disrupt the fragmented fuel, and the probability of fuel migration into the plenum chamber would increase.

It is significant that the dishes at the pellet-to-pellet interfaces were present only in the low fuel stack elevations after the first interim examination. This indicated that significant levels of dish closure had occurred, since high fuel temperatures were encountered which were probably above that required to cause melting. The dishes seem to have been completely lost after the second cycle of irradiation, during which the rod was exposed to higher heat flux levels (Table 1).

D. Neutron Radiography

A neutron radiograph was taken of rod BETT 79-64D prior to being reinserted into the test for ETR Cycle 75A. The radiograph (Figure 20) was obtained at Battelle Memorial Institute in Columbus, Ohio, and employed the transfer technique developed by Battelle (Reference 4). Broken fuel was seen to have accumulated at the top of the plenum chamber and thus verified the observation made from the gamma scans. Fuel particles were observed clinging to the internal cladding surfaces just above the top of the fuel stack. No as-fabricated dishes were found at the ends of the pellets; it is felt that the dishes were closed by fuel melting. A central void or core was also present at the top of the fuel stack. This core did not have the original dimensions of the as-fabricated center hole and probably resulted from the redistribution of molten fuel material. The dimension of the core, as measured from the neutron radiograph, was 0.100 to 0.150 inch and the fuel wall thickness ranged from 0.015 to 0.060 inch. The as-fabricated pellets had 0.063-inch diameter cores and a 0.074-inch thick fuel wall. The overall length of the fuel stack decreased from 8.050 to 7.874 inches. The decrease in length verified the gamma-scan analysis of the fragmentation and redistribution of at least one fuel pellet from the top of the fuel stack. Metallographic examination (Section V.F.1) shows that the region of the radiograph which appeared as a hole or core was in actuality occupied by a very porous material.

E. Radiochemistry

Five radiochemical burnup samples were taken from the rod at the locations illustrated in the general cutting sketch in Figure 21. These samples can be distinguished from other samples by the B prefix, B6, B13, etc. The

numerical part of the alpha-numeric code indicates the pellet numbers from the elevations of the unirradiated fuel stack.

The samples were analyzed by mass spectroscopy. Burnup values that were calculated from the analytical data showed a capture-to-fission ratio that was much larger than was expected. In order to determine and correct for U^{238} depletion, the samples were reanalyzed and the total uranium contents were obtained by isotopic dilution. Some low precision plutonium isotopic analyses were also obtained on two samples. The precision of these analyses was adequate for estimating a correction term for the depletion of U^{238} during irradiation.

These data were combined with the mass spectrometric data to estimate the depletion of U^{238} in the two samples. A straight line was obtained when these two values and the zero (pre-irradiation) value were plotted against U^{236} content. Estimates of the U^{238} depletion for the other samples were then obtained from this line. The burnup values, corrected for U^{238} depletion, are shown in Table 4.

The amount of plutonium formed during irradiation is much greater than was expected. Beyond the fact that the rod contained steam and the fuel did appear to experience extensive melting, there are no other known peculiarities in the nuclear characteristics of the irradiation history to explain the large plutonium content of the samples. The data appears to be internally consistent, so that the general shape of the burnup profile (Figure 22) is probably valid although its quantitative accuracy is questionable. A comparison of the radiochemical depletion data and that inferred from the calculated thermal data (Table 1) indicates that a peak burnup of only 2/3 of that calculated was obtained. Although the measured depletion values were lower, they do not have any major effect on the evaluation of the performance of the fuel rod.

F. Metallographic/Autoradiographic Examination

The metallographic analysis was directed primarily toward an analysis of the cladding in the failed region. A secondary metallographic analysis was directed toward the fuel material. The general cutting sketch (Figure 21) outlines the areas which were examined metallographically.

The experimental technique for metallographic and autoradiographic examination consisted of the following operations:

(1) Pressure mounting the sample in high temperature hysol.
(2) Inserting the mounted sample into a steel rim.
(3) Grinding the sample down approximately 0.020 inch and polishing so that a proper viewing surface could be obtained.

(4) Exposing the sample to a high resolution plate for two to four seconds to obtain a β-γ autoradiographic record of the fission product distribution.

(5) Etching the Zircaloy-4 cladding material with a 60 cc H_2O_2 + 40 cc HNO_3 + 8 drops HF solution to develop the cladding structure and hydride distribution.

(6) Pickling the cladding down 0.050 to 0.080 inch using 50 cc H_2O + 45 cc HNO_3 + 5 cc HF.

(7) Filling the gap where cladding was removed (Step 6) with high temperature hysol.

(8) Minimum grinding to prepare surface for metallographic observations.

(9) Viewing in as-polished condition.

(10) Viewing in fuel etched condition. The etchant was concentrated hot ammonium fluoride and the etching times ranged from four minutes to three hours and 39 minutes.

1. Fuel Region

Four metallographic samples were taken from the fuel stack region of the rod. The purpose of examining these samples was to determine: (1) if melting had occurred, (2) the depth of any remaining dishes at the ends of the pellets (not observable on the radiograph), (3) the quantitative extent of a central void which was noted on the neutron radiograph, (4) the amount of broken fuel present which would account for the large changes in the activity profile noted by gamma scans, and (5) if any fuel-clad reaction or internal clad corrosion had influenced the failure of the rod.

The general appearance of the fuel is illustrated in Figure 22 where it can be seen that there was extensive cracking in a material that was both very porous and dense. The original annulus (0.063-inch ID) could not be seen in its as-fabricated form. There also appeared to be some fuel redistribution. Fragmented fuel was found near the top of the fuel stack. A thick oxide was present in the interface between the fuel and the clad.

A longitudinal section was taken through pellets 33, 34, 35, and 36 which were at the top of the fuel stack. Figure 22 shows the orientation of this sample in relation to the orientation of the other samples as well as the burnup profiles of the fuels. All four pellets in this region were fractured and consisted of many discrete pieces, as illustrated in Figure 23. It thus appears that steam easily displaced the fractured fuel material from its normal position at the top of the fuel stack to the plenum chamber.

A transverse metallographic sample taken at an elevation corresponding to Pellet number 19 revealed a radially cracked material with a porous central region. An as-polished photomicrograph and autoradiograph showing fission product distribution is shown in Figure 22. After the fuel was etched for 22 minutes with hot ammonium floride, three distinct bands were visible, each separated by a black ring (Figure 24). The outermost large band has a rim of 0.0023-inch wide cracked fuel between it and the clad. This rim appears to be a combination of fuel and ZrO_2 formed by the exposure to water and/or by the reaction of hot fuel upon the cladding material. The band of fuel itself appears to have undergone a microscopic transition in that its etching characteristics were not the same as the rest of the fuel material. There are large pores at the outside edge of the fuel similar to those seen in ZrO_2+UO_2 or ZrO_2+UO_2+CaO fuel materials that had been molten during irradiation (References 5 and 6). What appears to have once been a dense structure, again reminiscent of an area of melting, surrounds the large pores. It must be noted here that the phase transformation and densification that ZrO_2+UO_2 material undergoes during the initial stages of irradiation (References 1 and 18) may confuse the structures produced by possible melting. If it is assumed that melting occurred in regions near the pellet surface, as will be shown in Section V.G., a high density region would be expected. The presence of extremely fine pores in this region appears to indicate that melting had occurred in the area and further irradiation-induced fuel swelling decreased the size of the pores to that found during metallographic examination, or that small fission gas bubbles had formed.

The second inner band appears to be the final point of melting at another time during life. The nature of the thermally transformed material, however, did not permit etching that would produce clear grain structure. The sample was etched again for a total of 3 hours and 39 minutes, and an equiaxed grain type structure was developed throughout the center region. The as-fabricated 0.063-inch diameter annulus in the center of the fuel was found to be filled with a highly porous material. A higher density band, which again appears to represent a limiting distance of melting, was found at the outside edge of this porous region. Thus it would appear that the fuel experienced melting several times early in life.

An autoradiograph of this sample indicated the presence of high activity fission products in a ring around the high porosity center material (Figure 22). The porous center region contained no indications of activity, so that the fission products appear to have migrated from the molten or near-molten regions of the fuel to the cooler outside regions of the fuel.

Pellet 5 revealed structure similar to that seen in pellet 19 (Figure 25). However, due to lower fluxes in this region the postulated limits of melting were not as near to the pellet surface as in pellet 19.

The final metallographic sample examined in the fuel region was a longitudinal section taken at the bottom of the fuel stack which included pellets 1, 2, and 3. This sample exhibited the same basic structure as seen in the fuel pellet samples taken from the upper fuel stack elevations. The center contained a highly porous material, and the outer regions illustrated the two limits of melting possibly produced during the initial states of irradiation (Figure 26). The outermost region contained a high-density rim with the same network of fine fission gas pores and large pores near the clad. The bottom pellet has taken the characteristic "crucible" shape which has been seen in other rods that have seen fuel melting (References 5 and 6). The autoradiograph of this section again indicated insignificant activity levels in the highly porous center region of the sample (Figure 22). There appears to be an accummulation of fission products at the postulated limit of melting. Some highly active fuel was also present in the predrilled hole of the bottom end cap. This was residue left by the plastic fuel material displaced from the fuel stack.

2. Cladding Structure

Three metallographic samples were taken at various positions through the cladding failure, as illustrated in Figures 21 and 22. These samples were examined for hydride needle orientation and concentration, internal oxide formation, structural changes in the cladding material, and cracking patterns in the vicinity of the failure. Structural changes of the cladding material were specifically looked for, since similar rods experiencing molten fuel-cladding interaction had exhibited structural changes in the clad material (References 5 and 6). Inclusion of the intentional defect hole in a metallographic sample was not successful.

The first sample that was examined was the longitudinal section taken through the upper end cap. Fuel chips were found in the plenum chamber (Figure 22). Moderate amounts of hydride precipitates (Figure 27) were seen in both the alpha phase of the cladding and in the beta-quenched weld region of the end cap. The beta-quenched material was produced during fabrication when the end caps were welded onto the tube and temperatures in excess of 1525 F were produced in the adjacent tubing wall. The same type of structure was also noted at the bottom of the rod and was also produced when the bottom end cap was welded to the tube. The hydride needles were randomly oriented with a larger proportion concentrated

on the cooler surfaces of the clad. As can be noted in Figure 27, the interior of the clad is extremely irregular and had a "sandblasted" appearance. In Section V.C. it was shown that the fuel material was free to move within the plenum chamber region. It was also postulated that the steam caused the fuel to be displaced in the region during irradiation. It thus follows that the moving fuel abraded the internal cladding surface and caused the "sandblasted" appearance.

A transverse section taken through the cladding crack is illustrated in Figure 22 (Sample TE-T). The diameter increase (bulge) and clad thinning are both observed. The clad thickness varied from 0.013 to 0.016 inch with the thinner clad sections found near the fracture (the original clad wall thickness was 0.0177 inch). The resultant radial strains were up to 27 percent. The hydride precipitates were uniformly distributed around the circumference of the sample, with no apparent increase noted near the point of fracture. Figure 28 illustrates typical clad structures and hydride concentrations found near the cladding fracture. The greatest hydride precipitate concentrations appeared at the outer diameter, the cooler region of the cladding. There does not appear to be any differential hydride precipitate concentration close to or away from the cladding adjacent to the Inconel-X spring collar.

The fracture, as viewed in this transverse sample, appears to be quite similar to the ductile fractures seen in recent burst tests of Zircaloy-4 tubing (Reference 7). There were no observations of radially oriented hydride precipitates, nor were there any indications of brittle fractures that could have been associated with excessive hydrogen levels.

The third metallographic section (Sample D-L) was taken below the failed region and illustrates the transition from normal diameter to the bulge (Figure 22). The cladding wall thickness ranged from 0.013 to 0.015 inch in this sample. A series of planes was examined in the rod until the crack was reached in the cladding. The etched structure of the clad in the region where the crack appeared is shown in Figure 29. Though the zirconium hydride concentration is high, there appear to be no solid hydride formations present near or adjacent to the ductile fracture. The heavier hydride concentrations were located in the bulged region rather than at the nonbulged ends of the sample. Little radial variation in the hydride concentrations was observed. Further grindings failed to reveal the progression of the crack towards the intentional defect hole which would have been located near the bottom of the sample.

Examination of the cladding in the fueled regions of the rod revealed some hydride precipitates concentrated along the outer circumference of the rod.

A typical example of the clad in the fueled region of the rod is shown in Figure 30 for pellet 19. The polarized light photomicrograph has been included to clearly define the hydride concentrations along the outside diameter of the rod and to illustrate the alpha grain structure in the cladding material. It appears that the hydride rim was a result of the normal corrosion reaction of the steam with the internal clad surface. The amount of hydrogen in this rim does not indicate that massive hydriding had occurred within the rod prior to or after failure occurred.

Several samples were taken from the rod at various axial locations for hydrogen analysis (Figure 21). The results of these analyses are shown graphically in Figure 22 and indicate that concentrations of up to 239 ppm hydrogen were found away from the clad rupture. Metallographic estimates for the hydrogen (visual comparison of photomicrographs with those having known concentrations) in the failed region were approximately 400 to 500 ppm or almost double that analyzed from the rest of the rod.

A listing of the internal and external oxide measurements is given in Table 5. In some areas it was impossible to evaluate the extent of the internal oxide film due to corrosion since there appeared to be an interaction zone between the cladding and the fuel. The internal oxide in the plenum region was generally irregular as is shown in Figure 31. Utilizing a computer program to estimate weight gains for the in-pile duration of the rod, it was calculated that a corrosion film of 1.3μ would be formed under the actual operating conditions. A thicker oxide film of up to 4μ was observed. It is felt that higher temperatures for the clad surface or the presence of fission products and/or fuel material could have caused the higher oxidation rate (Reference 8).

G. Fuel Rod Thermal Performance

The equation for heat conduction in cylindrical fuel rods is given by Reference 9:

$$\int_0^r dr/r \int_0^r q(r)dr = \int_{T_{\mathfrak{C}}}^{T_r} k(T)dT \qquad (1)$$

where

r = radius of fuel

$q(r)$ = volume heat generation rate as a function of radius

T_r = temperature at radius, r

$T_{\mathfrak{C}}$ = temperature of pellet center line (℄)

$k(T)$ = thermal conductivity as a function of temperature.

This equation has been integrated to yield the heat rating model for cored pellets derived by Robertson (Reference 15):

$$\int_{T_a}^{Tb} k(T)dT = \frac{(Q/A)_a xa}{2} \left[\frac{Kb\ I,(K_1(Kb)J_o(Ka) + I_o(Ka)J_1(Kb) - 1}{0.5\ K^2 abI_1(Ka)J_1(Kb) - I_1(Kb)J_1(Ka)} \right] \qquad (2)$$

where

$k(T)$ = thermal conductivity of the fuel material as a function of temperature, watts/cm-°C or Btu/hr-ft-°F

$T_a, T_b, T_{\mathcal{L}}$ = temperatures at the fuel pellet surface, inner surface (annular pellets), and centerline (solid pellets), respectively, °C or °F

$(Q/A)_a$ = heat flux at fuel pellet surface, watts/cm^2 or Btu/hr-ft^2

a = fuel pellet outer radius

b = fuel pellet inner radius (annular pellets only)

K = reciprocal diffusion length, cm^{-1} or in.$^{-1}$

$I_o(Ka)$, $I_1(Ka)$ = First and second order Bessel Functions (respectively) of the first kind.

$J_o(Ka)$, $J_1(Kb)$ = First and second order Bessel Functions (respectively) of the second kind.

The Robertson heat rating equation was broken up into component parts by Lieberman* for all types of pellet geometry:

$$\int_{T_a}^{Tb \text{ or } T_{\mathcal{L}}} k(T)dT = (Q/A)_a \times \frac{a}{2} \times B_k \times B_g = (Q/A)_{OD} \times \frac{r_{OD}}{2} \times B_k \times B_g \qquad (3)$$

where

$(Q/A)_a$ and $(Q/A)_{OD}$ = heat flux at surface of pellet and surface of rod respectively

a = pellet outer radius

r_{OD} = rod radius

B_k = factor due to flux suppression

B_g = geometrical correction factor.

*R. M. Lieberman, Bettis Atomic Power Laboratory

For an annular pellet, cooled on the outside only, the geometrical correction factor is:

$$B_g = 1 - \left(\frac{2b^2}{a^2 - b^2}\right) \ln \frac{a}{b} \quad . \tag{4}$$

The thermal conductivity for a ceramic fuel can be expressed as (Reference 13):

$$K_p = \frac{1 - p}{1 + \beta p} \left[\frac{1}{A_o + BoT + \frac{No}{T} + \frac{Xo}{T} + \frac{FZo(1386)}{T}}\right] \tag{5}$$

where

K_p = thermal conductivity of the oxide fuel, Btu/hr-ft-°F

p = the fractional as-fabricated porosity

β = factor for the geometry of the pores. Values of 0.5 - 2.5 were used

A_o = temperature independent thermal resistance constant (phonon mean free path) = 0.787 hr-ft^2 - °R/Btu for all temperatures.

B_o = temperature dependent thermal resistance constant (phonon mean free path) = 0. hr-ft/Btu for all temperatures.

T = temperature in °R

$\left(\frac{No}{T}\right)$ = thermal resistivity due to the concentration of lattice defects caused by neutron damage at burnups of less than 10^{18} fissions/cc. N_o = 6.23 hr-ft^2-°R/Btu at T≤2732F and 0. at T>2732F

$\left(\frac{Xo}{T}\right)$ = thermal resistivity due to the concentration of lattice defects caused by fission damage at burnups of less than 10^{18} fissions/cc. X_o = 49.82 hr-ft-°R^2/Btu at T≤2732F and 0. at T>2732F

$\frac{Z_o\ F(1386)}{T}$ = thermal resistance caused by fission damage at burnups in excess of 10^{18} fissions/cc.

Z_o = 0.0139 hr-ft-°R/Btu at T≤2732F and 0. at T>2732F

F = fissions/cc x 10^{-20}

$\frac{1386}{T}$ = conversion from the 1392 R irradiation temperature of an in-pile thermal conductivity experiment to T, the temperature interest.

The various quoted values for the constants A_o, N_o, X_o, and Z_o were taken from Reference 13 for ZrO_2-UO_2 material except at temperature levels above 2730F. Since the small amount of data available above 2730F shows no clear temperature

dependency, the values of A_o and B_o are assumed to be constant for the whole temperature range. Also the values of N_o and X_o were zero at temperatures in excess of 2732F where it was assumed that the lattice defects caused by the neutron and fission damage were annealed out. Furthermore, the value of Z_o was also zero at temperatures in excess of 2732F where it was assumed that the solid fission products are precipitated out. The use of a 2730F annealing temperature is considered conservative even for high fission depletion levels. For example, recent experimental data by D. C. Jacobs of Bettis Atomic Power Laboratory has shown no differences between the in-pile and out-of-pile values of thermal conductivity for ThO_2 - UO_2 and UO_2, within experimental accuracy, for temperature ranges for 930 to 3300F at low burnup levels (10^{19} fissions/cc). This experimental evidence suggests that N_o, X_o, and Z_o have been overestimated in Reference 13. However, the values of N_o, X_o, and Z_o presented herein are considered to be the best estimates presently available. The values for the thermal conductivity and integrated thermal conductivity were computed by the FIGRO computer program (Reference 3) and are illustrated in Figures 32 and 33 respectively. A discussion of the interpretations of these values is given in more detail in Reference 6.

The temperature of the surface of the fuel pellet (T_a) can be calculated by:

$$T_a = T_{BW} + \Delta T_{film} + \Delta T_{clad} + \Delta T_{gap} \tag{6}$$

or expanding Equation (6):

$$T_a = T_{BW} + \frac{(Q/A)_{OD}}{h} + \left(\frac{(Q/A)_{OD} \times r_{OD}}{k_{clad}} \times \ln \frac{r_{OD}}{r_{ID}} \right) + \left(\frac{(Q/A)_{OD}}{c} \times \frac{r_{OD}}{a} \right) \tag{7}$$

and summing terms:

$$T_a = T_{BW} + (Q/A)_{OD} \left[\frac{1}{h} + \left(\frac{r_{OD}}{k_{clad}} \times \ln \frac{r_{OD}}{r_{ID}} \right) + \frac{r_{OD}}{ac} \right] \tag{8}$$

where

$(Q/A)_{OD}$ = heat flux at surface of fuel rod

k_{clad} = thermal conductivity of sheath material

T_a, T_{BW} = temperature at fuel pellet surface and bulk water, respectively

h = heat transfer coefficient between sheath and water

r_{OD}, r_{ID} = radius of outer sheath and inner sheath surfaces, respectively

a = fuel pellet surface radius

c = heat transfer coefficient between fuel and sheath.

Equation (8) can also be written in the form of:

$$\int_{T=0}^{T=T_a} k(T)dT \quad . \tag{9}$$

Thus, the center-line temperature can be calculated if the values of both Equations (3) and (9) are known and summed:

$$\int_{T=0}^{T=T_{\ell}} k(T)dT = \int_{T=0}^{T=T_a} k(T)dT + \int_{T=T_a}^{T=T_{\ell}} k(T)dT \quad . \tag{10}$$

The input parameters for the use of the FIGRO computer code consist mainly of the dimensions of the rod and fuel (Figure 5), loop environmental conditions (Table 2), the thermal power levels of the rod (Table 1), and thermal properties of the fuel and cladding material (References 7 and 13). The various input options were the porosity factor β (Equation (3)) and the calculations of the fuel/sheath gap conductance. The fuel/sheath gap conductance was the same as that used by Meieran (Reference 16) in a failed rod, or by the Ross and Stoute method (Reference 14) using the appropriate thermal conductivities of the standard water properties rather than that of helium (the welding medium) in the defected rod. The results of these calculations are illustrated in Figure 34 where it can be seen that extensive melting occurred in the fuel material. First of all, it was found that the value of β (geometry factor for porosity), which was varied in the calculations from 0.5 to 2.5 (spherical to elongated pores) did not have any appreciable effect upon the fuel center-line temperature although the conductivity could decrease up to 13.2 percent (see Equation (3)). It was also found that melting (4890 F) was calculated to have occurred near the outer surface of the fuel pellet for maximum heat fluxes in rod BETT 79-64D during its first two cycles of operation (40-percent hafnium shroud) irrespective of the value of the gap conductance. A quantitative comparison between metallographic and calculated estimates of the limit of melting was not possible for two reasons. First, the fuel had initially densified and undergone a phase transformation which would distort the molten fuel structure. Secondly, the

fuel material had undergone irradiation induced swelling for some time after the extensive melting had occurred. The heat rating for the rod ranged from:

$$\int_{T_a}^{T_\ell} k(T)dT = \frac{(Q/A)_{OD} \times r_{OD} \times B_g \times B_K}{2}$$

$$= 6500 \text{ Btu/hr-ft (62.6 watts/cm)}$$

for a heat flux of 1,747,000 Btu/hr-ft^2 and

$$= 2180 \text{ Btu/hr-ft (21.1 watts/cm)}$$

for a heat flux of 587,000 Btu/hr-ft^2

where B_K = 0.93 (factor due to flux suppression) as calculated from the analysis given in Reference 7 for the dimensions given in Figure 5 and the isotopic loadings for the fuel materials (U^{235}, U^{238}, Zr^{90}, and O^{16}).

$$B_g = 1 - \left(\frac{2\,b^2}{a^2 - b^2}\right) \ln \frac{a}{b} = 0.761 \quad .$$

Values of a (pellet outer radius) and b (pellet inner radius) were taken from Figure 5.

The equivalent linear heat ratings for rod BETT 79-64D were 33.8 kw/ft (1110 watts/cm) and 11.4 kw/ft (374 watts/cm) for the respective maximum and minimum heat flux levels.

VI. DISCUSSION

A. Mode of Failure - Waterlogging

Unbonded fuel elements are susceptible to waterlogging failures. Such failure occurs when the coolant enters the sheath interior through a defect hole, intentional or otherwise, during a reactor shutdown and then flashes to steam as the reactor is brought to power. If the defect becomes plugged, as is postulated in the present case, or becomes sufficiently closed, the internal pressures can cause clad deformation or rupture (Reference 9).

A Fortran-IV digital computer program (GLUB-1) has been developed for the analysis of waterlogged fuel elements (Reference 11). This program examines the possibility of excessive sheath distortion in a waterlogged fuel rod subjected to a power transient. Heat transfer, linear elastic stress and deformation, and fluid flow equations to yield transient values of internal pressure, clad stress, and clad strain are solved in the program. This program uses a model which divides a typical rod-type fuel element into two axial sections: a fuel section and a plenum section. The available water space in

the fuel rod is made up of four subvolumes: (1) the hollow core of the fuel pellets, (2) the internal volume of the plenum, (3) the gap between fuel pellets and clad, and (4) the lumped volume representing the porosity of the fuel pellets. The clad may contain a defect of arbitrary size (including zero) located in either the fuel section (gap defect) or the plenum section (plenum defect). A plenum defect was considered in the case of the subject rod, and the reactor power history encountered by rod BETT 79-64D during its last day of irradiation was programmed into GLUB-1. It was calculated that internal pressures and corresponding clad rupture stresses would be produced if the defect hole were closed to a diameter of less than 0.0001 inch. Figures 35 and 36 illustrate the resultant internal pressures generated within an intentionally defected rod during a simulated reactor startup (from zero power) and in which the defect hole is partially plugged (0.0001-inch hole) or completely plugged (0.0-inch hole). In the former case there is a sufficient hole size and time for the steam to escape after each power transient. In the second case the internal pressures continue to build up after each power transient until there is a sufficient stress to cause clad rupture.

Two types of waterlogging failures are discussed in References 9 and 10. The first type occurs in the presence of considerable open porosity in the fuel such that water can permeate the pores of the oxide during low power exposure. On approaching operating temperatures, the vaporization of water in the pores may fragment the oxide and project fragments with considerable force against the interior of the cladding. The second type of waterlogging occurs as a result of permeation of clearance and void space with water. The photograph of a waterlogged rod in Reference 10 (the failure of which has been attributed to fractured fuel) appears to be quite similar to the bulge and rupture noted in rod BETT 79-64D. It is therefore postulated that the first mechanism, combined with the high fuel temperatures (>4890 F) seen early in life, caused the gross fuel fracturing noted in several of the pellets of rod BETT 79-64D (Section V.G.). During subsequent reactor cycling these pieces of broken fuel, which were noted by both the gamma scans and neutron radiographs, could move into the plenum region, causing an abrading attack of the internal clad surface. This continued movement of mixing of fuel and steam over a period of time would cause a continual breakdown of the fuel particles into smaller and smaller particles. Therefore, it is highly probable that some of these particles were periodically trapped in the 0.0062-inch diameter defect hole, causing partial to full closure of the hole. Internal pressure would then cause deformation of the cladding, as indicated by the progressive diameter increases noted during the interim

examinations. It is postulated that such a mechanism was occurring but, as the internal pressure built up, the small pieces of fuel wedged in the defect became dislodged and permitted relief of the internal pressure of the rod. Figure 7, which is a comparison of a normal reactor startup in which a failure occurred, shows that during a normal startup a brief burst of activity has been recorded as the reactor power transients occur. These activity bursts have been attributed to the release of fuel particles and/or fission products from defected samples. Consequently, it is possible that the defect hole in rod BETT 79-64D periodically became plugged, the clad was deformed (as indicated by dimensional surveys), the hole cleared itself of the fuel particles (as indicated by the activity bursts noted on gamma monitoring devices), and the rod continued to operate normally until the next shutdown-startup cycle occurred. As the clad deforms and as the wall becomes thin, it would take less internal pressure to cause additional deformation. It is then not surprising that the rod diameter increased by 0.022 inch in the plenum region in the short exposure time of 24 EFPD after its third and prior to its fourth interim examination. Upon returning the rod to the L-12 loop test it only took an additional 8.8 EFPD to finally plug the hole to a diameter of less than 0.0001 inch (maximum diameter for hole if a waterlogging type failure were to occur) and rupture the already weakened cladding. Figure 9 indicates that there were eight shutdowns during the last cycle. Since the failure occurred on the seventh startup (Figure 7), there were seven chances for the above postulated mechanism to cause deformation of the clad to the point of failure.

B. Clad Structure

It has been stated in Reference 7 that "small amounts of precipitated hydrogen are detrimental to the properties only if the hydride platelets are radially oriented." In the region of the failure on rod BETT 79-64D, the hydride platelets were generally randomly distributed (Figures 28 and 29) although there was a slight tendency for circumferentially oriented hydride precipitates (Figure 37). It thus appears that there was no significant contribution of radially oriented hydride towards the decrease of the mechanical properties of the Zircaloy or with a resultant increased tendency for clad rupture when the sheath was strained.

There were no examples of solid hydride formation observed in any of the metallographic samples. This observation was contrary to that noted on other failed rods. It was generally found that massive hydride will occur along the internal cladding surface, or at least in the end caps, of almost all Zircaloy

sheathed ceramic pelleted rods which experience an in-pile clad rupture (References 5, 6, 12, 16, and 17). Massive hydride was also found on rods which were intentionally defected and which ruptured in-pile (Reference 12). The hydride platelets were evenly distributed through the cladding in the plenum chamber of rod BETT 79-64D where the failure occurred. In the fuel region, however, the hydride platelets appeared to be more concentrated at the outer clad surface in the fuel region (Figures 30 and 37). This second observation is consistent with the known thermal diffusion characteristics of hydrogen which will tend to migrate down the thermal gradient to the cooler part of the clad (Reference 12). A thermal gradient would be expected in the cladding over the fuel region; whereas, none would be expected in the plenum region. The formation of solid hydride, which has been attributed to the radiolytic decomposition of water by Markowitz (Reference 12), could have been limited by the formation of the thick oxide film along the internal clad surface (Figures 23, 26, and 30), by the intimate fuel/sheath contact (no gap for steam or hydrogen buildup), or by the size of the clad split which would have permitted a free passage of the hydrogen from within the rod. It was estimated metallographically that the hydrogen content was 400 to 500 ppm in the cladding at the plenum chamber; whereas, the rest of the rod exhibited an analyzed range of 209 to 239 ppm for the cladding in the fuel region. The concentration gradient was consistent with the thermal gradient in the cladding which was considerably higher over the fuel regions than over the plenum chamber. The higher hydrogen content in the cladding over the plenum chamber could have also been associated with the greater water volume and the thinner corrosion films.

C. Fuel Structure

The behavior of the ZrO_2-UO_2 fuel in rod BETT 79-64D was typical of ceramic material being irradiated in the molten state. The original porosity and geometry were completely altered (no annulus, no dishes, no pellet-to-pellet interfaces). The remainder of some central core and dishes both should have been found if melting had not occurred, since these means of incorporation of void volume had been found on other ceramic pelleted fuel rods which had been irradiated to higher burnups (References 6 and 17). In addition to the loss of the original pellet geometries, there was massive redistribution of fuel material, extensive fission product migration, and the formation of particles which were thought to have assisted in causing the waterlogging phenomenon (see Section VI.A).

After the initiation of melting during the first two cycles of operation and the formation of large pores surrounded by densified material, irradiation

of the fuel material near the outer pellet surfaces produced microstructures similar to those produced in other highly depleted ZrO_2-UO_2 fuel materials (Reference 1). Continued irradiation of the altered fuel material produced the small fission-gas pores found near the surface of the pellet. The possibility of melting significantly decreased after the first two cycles, because the heat flux was intentionally decreased and the size of the fuel/sheath gaps decreased. A combination of the high temperatures which caused the rapid oxidation of the clad by the steam environment, the volume expansion associated with the transformation of the ceramic material from the solid to the liquid state, and the redistribution of fuel material caused the effective sealing of the fuel/sheath gap. Thus, lower fuel temperatures would result during later stages of irradiation, since the size of the fuel/sheath gap and, hence, the thermal resistance were reduced.

Previous tests of intentionally defected samples containing ZrO_2-UO_2 materials have also indicated that this ceramic material has a high corrosion resistance under irradiation (Reference 1). This was also true for rod BETT 79-64D, although it was exposed to considerably higher temperatures and thermal gradients than those experienced by the reference materials. It is quite possible, however, that the extent of corrosion attack may have been limited because the defect hole was not located directly over a pellet or because the hole was periodically plugged by the fragmented fuel material.

VII. CONCLUSIONS

1. The element failure was caused by the formation of a longitudinal rupture in the tubing wall in the region of the plenum chamber. It is postulated that the rupture resulted from excessive plastic strain in the cladding because of successive waterlogging type internal pressurizations of the fuel element.
2. Post-irradiation metallographic structures of the fuel exhibited the occurrence of multiple melting zones. The presence of these zones was analytically confirmed by FIGRO computer program calculations which indicated fuel melting conditions.
3. Post-irradiation metallographic structures of the fuel indicated there was very little fuel lost through corrosion mechanisms.
4. Excessive hydrogen pickup or the presence of solid hydride was not observed in the Zircaloy-4 clad.
5. Fully annealed Zircaloy-4 tubing material can undergo severe deformations (circumferential strains in excess of 8.5 percent) at high fast neutron flux dosages without rupturing.

6. Annular ceramic-pelleted fuel rods can undergo significant amounts of fuel redistribution if the material near the central hole becomes fragmented (cracked) and falls into the central core. The ceramic material can also become redistributed if the fuel becomes molten and plastically flows into a central core which was fabricated or which results from melting.
7. The corrosion resistance of ZrO_2 + 29.6 w/o UO_2 fuel material irradiated at very high temperatures is very satisfactory.

ACKNOWLEDGMENTS

The authors acknowledge the efforts and interest of the many people whose contributions made this report possible. Those principally responsible for various phases of the program include R. W. Reidl, C. R. Woods, D. J. Clark, D. C. Corrigan, E. G. Stevens, J. D. Eichenberg, T. R. Padden, and C. P. Gamber. Valuable comments and assistance were received from B. F. Rubin, and R. C. Daniel who was of great assistance in interpreting the metallographic results.

REFERENCES

1. B. F. Rubin, R. M. Berman, and M. L. Bleiberg, "The Irradiation Behavior of ZrO_2-UO_2 Fuels," WAPD-264, October 1962.
2. J. D. Eichenberg, F. J. Lennon, and K. L. Rupp, "Remotely Operable High-Precision Dimensioning Equipment" in "Proceedings of the Twelfth Conference on Remote Systems Technology, Held in Conjunction with American Nuclear Society Winter Meeting, San Francisco, November 30 - December 3, 1964," pp 207-215, American Nuclear Society, Inc., Hinsdale, Illinois, 1964.
3. I. Goldberg, L. L. Lynn, and C. D. Sphar, "FIGRO: FORTRAN-IV Digital Computer Program for the Analysis of Fuel Swelling and Calculation of Temperature in Bulk-Oxide Cylindrical Fuel Elements," WAPD-TM-618, December 1966.
4. W. A. Carbiener, "Nondestructive Examination of Radioactive Material Using Neutron Radiography," Nucl. Appl. 2, 468-470 (1966).
5. B. V. Rubin, "Examination of a Failed Rod Operating with Molten UO_2-ZrO_2-CaO Fuel," WAPD-TM-593, December 1966.
6. B. Rubin, R. C. Daniel, L. Lynam, J. E. McCauley, and H. B. Meieran, "Irradiation Performance Capabilities of Oxide Fuel Rods: X-1-u Test of Two 100-Inch Long Highly Rated Annular ZrO_2-UO_2 Fuel Rods," WAPD-TM-574, September 1966.

7. C. R. Woods, Ed., "Properties of Zircaloy-4 Tubing," WAPD-TM-585, December 1966.

8. H. B. Meieran, "History of the NRX Reactor X-1-q and X-3-n Tests and the Nondestructive Post-Irradiation Examination of Their Plate-Type Ceramic Fuel Elements," WAPD-TM-455, March 1966.

9. B. Lustman, "Irradiation Effects in Uranium Dioxide" in "Uranium Dioxide: Properties and Nuclear Applications," J. Belle, Ed., pp 431-666, U. S. Government Printing Office, Washington 25, D.C., 1961.

10. J. D. Eichenberg, P. W. Frank, T. J. Kisiel, B. Lustman, and K. H. Vogel, "Effects of Irradiation on Bulk UO_2," WAPD-183, October 1957.

11. F. T. Dunckhorst, L. L. Lynn, W. A. Coffman, and J. E. Meyer, "GLUB-1 - A FORTRAN-IV Digital Computer Program for Waterlogged Fuel Element Analysis," WAPD-TM-569, November 1966.

12. J. M. Markowitz, "Internal Zirconium Hydride Formation in Zircaloy Fuel Element Cladding under Irradiation," WAPD-TM-351, May 1963.

13. J. Belle, R. M. Berman, W. F. Bourgeois, I. Cohen, and R. C. Daniel, "Thermal Conductivity of Bulk Oxide Fuels," WAPD-TM-586 (Rev.), April 1967.

14. A. M. Ross and R. L. Stoute, "Heat Transfer Coefficient between UO_2 and Zircaloy-2," AECL-1552 (CRFD-1075), June 1962.

15. J. A. L. Robertson, "$\int k d\theta$ in Fuel Irradiations," AECL-807 (CRFD-835), April 1959.

16. H. B. Meieran and J. T. Engel, "Irradiation Performance of Zircaloy-4 Sheathed, 97% Theoretical Density UO_2 Fuel Rods Irradiated at Low Thermal Ratings (LSBR/LWBR Development Program)," WAPD-TM-631, July 1968.

17. R. M. Berman, H. B. Meieran, and P. W. Patterson, "Irradiation Behavior of Zircaloy-Clad Fuel Rods Containing Dished-End UO_2 Pellets (LWB-LSBR Development Program)," WAPD-TM-629, July 1967.

18. R. M. Berman, "Homogenization of Two Phase Mixtures of ZrO_2-UO_2 by Irradiation," J. Nucl. Materials, 17, 313-323 (1965).

19. J. B. Newman, "Elastic Analysis of Thermal Gradient Bowing in Rod Type Elements Subjected to Axial Thrust (LWBR/LSBR Development Program)," WAPD-TM-726, January 1968.

TABLE 1. THERMAL-NUCLEAR HISTORY FOR ROD BETT 79-64D

ETR Cycle	Date(2) From-To	Test	Shroud v/o Hf	Exposure Time, EFPD	Heat Flux (Btu/hr-ft^2 x 10^{-6})(1)		Accumulative Burnup (f/cc x 10^{-20})(1)		Accumulative Fast Flux (>1 Mev), nvt x 10^{20}
					Maximum	Average	Maximum	Average	
64	6-10 to 6-22-64*	L-12-14	40	10.7	1.590	1.243	1.35	1.04	1.66
65A	7-19 to 7-23-64	L-12-19	100	15.0	1.747	1.372	1.94	1.51	2.39
65D	7-30 to 8-16-64	L-12-21	100	23.5	1.080	0.857	2.66	2.07	3.78
66	8-27 to 9-27-64	L-12-21	100	49.3	1.091	0.873	4.86	3.81	8.02
67	10-9 to 11-15-64*	L-12-21	100	78.8	1.052	0.850	7.26	5.73	13.10
68A, B	12-1 to 12-14-64*	L-12-21	100	88.5	0.942	0.773	7.96	6.30	14.80
69	1-24 to 2-14-65	L-12-22	100	107.2	0.954	0.791	9.34	7.43	18.00
70A	3-1 to 3-8-65*†	L-12-22	100	112.4	0.887	0.742	9.69	7.72	18.76
75A	9-26 to 10-9-65‡	L-12-27	100	121.2	0.709	0.587	10.16	8.10	20.06

(1) Based on loop calorimetric data
(2) * - Interim examination conducted at ECF at the end of this cycle
† - Post-shutdown examination conducted at Bettis Laboratory at the end of this cycle
‡ - Post-failure examination conducted at Bettis Laboratory

TABLE 2. NOMINAL L-12 LOOP DESIGN OPERATING AND CHEMISTRY CONDITIONS[1]

A. Operating Conditions	
1. Reactor power level	175 MW
2. Test section flow rate	48 gpm @ 445 F (19.7 ft/sec)
3. Loop pressure	2000 psig
4. Loop inlet temperature at test assembly	445 F
5. Predicted loop outlet temperature	494 F
6. Predicted assembly ΔT	49 F
7. Predicted heat output	1,014,000 Btu/hr, 297 kw
B. Chemistry Conditions	
1. Hydrogen	30 cc/Kg (15 - 60 cc/kg range)
2. Oxygen	0.05 ppm (max)
3. pH	9.8 - 10.2 NH_4OH
4. Conductivity	Consistent with pH (19 to 48 micro-mhos/cm)
5. Change IX resin	As required by decontamination factor or maintenance of pH level
6. Crud concentration	3 ppm (max.)
7. Makeup Water	
a) Purification Resins	Mixed bed (H - OH form)
b) pH	Deoxygenating (Sulfite) 6.0 to 8.0
c) Oxygen concentration	0.05 ppm (max)
d) Conductivity	2.5 micro-mhos/cm (max)
e) Chloride (by chemical analysis)	0.1 ppm chloride max
f) Particulate matter	None visible

(1) These conditions were for the L-12-21 test irradiated during ETR cycle 67. Design parameters varied during various test phases and ETR cycles as dictated by required conditions.

TABLE 3. BULK WATER AND AVERAGE CLAD SURFACE TEMPERATURE FOR ROD BETT 79-64D

ETR Cycle	Local Bulk Water Temperature, F	Average Clad Surface Temperature, F	Film Coefficient (Btu/Hr-Ft^2 - F)	Loop Inlet Water Temperature, F
64	336	478	8740	325
65A	384	535	9040	371
65D	448	544	9010	439
66	448	545	9010	439
67	454	549	9000	445
68A, B	451	537	9000	442
69	525	617	8590	515
70A	518	608	8260	510
75A	516	589	8060	510

TABLE 4. RADIOCHEMICAL BURNUP VALUES FROM ROD BETT SPECIMEN 79-64D

Sample Ident. No.(1)	Weight Ratio Pu^{239}: U^{238}	Atom Percent Estimated U^{238} Depletion	Atom Percent Corrected U^{235} Depletion	Atom Percent Corrected U^{235} Fission	Burnup Analysis f/cc x 10^{-20} compartment
B-6	0.033	4.1	16.8	13.2	4.26
B-13	--	4.5	18.6	14.3	4.62
B-24	--	5.2	21.1	16.9	5.46
B-32	0.041	5.5	22.1	17.9	5.68
B-37	--	5.9	24.2	19.4	6.27

(1) Number indicates pellet identity in the fuel stack at is elevation prior to irradiation.

TABLE 5. OXIDE FILM THICKNESS

Sample	(1) HL No.	Distance from Fuel Bottom (inches)	Oxide Film Thickness, Microns		Remarks
			Clad ID Surface	Clad OD Surface	
TE-L	3394	9	6-10	4 (to 6 near fuel)	External film uniform. Internal film jagged.
TE-T	3390	8 3/4	14 (@ peaks)	6 at fracture	External film spotty.
D-L	3389	8	10 to 14	1	Internal oxide jagged from bulge on. Range 0 to 10 microns.
P19-T	3393	3 7/8	10	4	
P4-5T	3392	3/4	10	4	
P1-3L	3391	0	4-12 10 to 20 @ Red Bottom	0 to 3	

(1) Hot Laboratory Sample Number

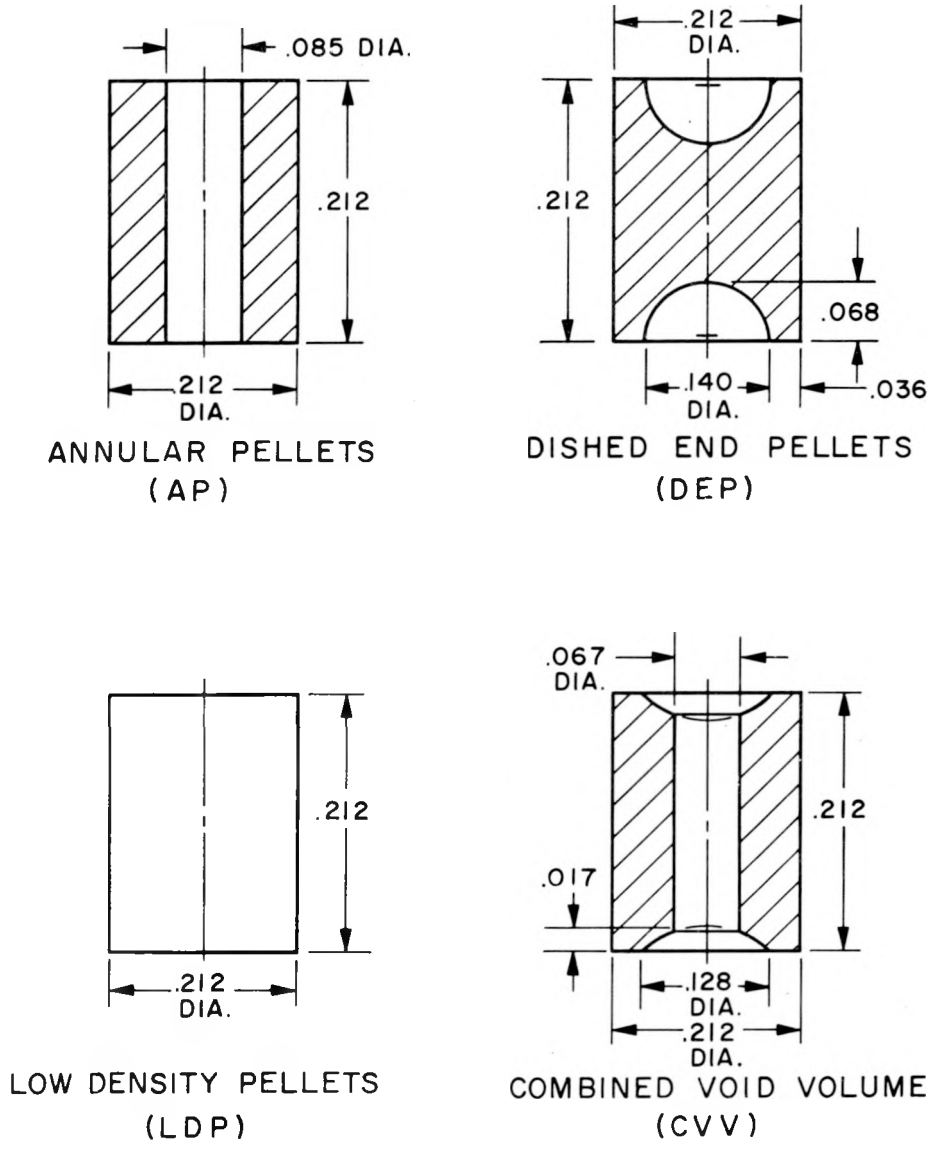

Figure 1. Configurations and Nominal Dimensions of Pellets Used in L-12 Test Rods

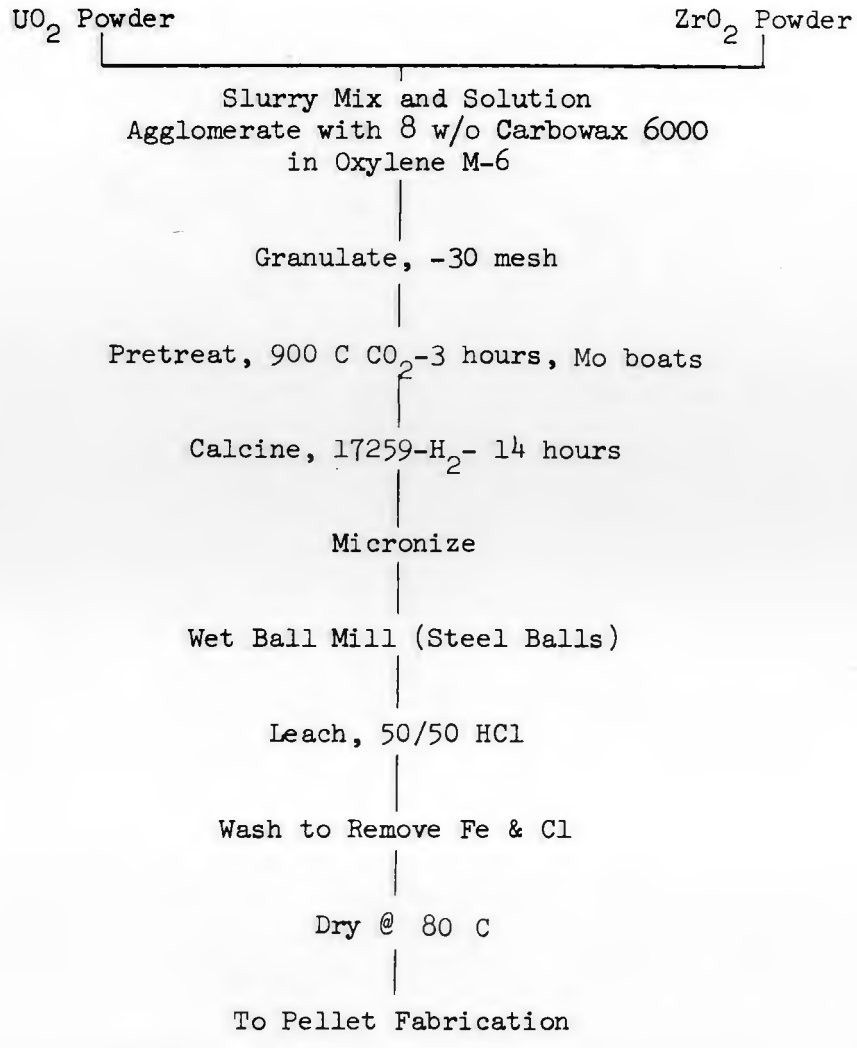

Figure 2. Bettis Laboratory Fuel Powder Preparation Flow Sheet

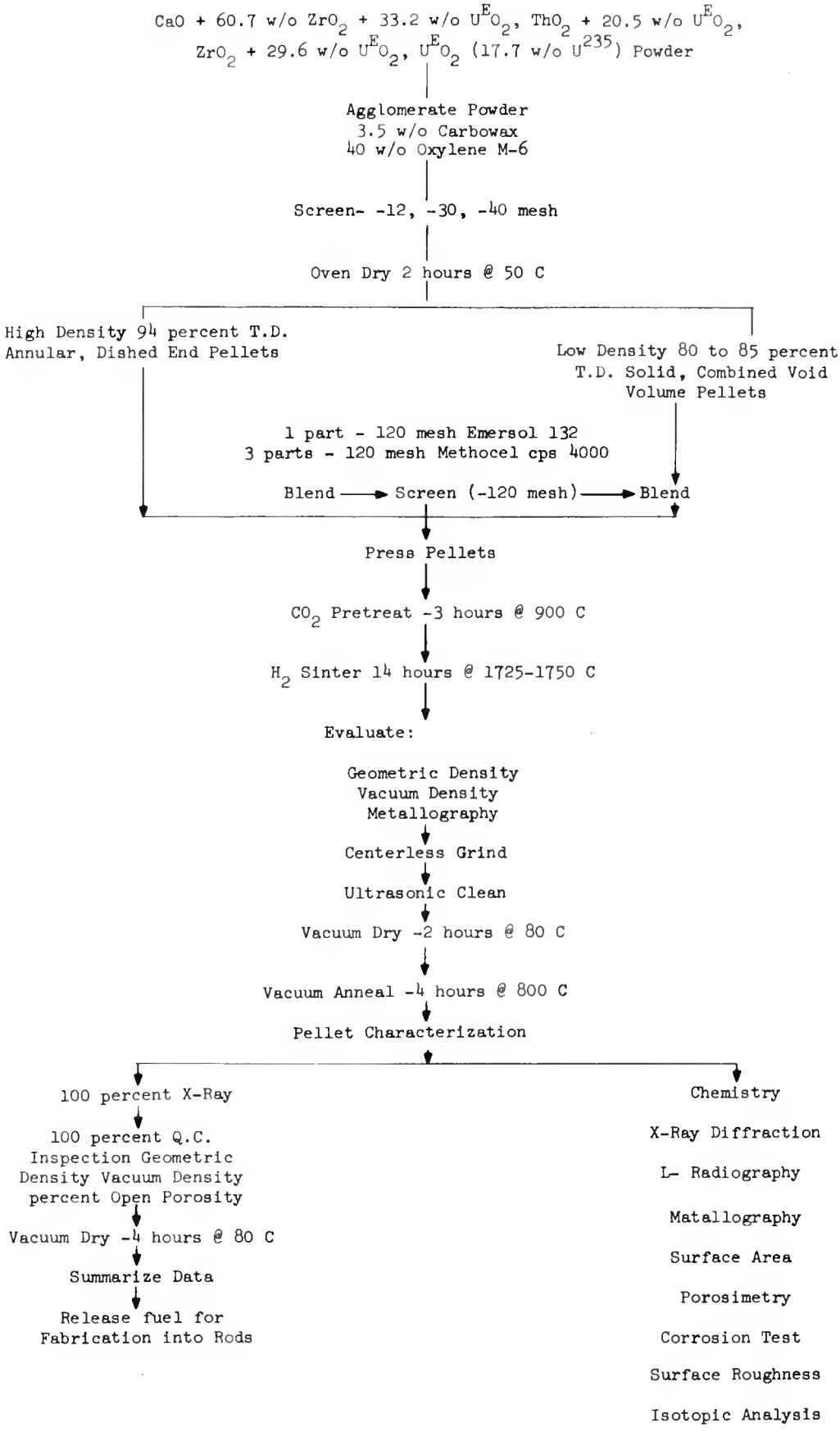

Figure 3. Bettis Laboratory Fuel Pellet Fabrication Flow Sheet

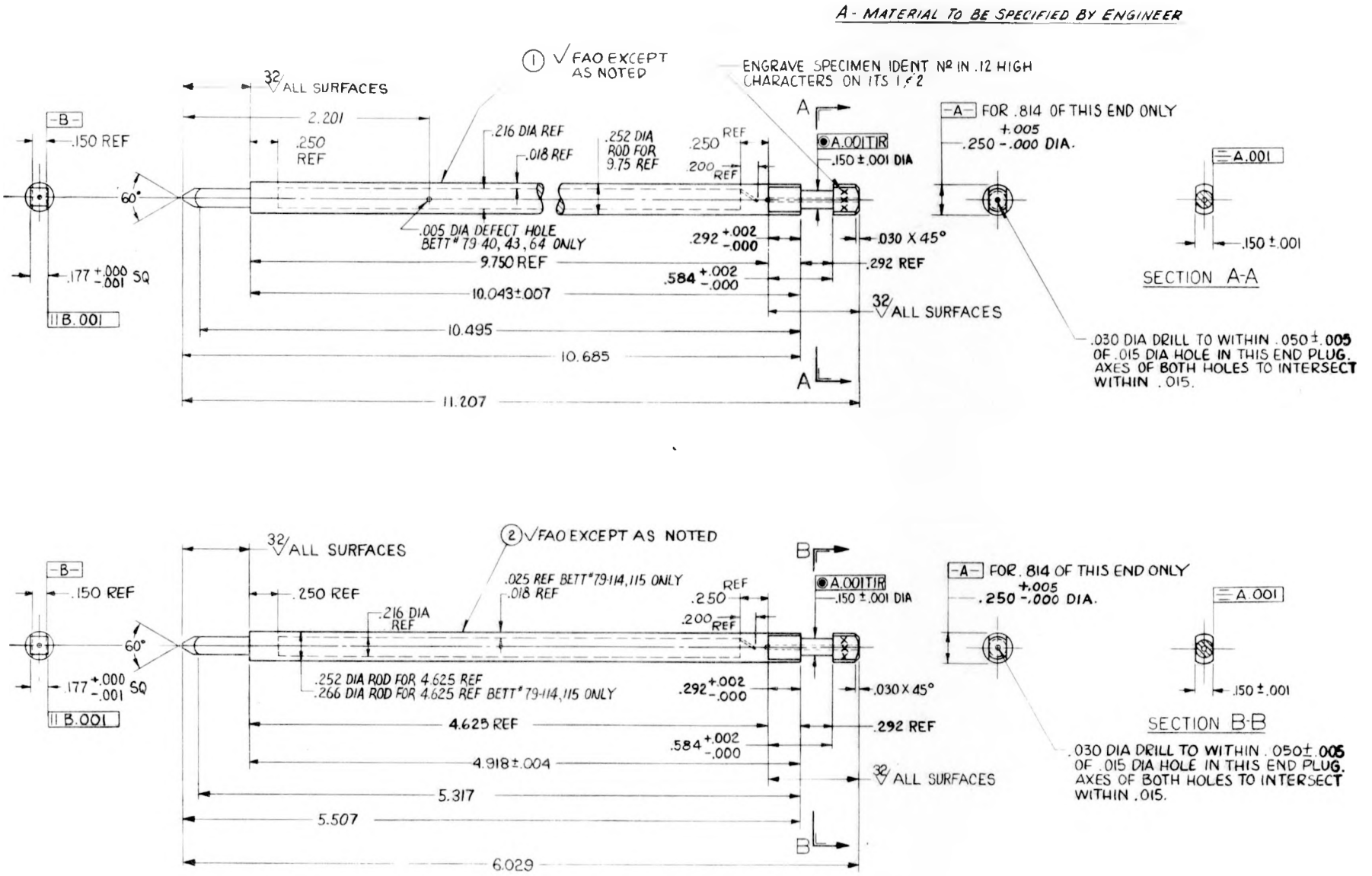

Figure 4. Drawing of Fuel Rod BETT 79-64D

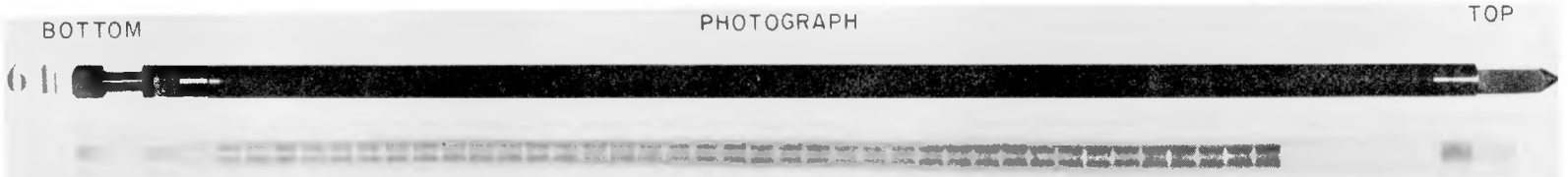

ZIRCALOY-4 SHEATH MATERIAL:		
AVERAGE O.D., IN. (CMS)	0.2528	(0.6421)
AVERAGE WALL THK., IN. (CMS)	0.0178	(0.0452)
AVERAGE I.D., IN. (CMS)	0.2173	(0.5519)
TYPE:	ANNEALED	
AVERAGE FUEL/SHEATH DIAMETRAL CLEARANCE, IN. (CMS)	0.0049	(0.0124)
ZrO_2 - 29.6 w/o U^EO_2 PELLET:		
w/o U^{235} IN U^T	93.09	
TYPE PELLET	COMBINED VOID VOLUME	
NO. OF PELLETS PER ROD	38	
DENSITY, % T.D‡-IN FUEL (VACUUM)	92.0	
-IN FUEL STACK (GEOMETRIC)*	78.0	
DIAMETER: AVERAGE O.D., IN. (CMS)	0.2124	(0.5395)
AVERAGE I.D., IN. (CMS)	0.0631	(0.1603)
DISH: AVERAGE DEPTH, IN. (CMS)	0.0166	(0.0422)
AVERAGE DIAMETER, IN. (CMS)	0.1360	(0.3454)
AVERAGE SHOULDER, IN. (CMS)	0.0362	(0.0919)
POROSITY IN FUEL: % OPEN	5.2	
% CLOSED	2.8	
% VOID VOLUME★ OPEN POROSITY	4.5	
CLOSED POROSITY	2.4	
DISH AND ANNULUS	13.2	
TOTAL	20.1	

FUEL STACK HEIGHT, IN. (CMS)	8.052	(20.452)
Gm U^{235}/INCH	0.786	
U^{235} ATOMS/CM^3 X 10^{-20}:		
FUEL MATERIAL	38.3	
FUEL STACK	32.3	
TOTAL AXIAL PLENUM CHAMBER:		
LENGTH, IN. (CMS)	1.189	(3.020)
% OF FUEL STACK HEIGHT	14.75	
% OF INTERNAL COMPARTMENT LENGTH	12.88	

‡ THEORETICAL DENSITY OF ZrO_2 - 29.6 w/o U^EO_2 = 7.00 GM/CM^3

* GEOMETRIC DENSITY = $\frac{\text{WT. OF FUEL STACK}}{\pi/4 \times \text{LENGTH OF FUEL STACK} \times (\text{AVG. PELLET OUTSIDE DIAM.})^2}$

★ CORRECTED FOR VOLUME OF FUEL MATERIAL AND EXCLUDES VOID IN FUEL/SHEATH GAP

Figure 5. Description, Photograph, Radiograph, and Summary of As-Built Characteristics for Rod BETT 79-64D

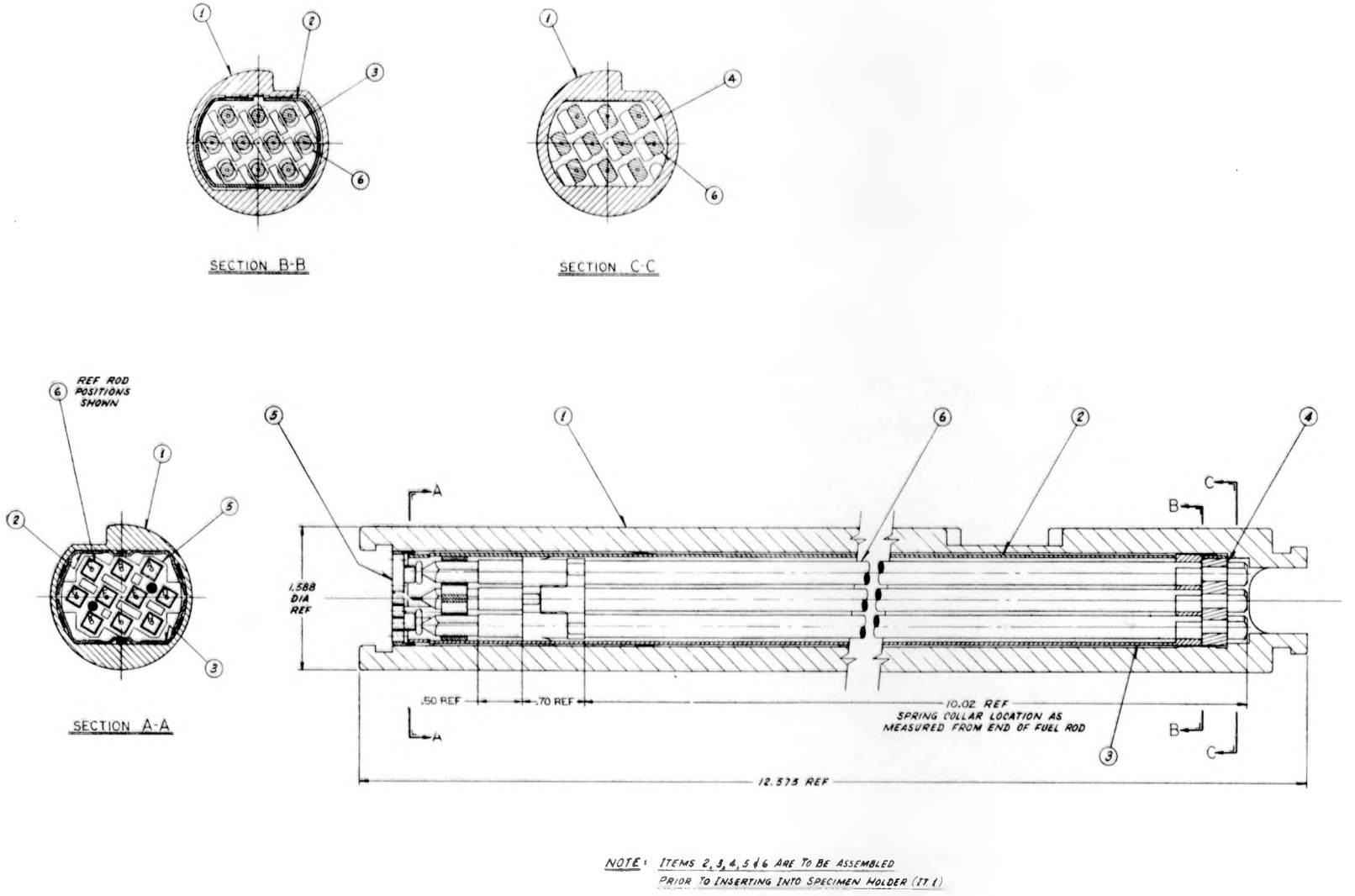

Figure 6. Configuration of L-12 Test Holder 1 Rod Holder Assembly

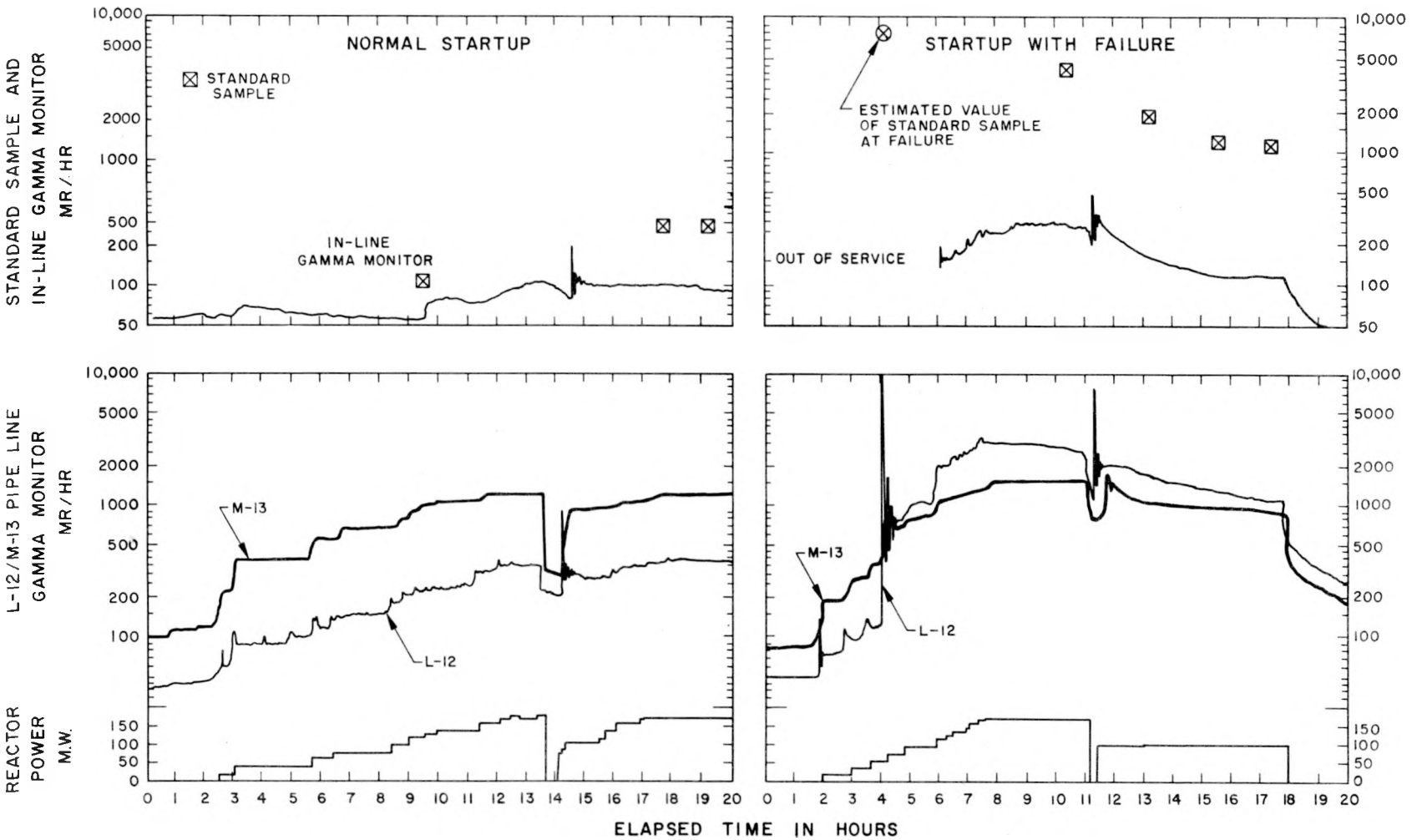

Figure 7. Comparison between Normal Startup and Startup with a Failure on L-12/M-13

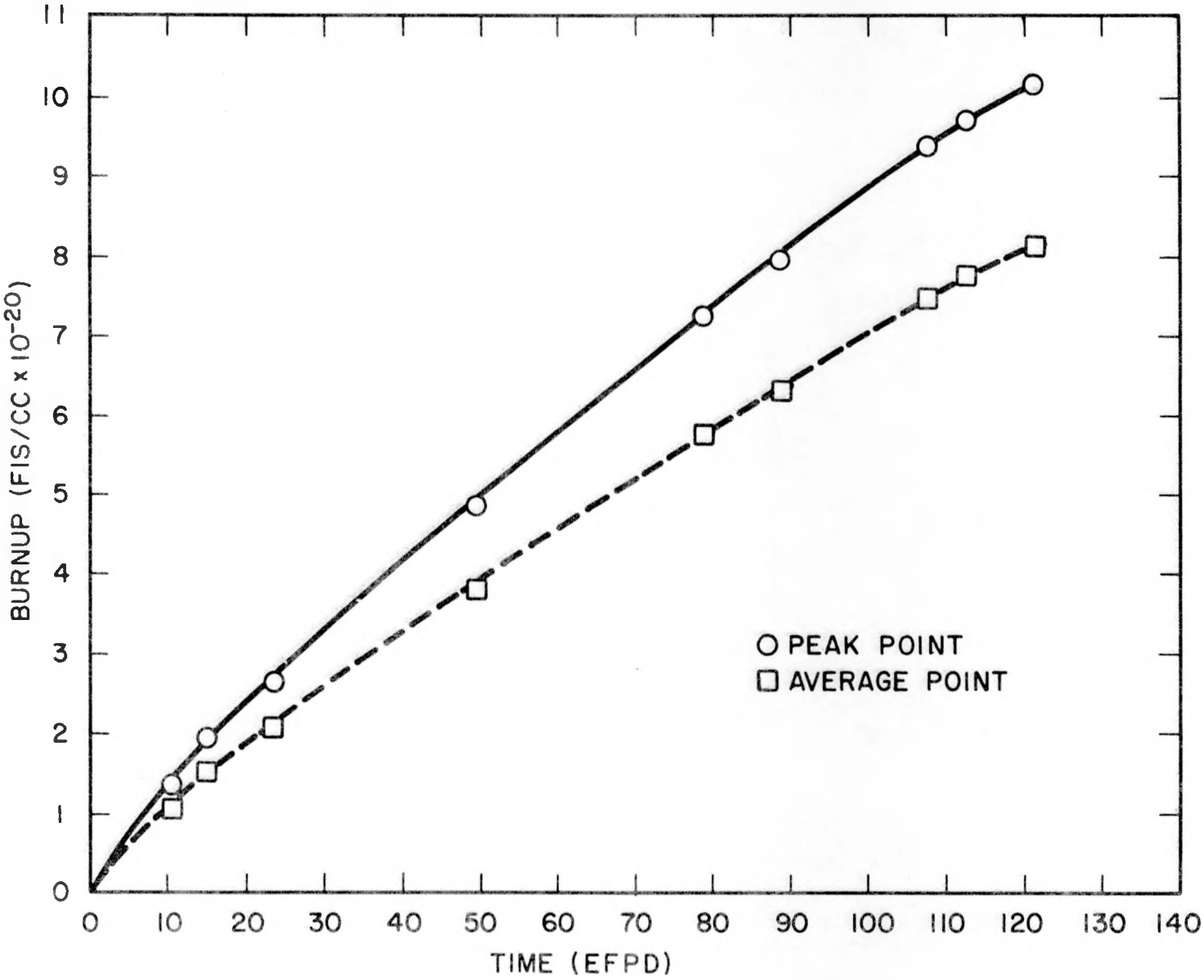

Figure 8. Burnup for Failed Rod BETT 79-64D

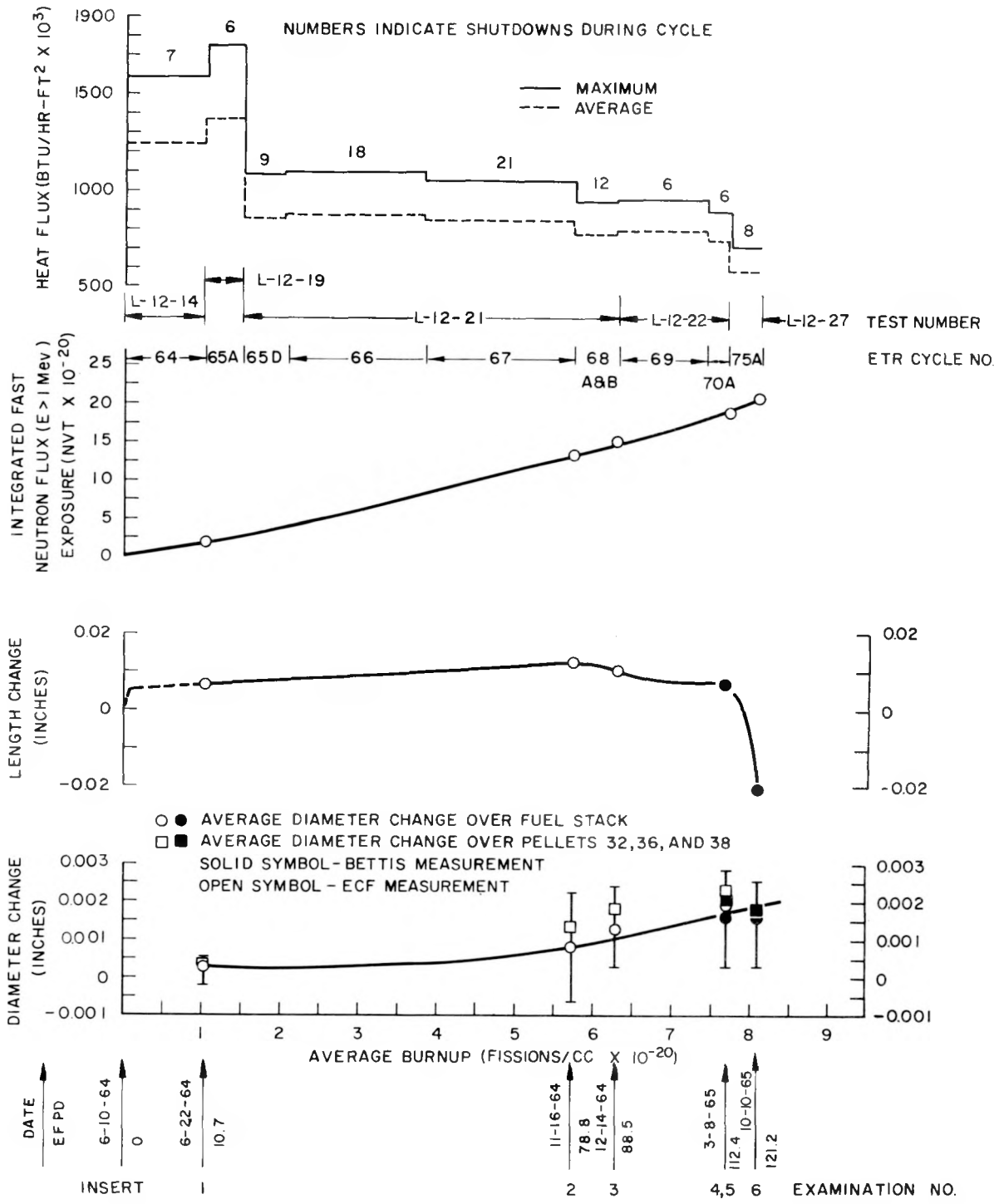

Figure 9. Operating History and External Dimensional Changes as a Function of Burnup for Rod BETT 79-64D

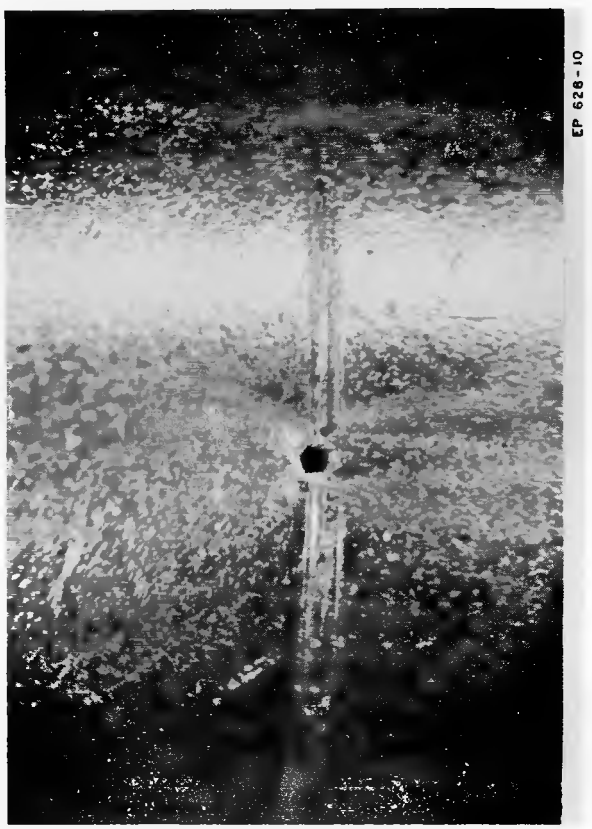

Figure 10. Defect Hole on Rod BETT 79-64D Taken during its Third Interim Examination on December 14, 1964. X18

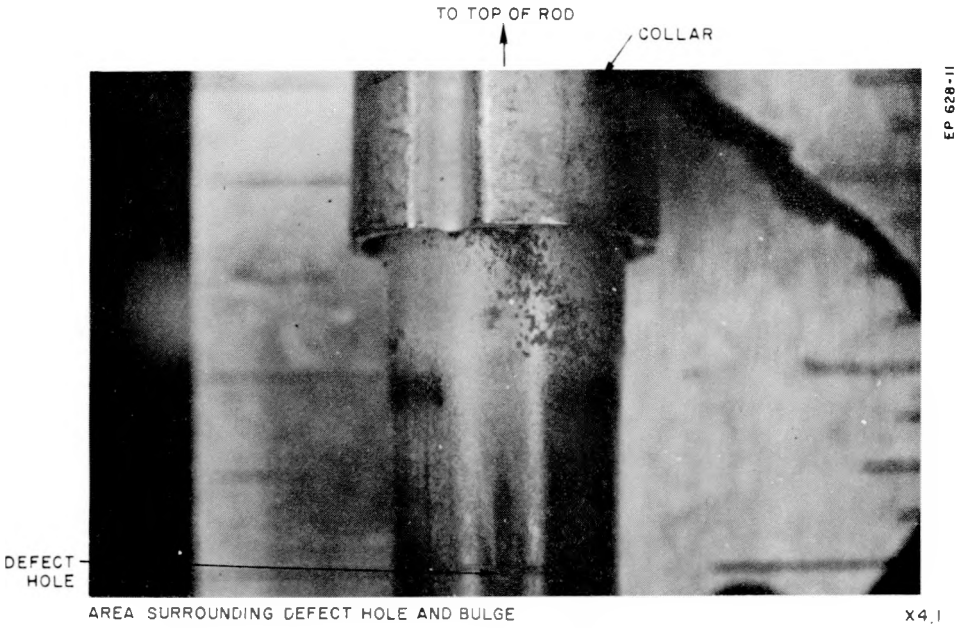

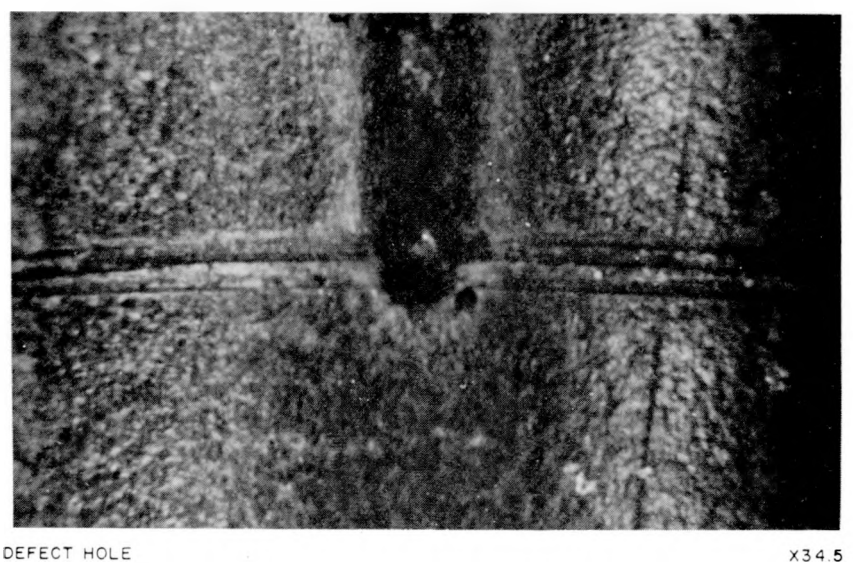

Figure 11. Photographs of Rod BETT 79-64D Taken during its Fourth Interim Examination, March 8, 1965

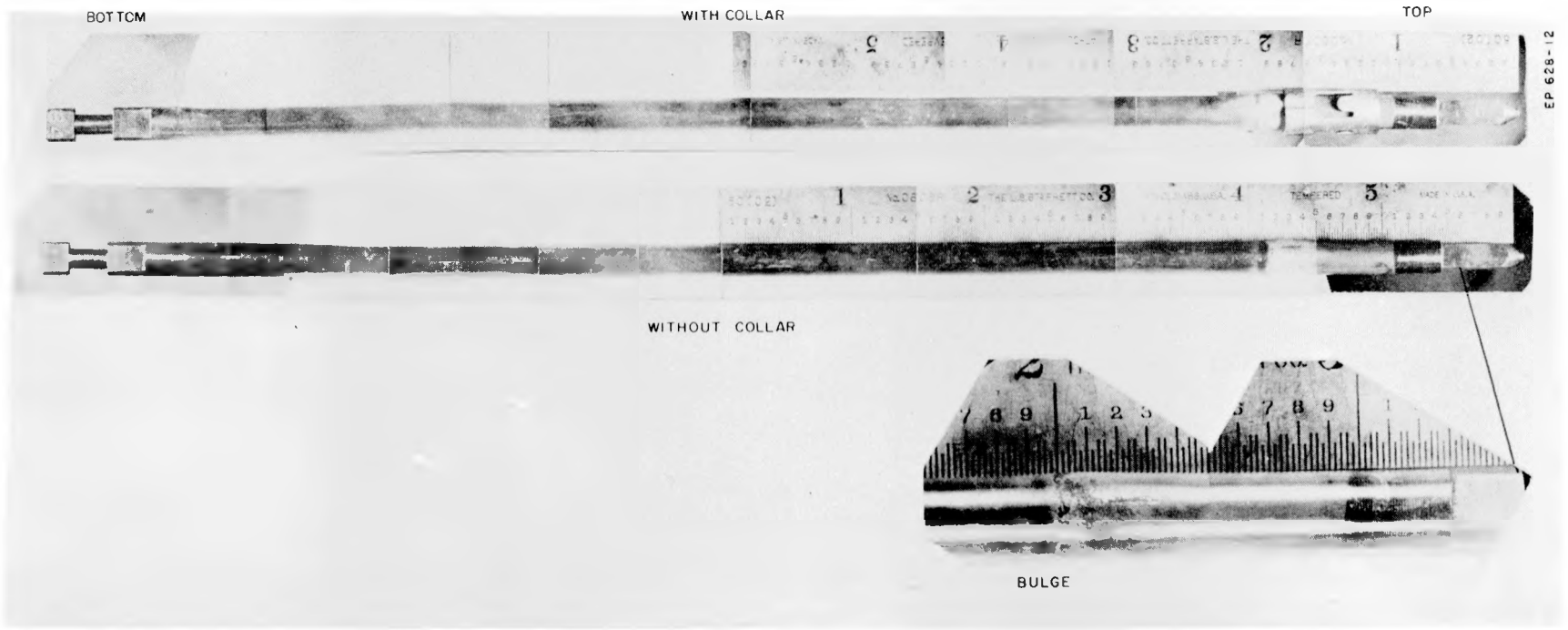

Figure 12. Photographs of Rod BETT 79-64D Taken at Bettis Laboratory Showing Bulge

EP 629-13

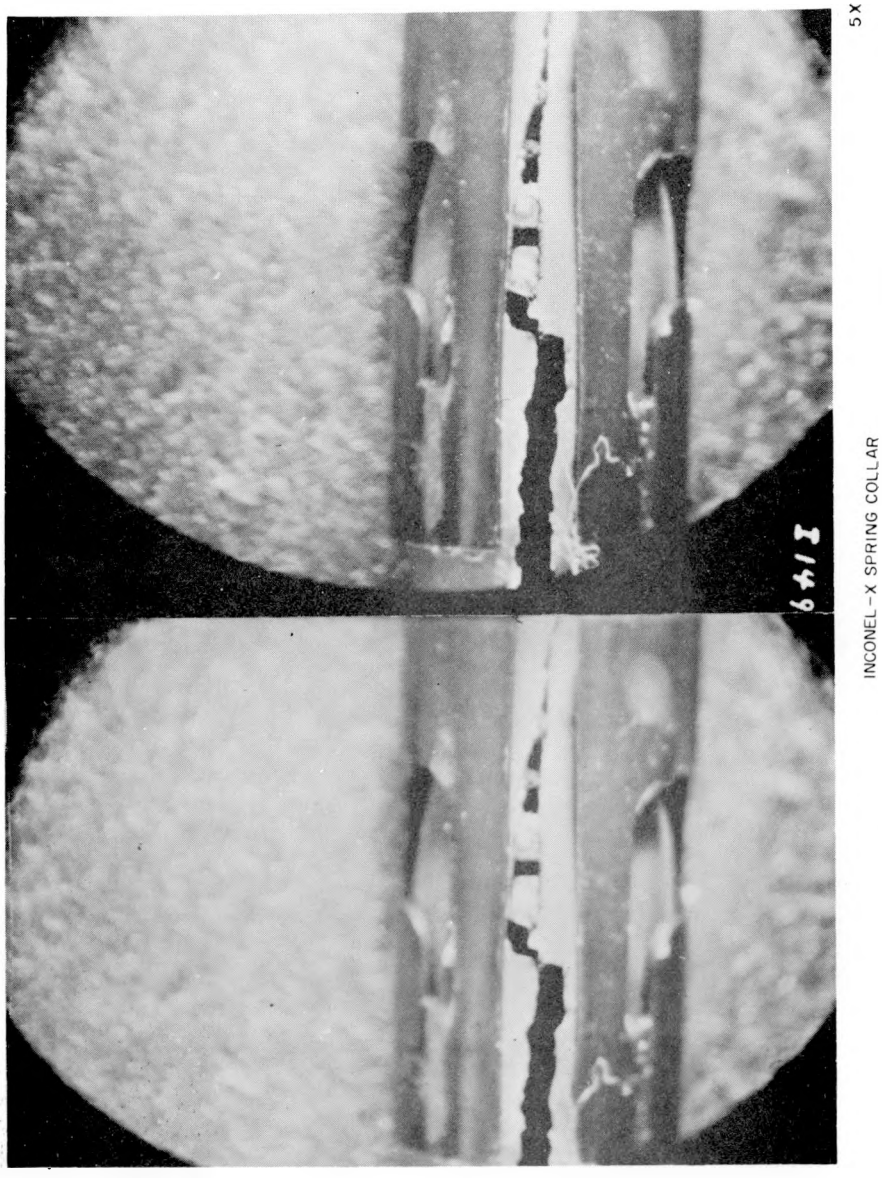

Figure 13. Clad Rupture in Rod BETT 79-64D Taken at ECF. Note Fuel Particles in Crack

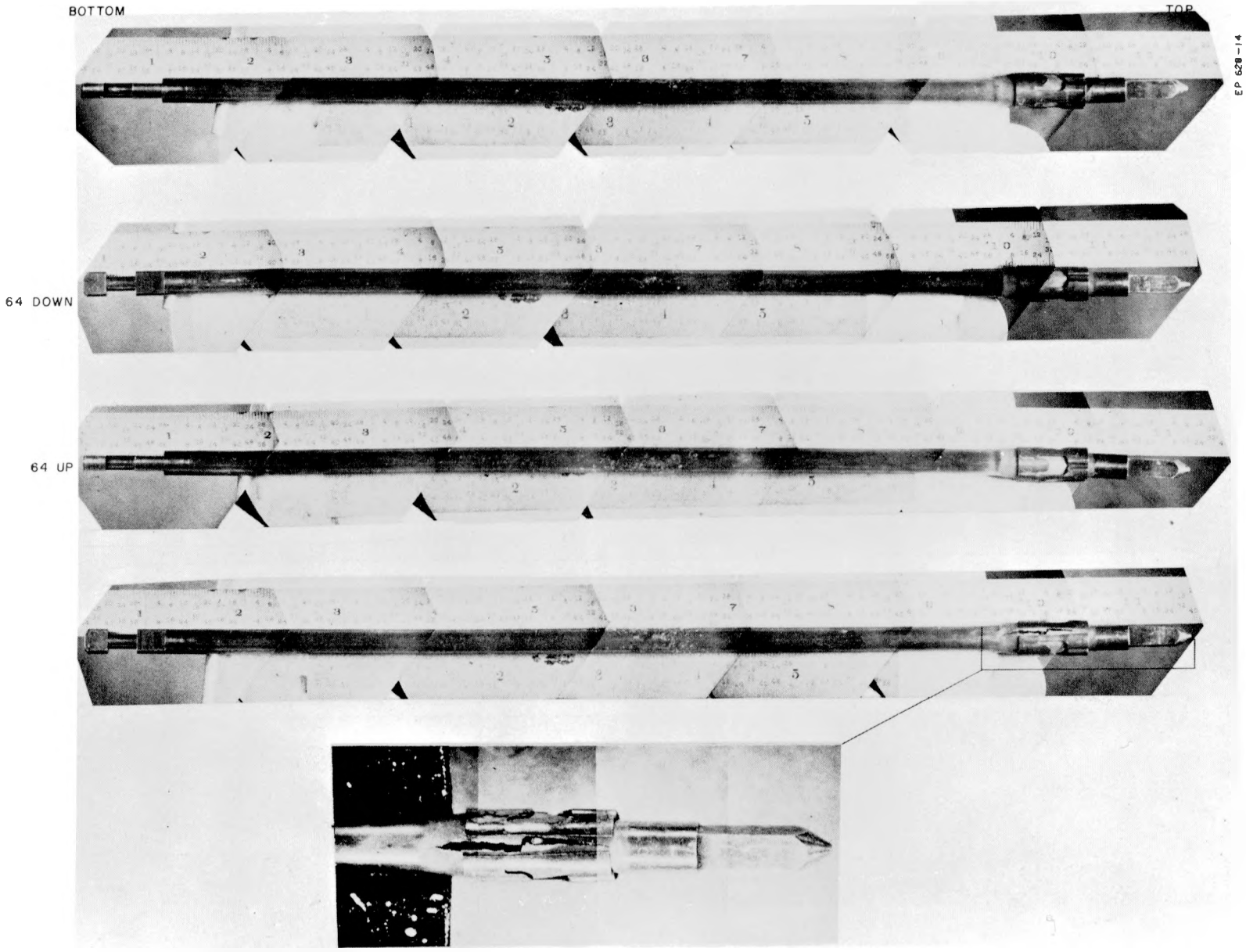

Figure 14. Photographs of Rod BETT 79-64D Taken at Bettis Laboratory After the Cladding had Ruptured

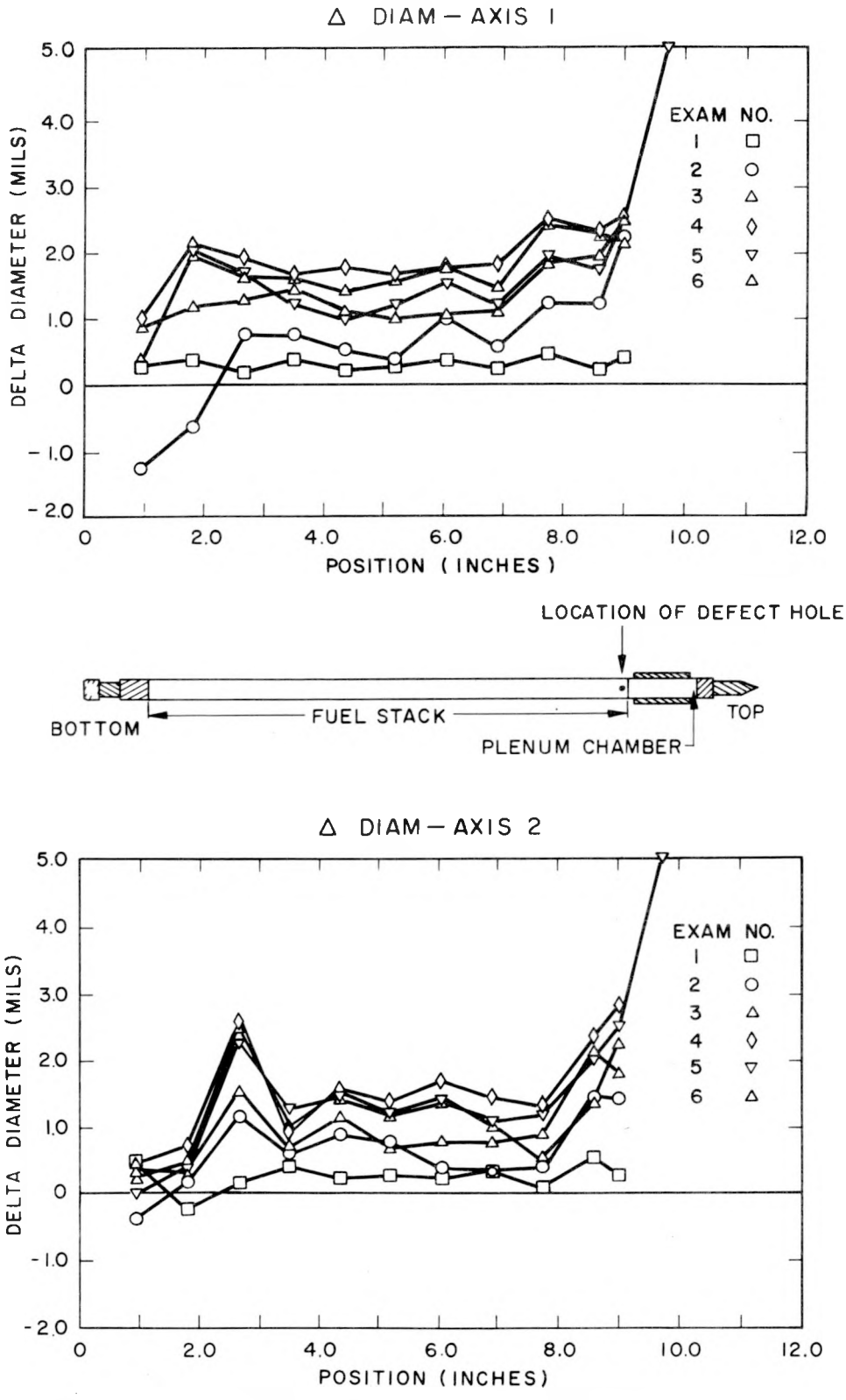

Figure 15. Diameter Changes for Rod BETT 79-64D

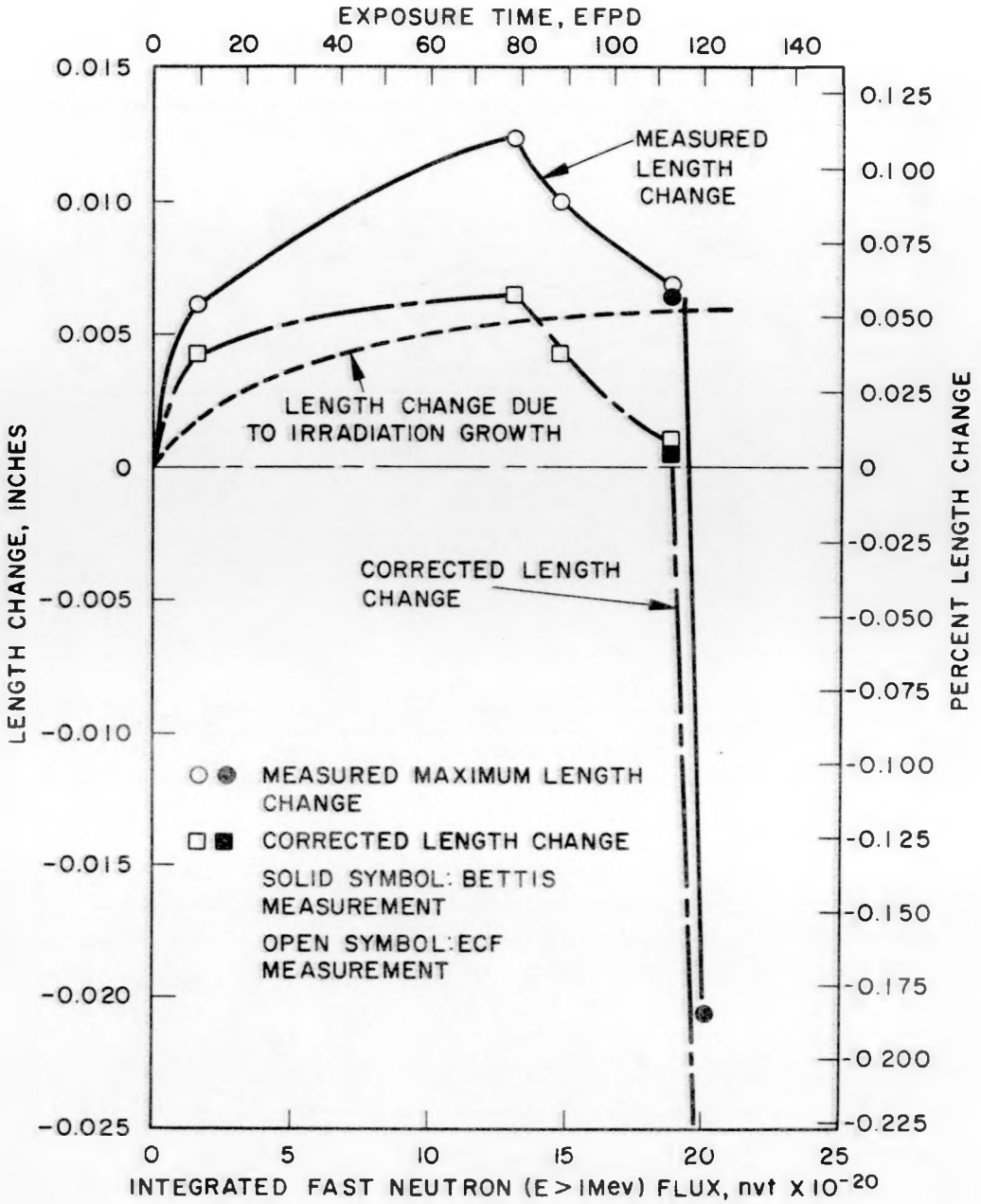

Figure 16. Length Change for Rod BETT 79-64D as a Function of Integrated Fast Neutron Flux Dose and Exposure Time

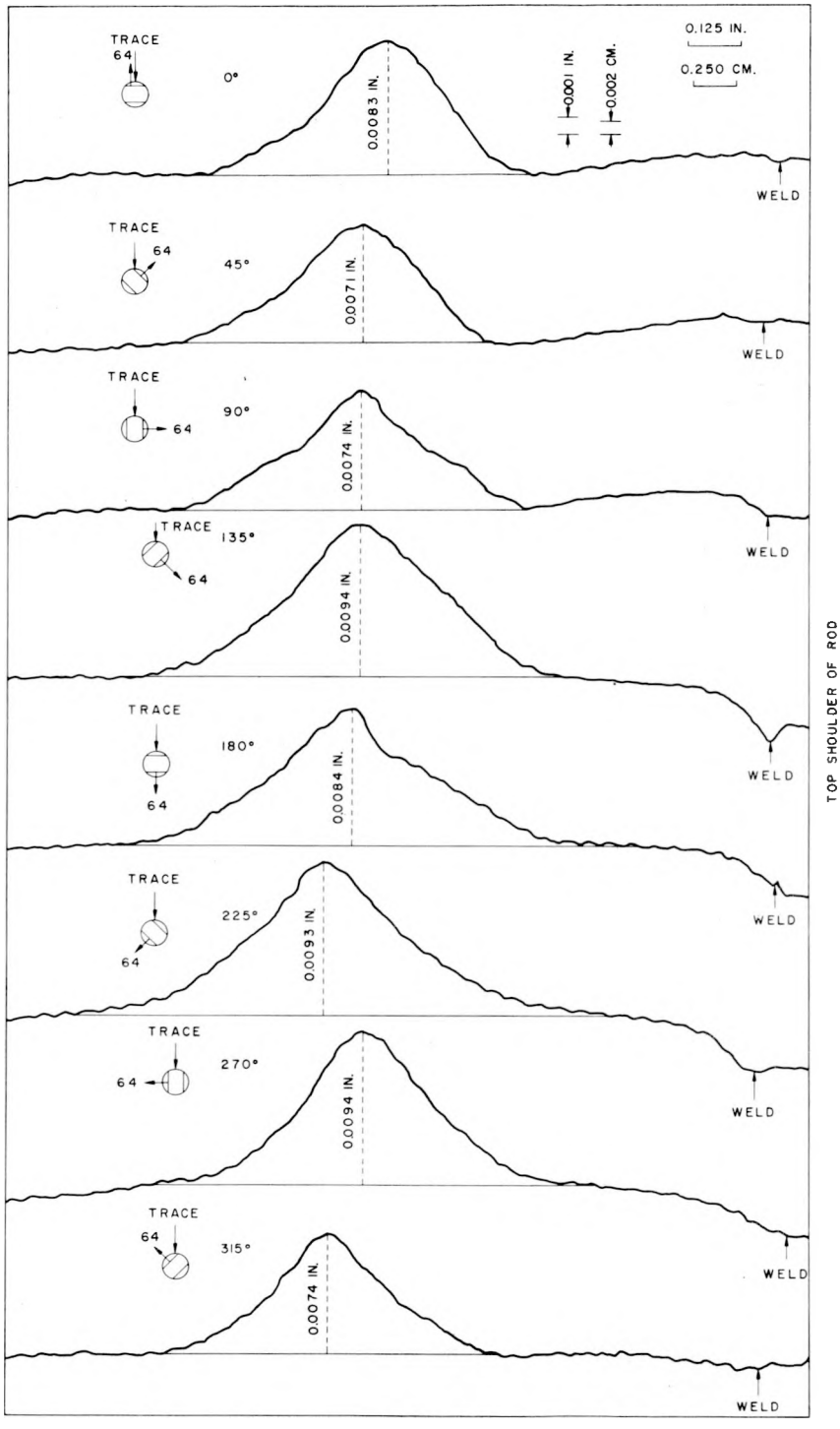

Figure 17. Profile Trace of Bulge on Rod BETT 79-64D Taken Prior to Time of Reinsertion and Ultimate Failure

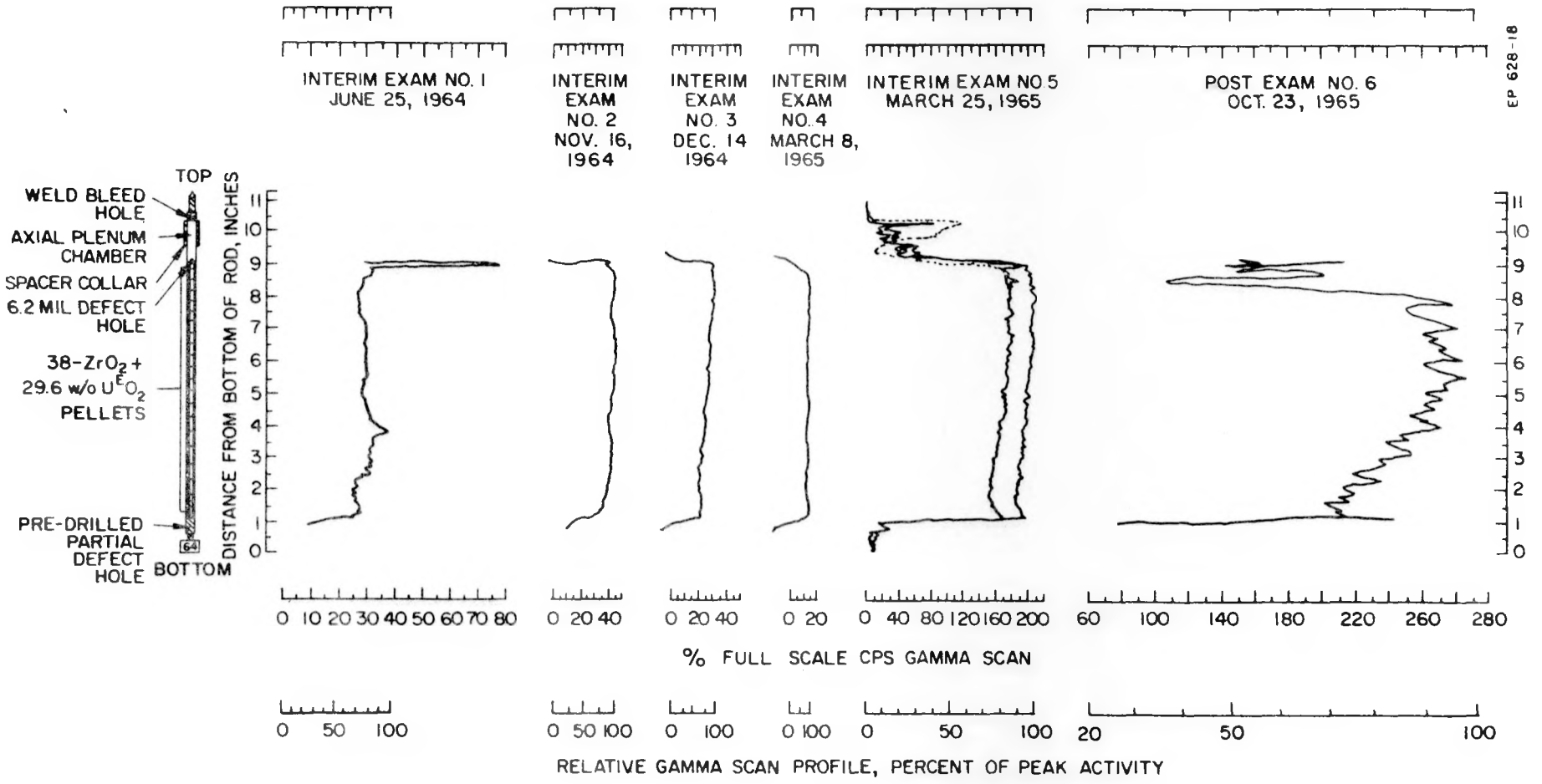

Figure 18. Interim Examination Gamma Scans for Rod BETT 79-64D

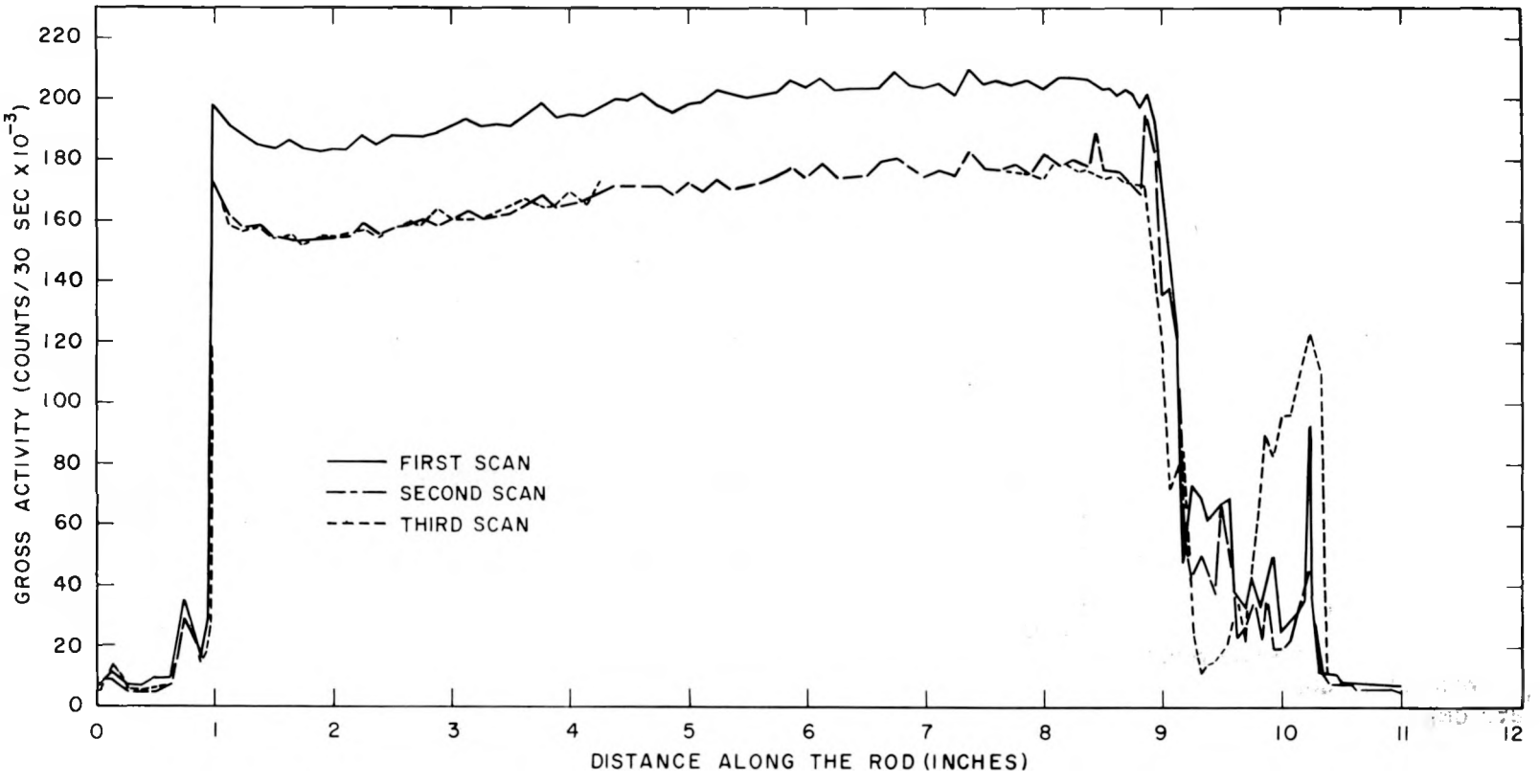

Figure 19. Three Scans Taken during Examination of March 30, 1965 Showing the Movement of Loose Fuel in the Plenum Chamber

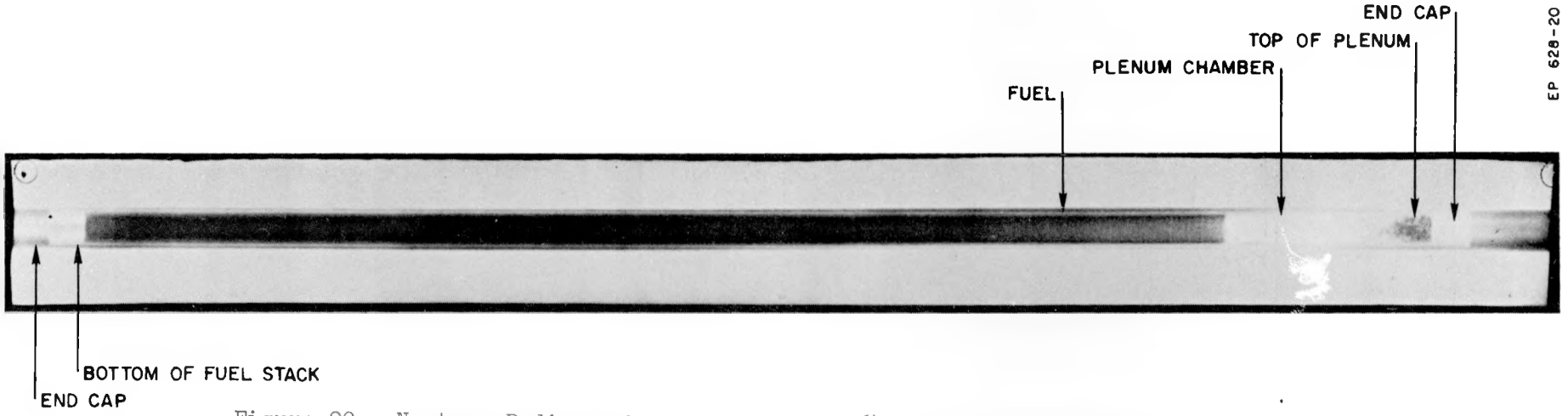

Figure 20. Neutron Radiograph of Rod BETT 79-64D before Reinsertion into L-12 Loop, September 13, 1965. Internal "Compartment" Length is 9.25 inches (from End Cap to End Cap)

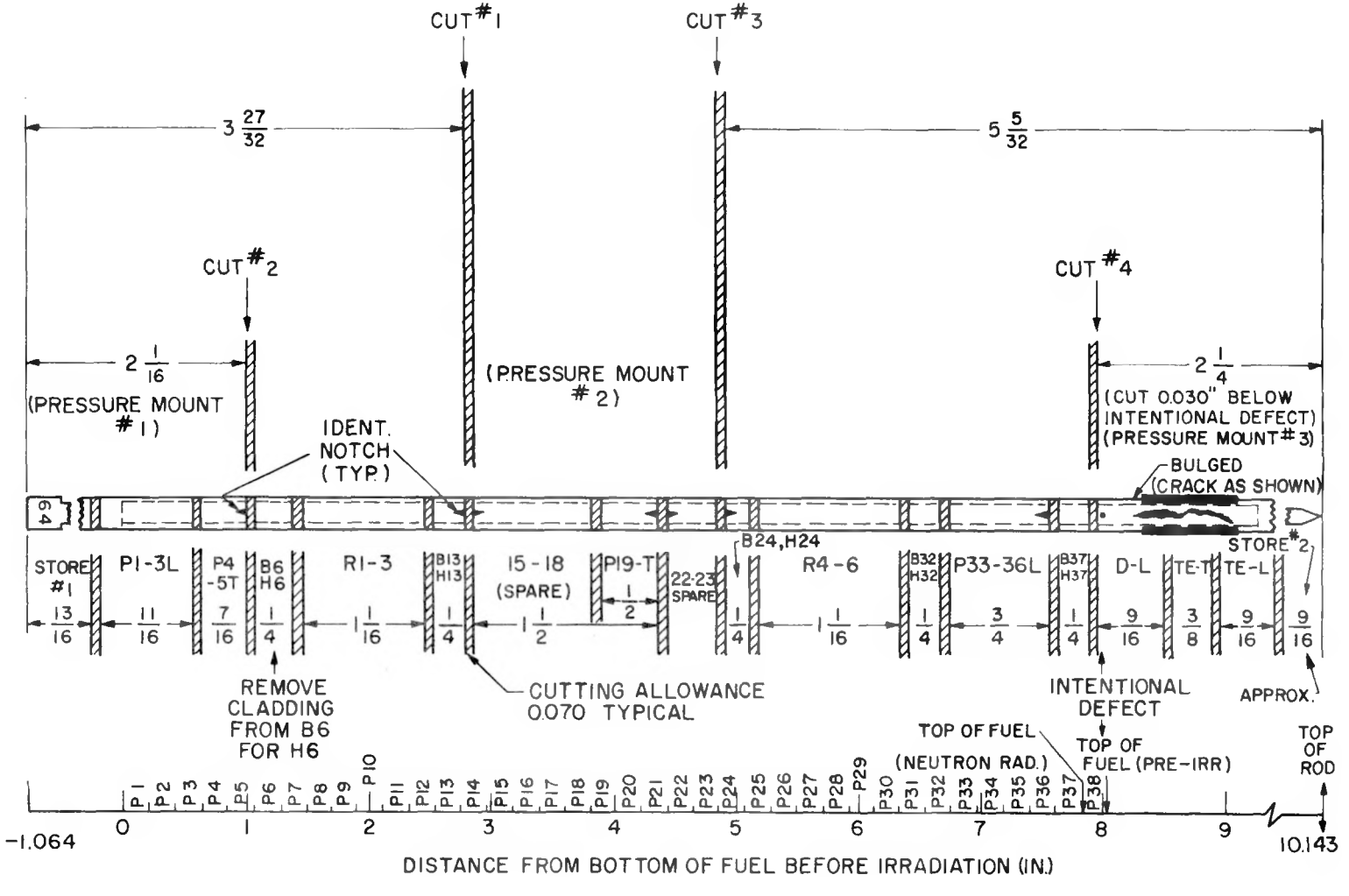

Figure 21. General Sectioning Sketch for Rod BETT 79-64D

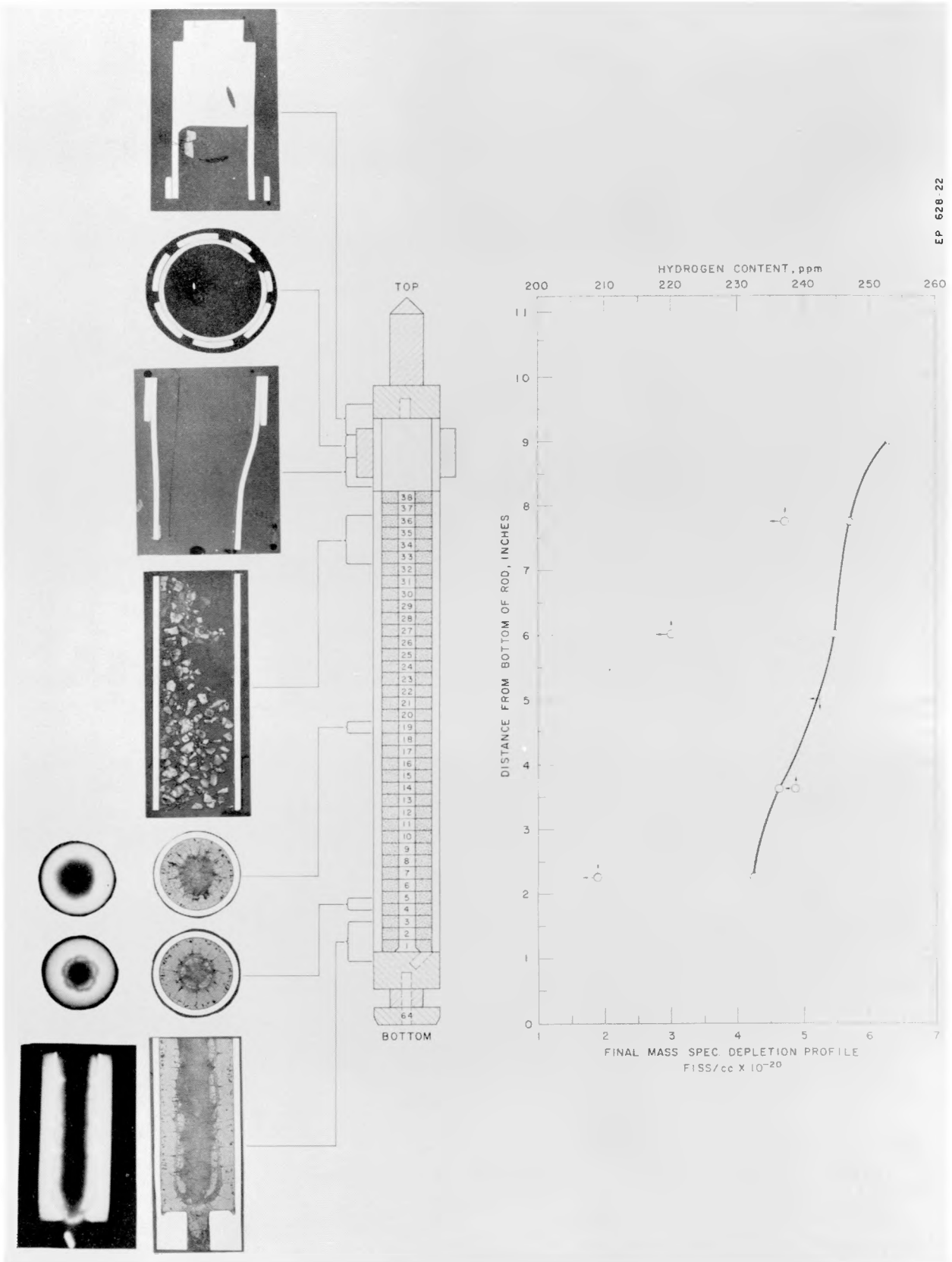

Figure 22. Fuel Structure Profile, Fission Product Concentrations Fuel Depletion Profile, and Cladding Hydride Analysis Profile for Rod BETT 79-64D

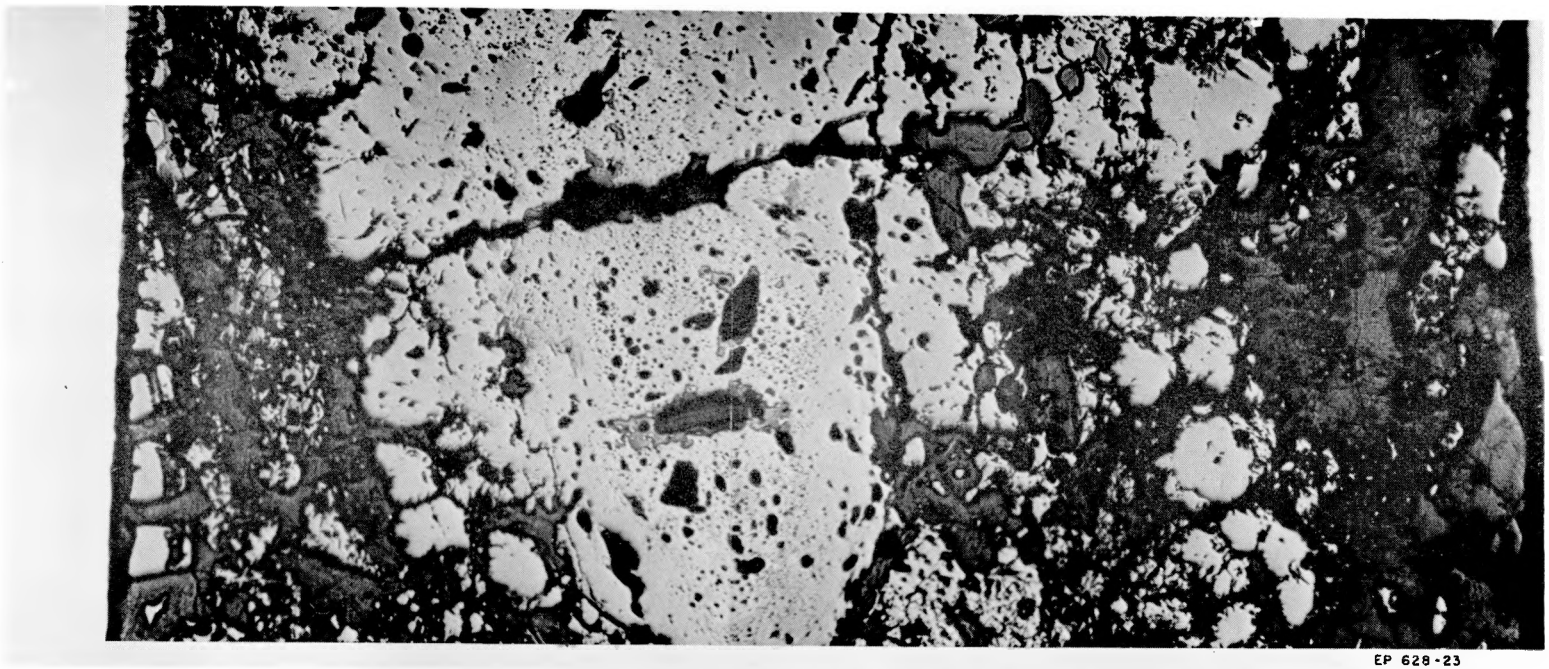

Figure 23. Typical Broken Fuel that was Seen in Pellets 33-36 at the Top of the Fuel Stack. X68

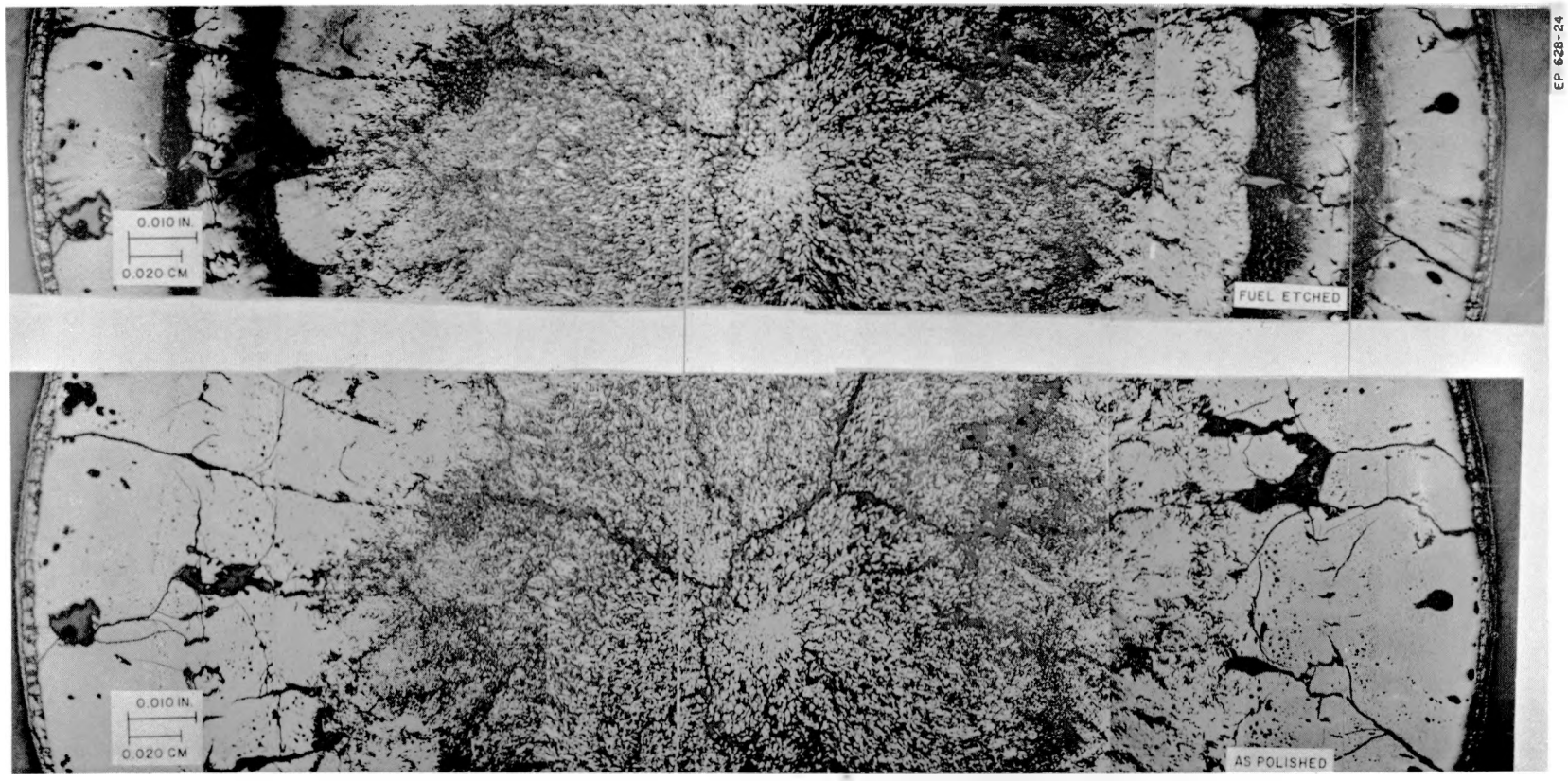

Figure 24. Typical Etched Fuel Structure as Seen in Pellet 19 which Shows Rings of Densified Material

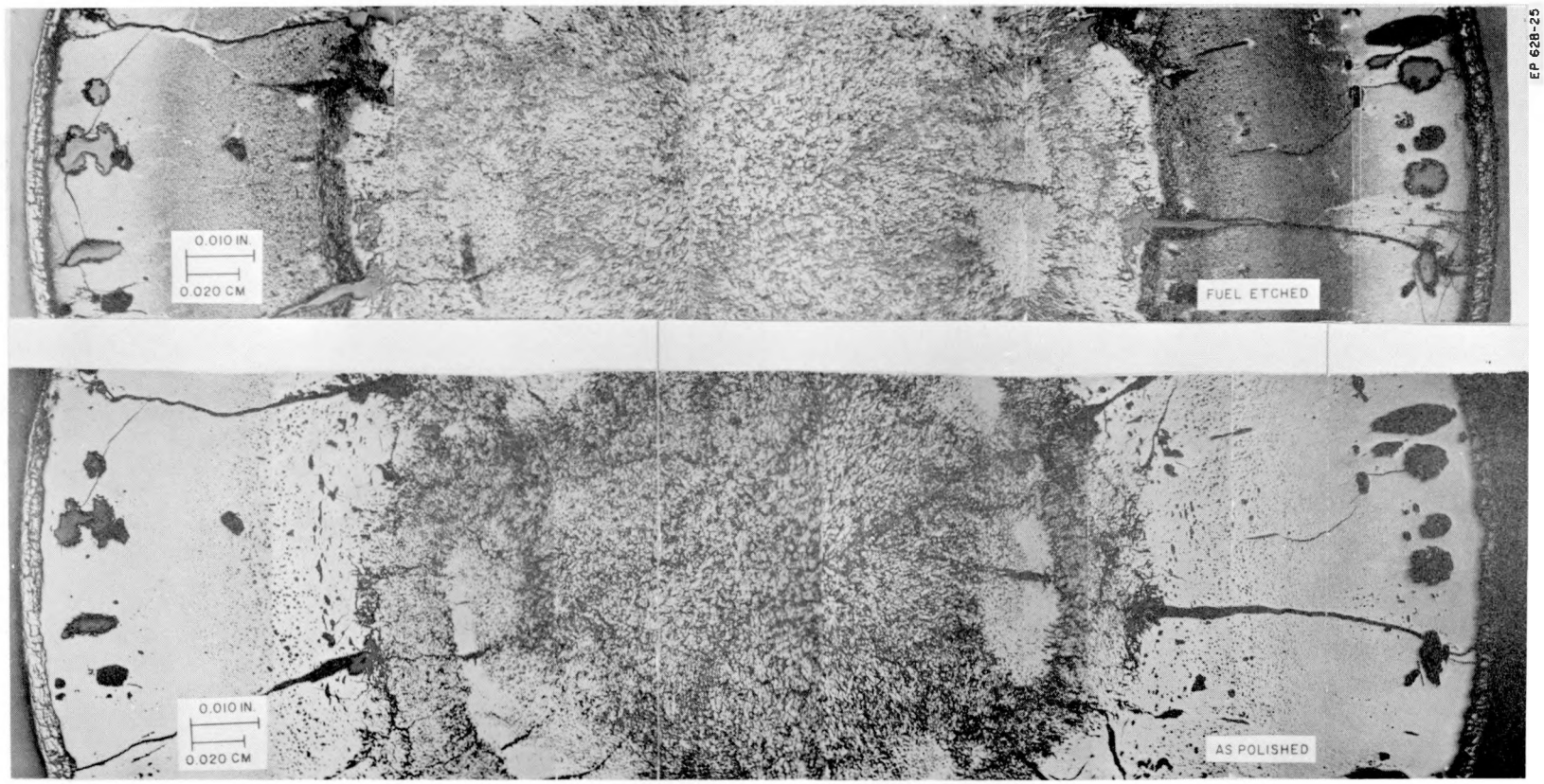

Figure 25. Fuel Structure from Pellet 5. Cladding Removed to Prepare Sample for Etching

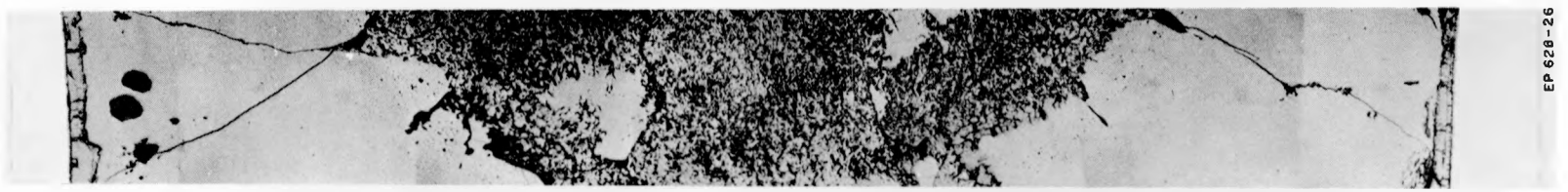

Figure 26. Characteristic "Crucible" Shape Seen in Molten Rods Illustrated by Pellet 1. X32

Figure 27. Hydride Concentrations in Alpha and Beta Phase Transition Region in the Upper End Cap. X56

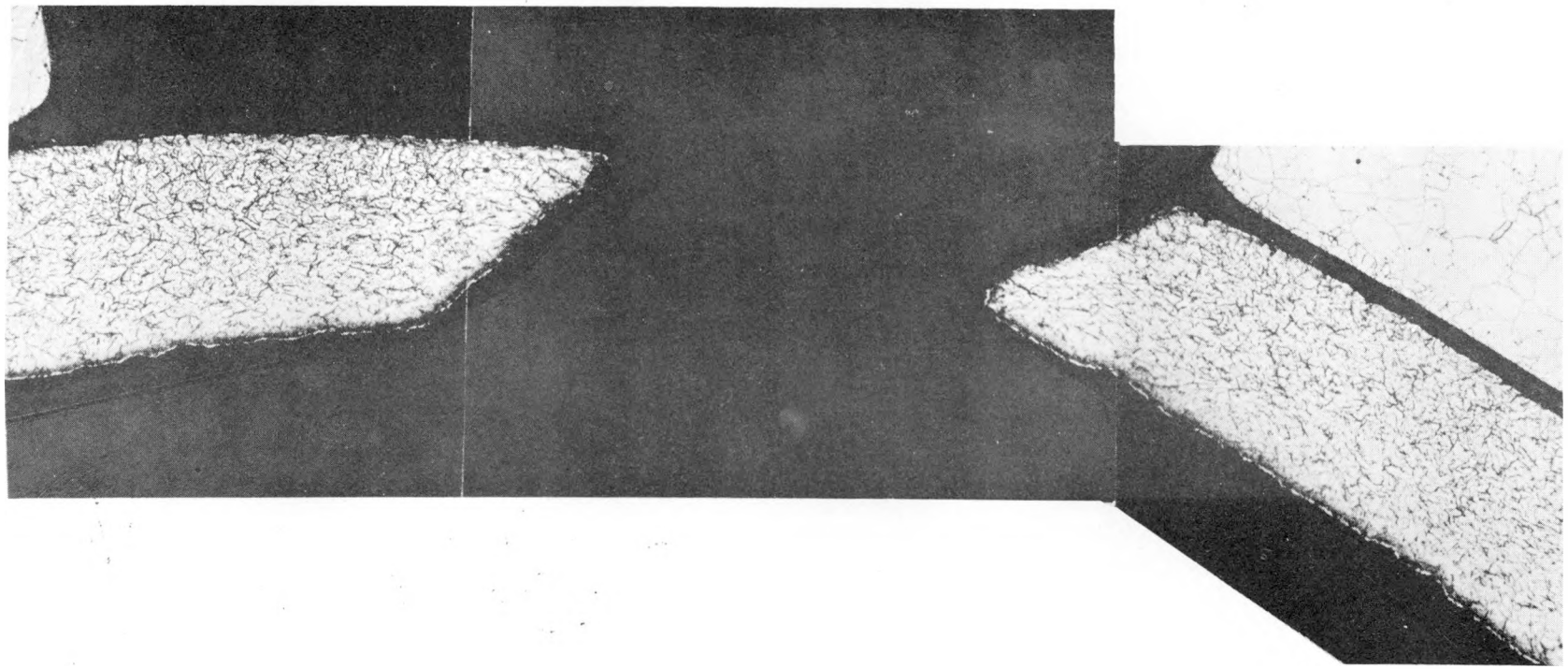

Figure 28. Hydride Concentrations of the Point of Clad Rupture. X85

Figure 29. Etched Structure of the Clad in the Plenum Region Where the Rupture Occurred. X26

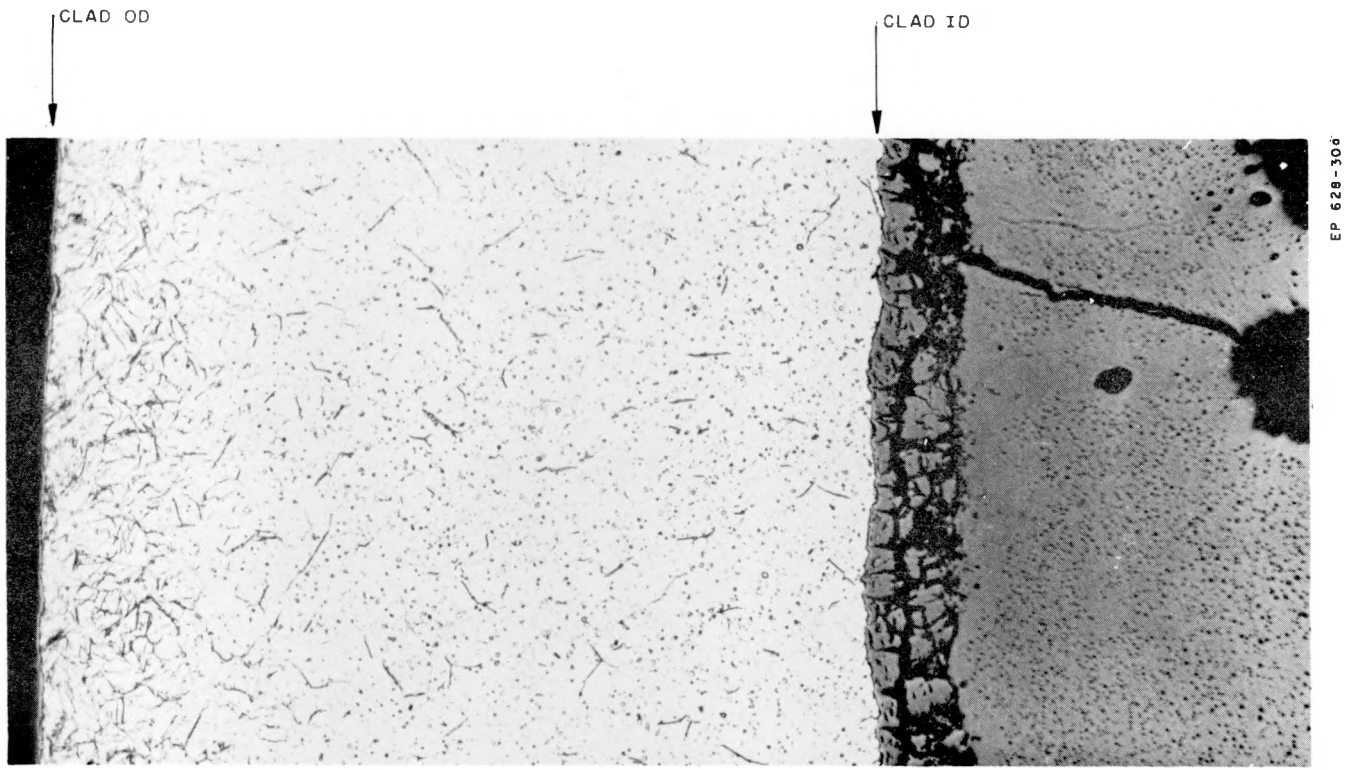

Figure 30a. Bright Field View of the Clad over Pellet 19 Showing Concentration of Hydride at the Clad Surface. This View is Typical of the Clad over all the Fuel Region. X250

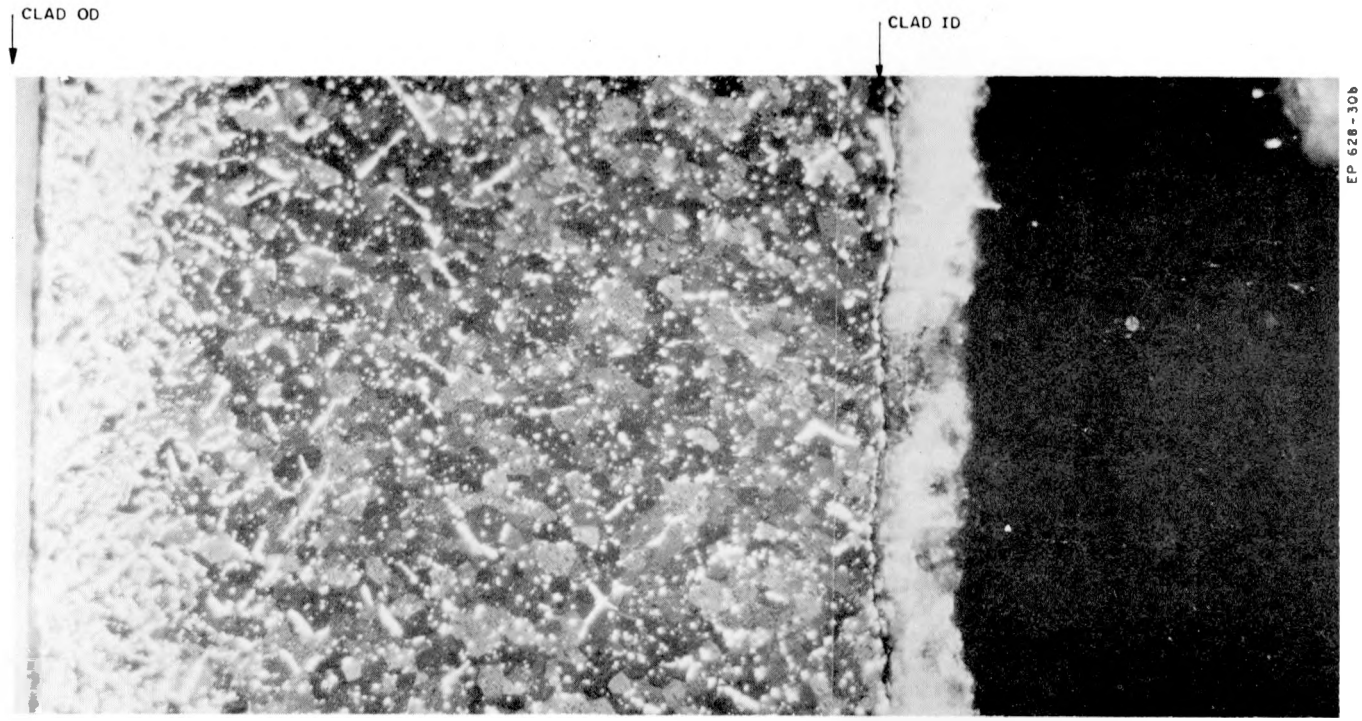

Figure 30b. The Same Area of Clad over Pellet 19 as Shown in Figure 30a but Using Polarized Light to Highlight the Hydride Concentration at the Clad OD. X250

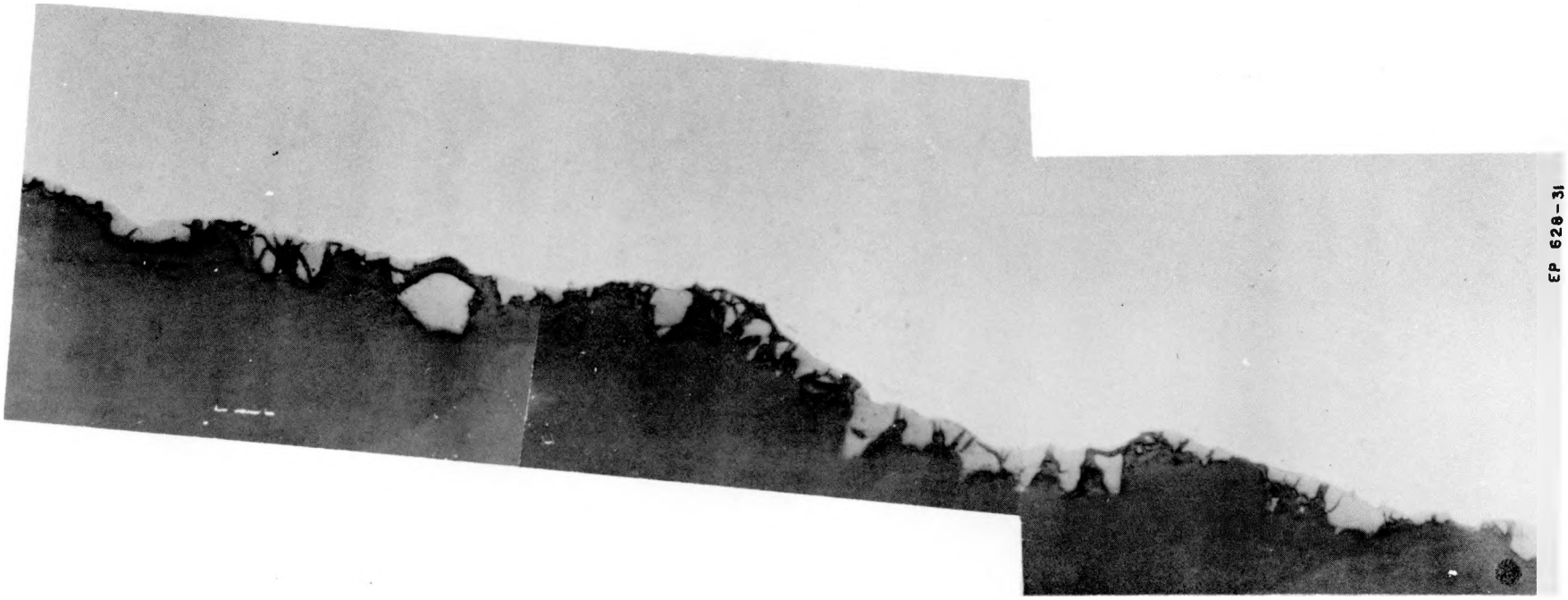

Figure 31. Typical Jagged Oxide Observed in the Plenum Region of the Rod.
X750

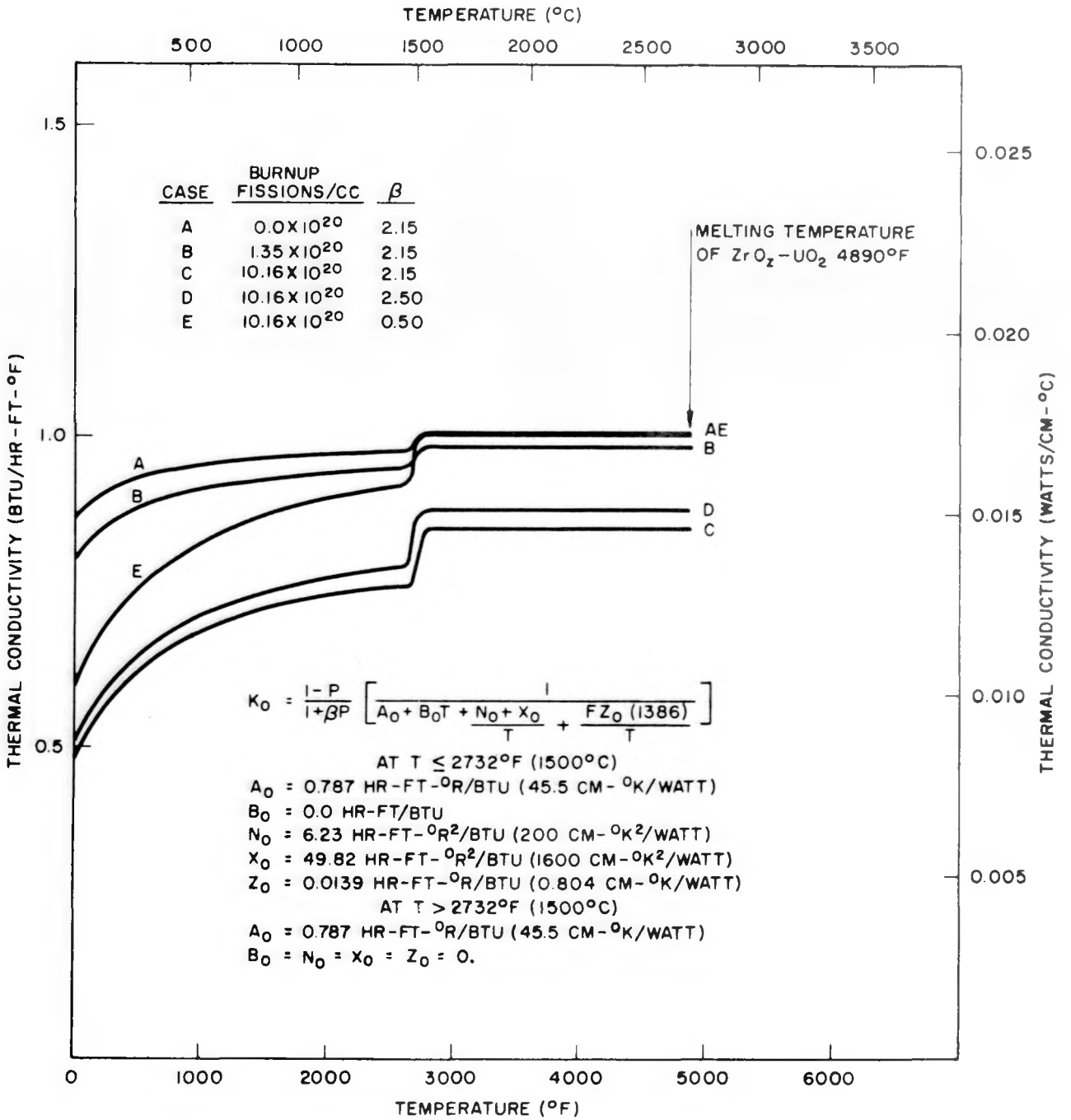

Figure 32. Thermal Conductivity versus Temperature for Rod BETT 79-64D

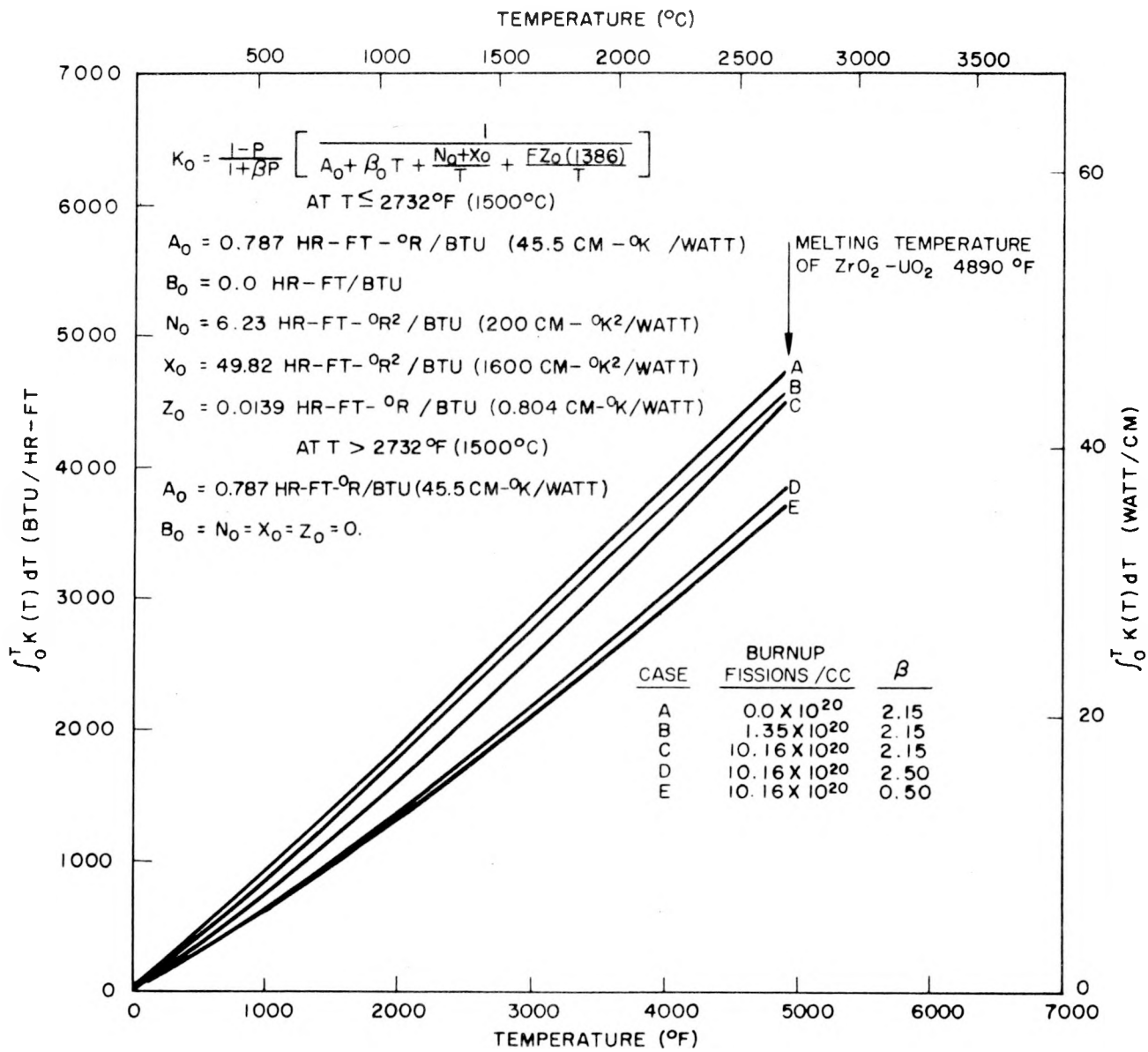

Figure 33. Integrated Thermal Conductivity versus Temperature Rod BETT 79-64D

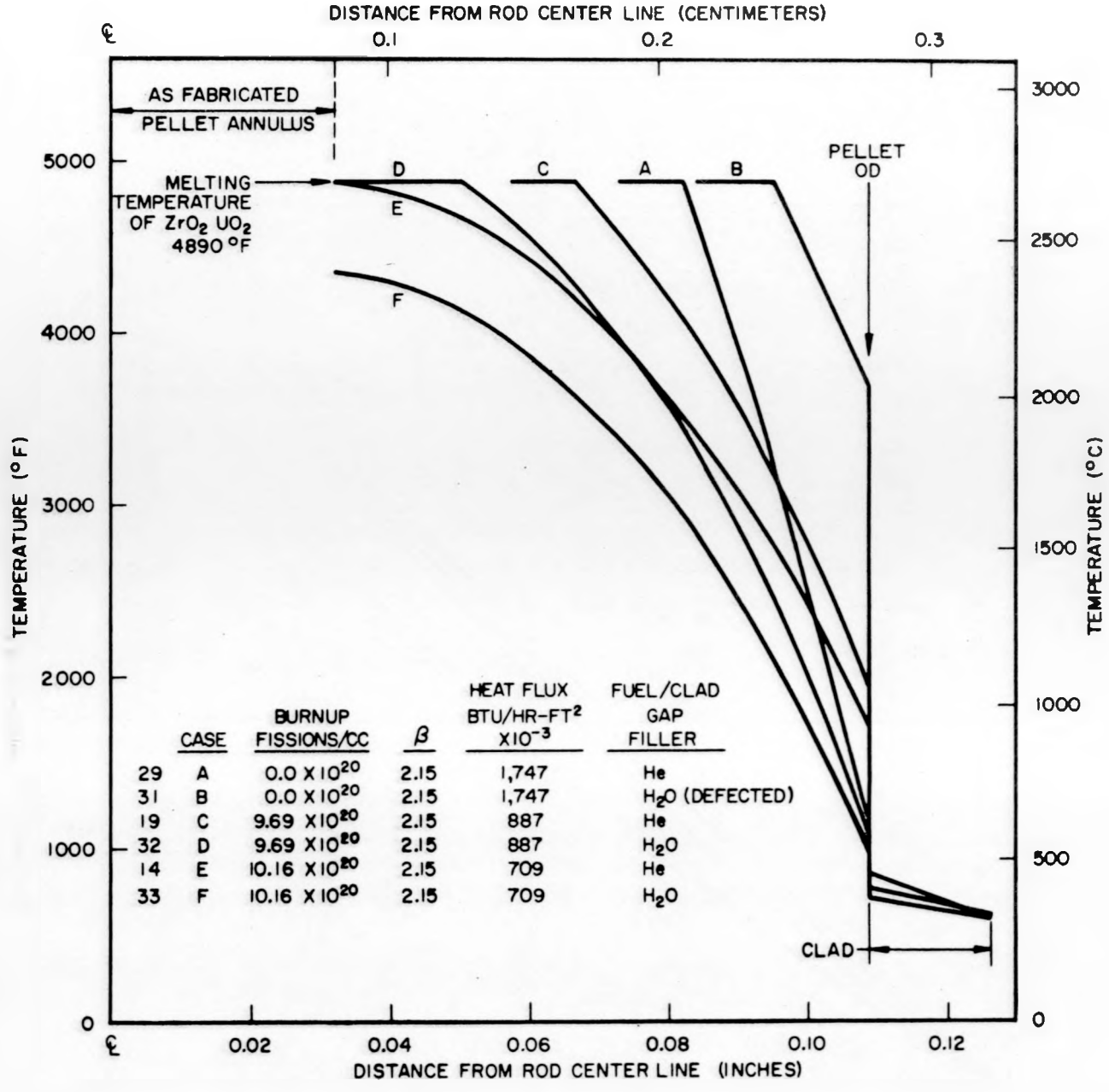

Figure 34. Temperature Profile for Rod BETT 79-64D Calculated from FIGRO Computer Program

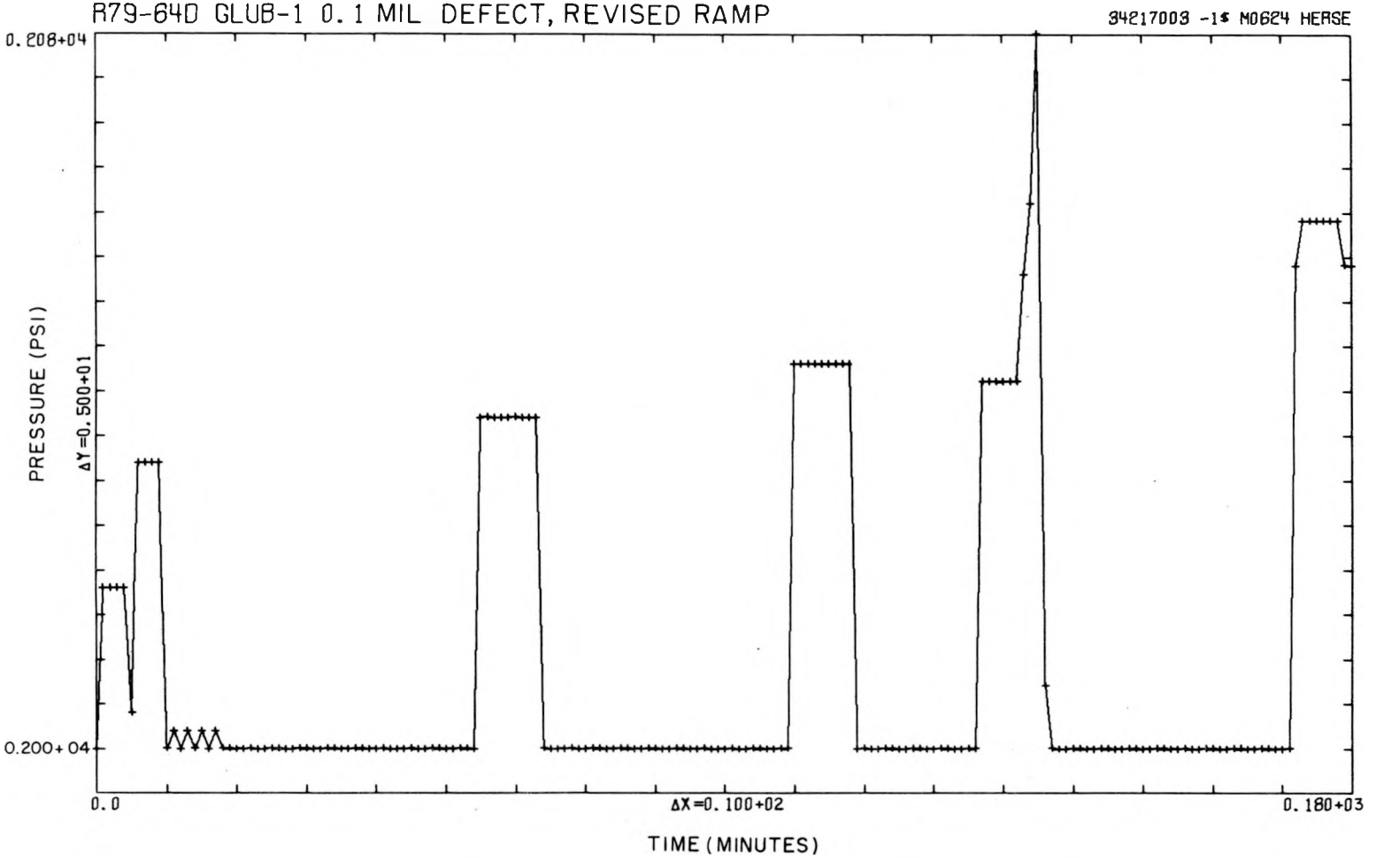

Figure 35. Internal Pressures in Rod BETT 79-64D with a 0.0001 Inch Diameter Defect Hole Calculated with GLUB-1 Computer Program

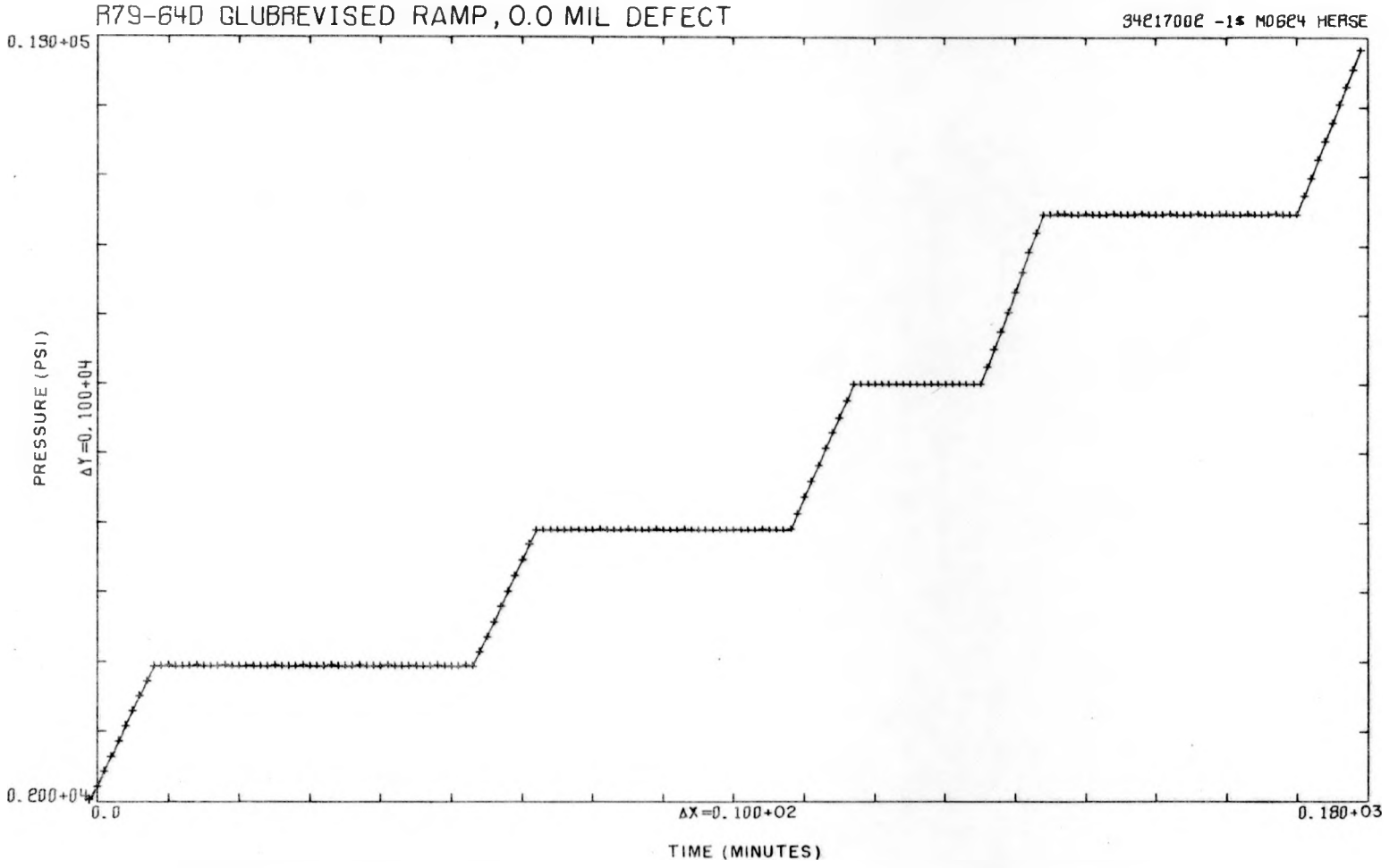

Figure 36. Internal Pressures in Rod BETT 79-64D with a 0.0000 Inch Diameter Defect Hole Calculated with GLUB-1 Computer Program

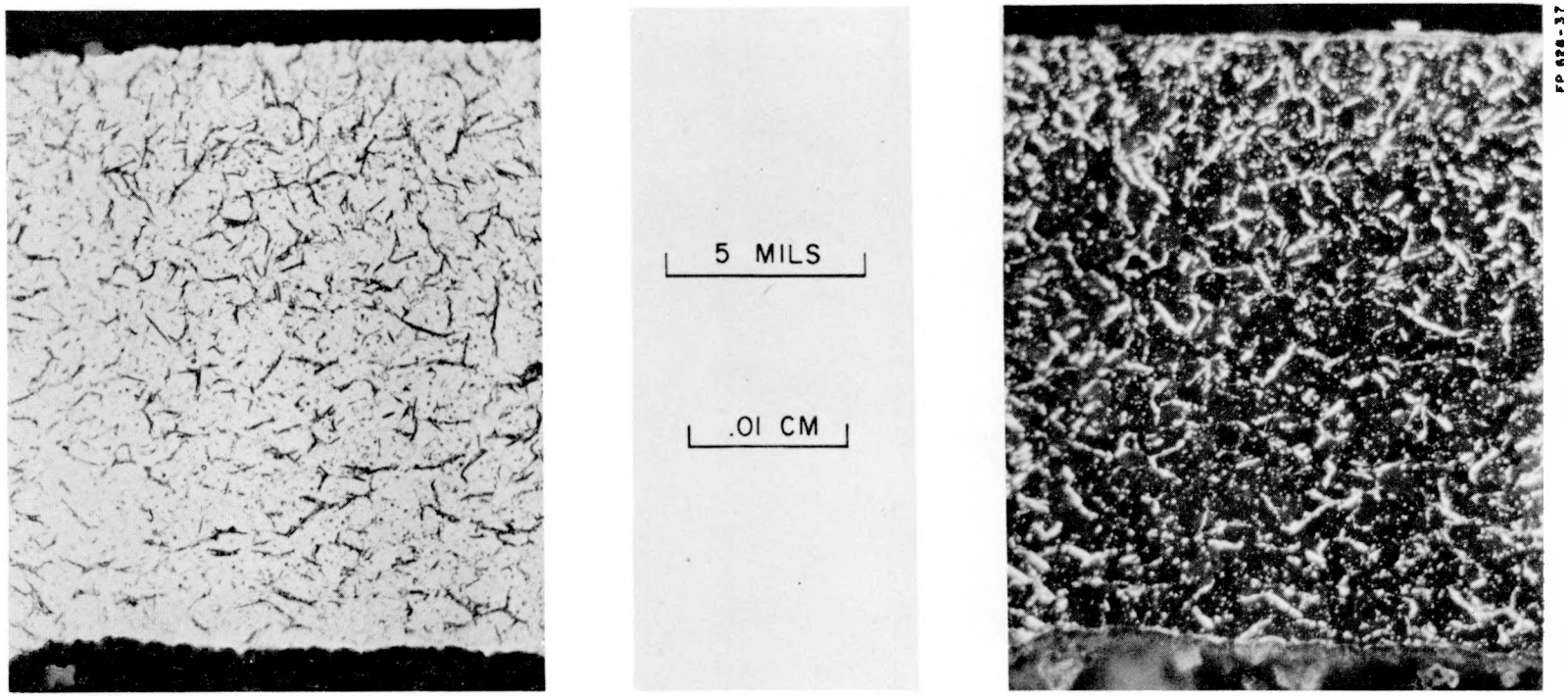

Figure 37. Typical Circumferential Hydride Orientation in Failure Region

APPENDIX A. PRE-IRRADIATION DATA

TABLE A-1. CHEMICAL ANALYSIS OF FUEL MATERIAL PELLET CHEMISTRY

Composition Geometry	ZrO_2 + 29.6 w/o U^EO_2 C.V.V.	
	Required	Actual
Processor	Bettis	Bettis
U^{234} w/o		1.05 ± 0.02
U^{235} w/o	93.0 ± 0.2	93.09 ± 0.08
U^{236} w/o		0.17 ± 0.02
U^T, w/o	26.1 ± 0.3	26.06
U^{+6}, w/o	0.5 max	
UO_2, w/o	29.6 ± 0.3	29.56
ZrO_2, w/o	70.4 ± 0.7	70.37
U^{238}, w/o		5.69 ± 0.06
Al, ppm	< 150	< 50
B, ppm	< 1	< 0.5
C, ppm	< 300	22
Cd, ppm	< 0.5	< 0.5
Co, ppm	< 10	< 10
Cr, ppm	< 75	< 20
F, ppm	< 30	< 10
Fe, ppm	< 300	< 50
Hf, ppm	< 150	
Mo, ppm	< 250	105
N, ppm	< 300	< 50
Ni, ppm	< 200	< 10
Si, ppm	< 500	50

TABLE A-2. AS FABRICATED FUEL PELLET DIMENSIONS AND DENSITIES

Rod BETT 79-64D — Fuel Comp. - ZrO_2-29.6 w/o $U^E O_2$ Fuel Geom. CVV

Bottom	Ident.	Pellet Diameter Max. (in.)	Pellet Diameter Min. (in.)	Pellet Diameter Avg. (in.)	I.D. Avg. (in.)	Length Avg. (in.)	Wt. (gm)	Vacuum Density (Incl. O.P.) g/cc	Vacuum Density (Incl. O.P.) Percent T.D.	Open Porosity Percent	Percent Pellet Void External to Fuel Matrix
1	6	-	-	0.2126	0.0629	0.2107	0.6866	6.43	92.0	5.0	12.9
2	7	-	-	0.2124	0.0630	0.2118	0.6908	6.44	92.1	4.7	12.8
3	9	-	-	0.2125	0.0630	0.2108	0.6870	6.42	91.9	5.0	12.7
4	11	-	-	0.2124	0.0631	0.2126	0.6890	6.40	91.5	5.6	12.8
5	13	-	-	0.2123	0.0634	0.2114	0.6862	6.42	91.9	5.3	12.9
6	15	-	-	0.2124	0.0631	0.2133	0.6937	6.42	91.8	5.2	12.7
7	20	-	-	0.2124	0.0631	0.2122	0.6944	6.44	92.2	4.8	12.5
8	21	-	-	0.2127	0.0633	0.2119	0.6842	6.40	91.6	5.9	13.4
9	22	-	-	0.2122	0.0632	0.2109	0.6853	6.43	92.0	5.2	12.8
10	25	-	-	0.2124	0.0632	0.2120	0.6909	6.43	92.0	5.4	12.8
11	26	-	-	0.2122	0.0631	0.2111	0.6891	6.43	92.0	5.4	12.5
12	27	-	-	0.2121	0.0631	0.2109	0.6830	6.42	91.9	5.8	13.0
13	28	-	-	0.2125	0.0629	0.2100	0.6819	6.42	91.9	5.7	13.1
14	29	-	-	0.2128	0.0631	0.2109	0.6809	6.43	92.0	6.0	13.9
15	30	-	-	0.2122	0.0631	0.2126	0.6946	6.44	92.1	5.0	12.5
16	31	-	-	0.2123	0.0631	0.2119	0.6893	6.49	92.8	4.7	13.5
17	32	-	-	0.2122	0.0632	0.2118	0.6821	6.42	91.9	6.0	13.6
18	34	-	-	0.2123	0.0633	0.2116	0.6808	6.42	91.8	5.8	13.6
19	35	-	-	0.2122	0.0633	0.2132	0.6899	6.43	92.0	5.9	13.2
20	36	-	-	0.2120	0.0633	0.2113	0.6866	6.45	92.3	5.3	13.0
21	37	-	-	0.2124	0.0630	0.2102	0.6870	6.47	92.6	4.9	13.1
22	39	-	-	0.2123	0.0631	0.2109	0.6871	6.47	92.5	5.0	13.1
23	40	-	-	0.2123	0.0634	0.2120	0.6846	6.47	92.5	6.1	13.9
24	45	-	-	0.2123	0.0633	0.2127	0.6890	6.42	91.9	5.6	13.1
25	50	-	-	0.2124	0.0631	0.2117	0.6932	6.49	92.9	5.1	13.1
26	52	-	-	0.2122	0.0633	0.2128	0.6830	6.39	91.4	6.7	13.3
27	53	-	-	0.2122	0.0631	0.2121	0.6931	6.47	92.6	5.0	12.9
28	54	-	-	0.2123	0.0633	0.2139	0.6893	6.42	91.8	6.1	13.5
29	55	-	-	0.2122	0.0632	0.2115	0.6829	6.40	91.6	5.9	13.1
30	57	-	-	0.2124	0.0630	0.2101	0.6833	6.45	92.3	4.9	13.2
31	58	-	-	0.2122	0.0630	0.2109	0.6876	6.49	92.8	4.2	13.3
32	59	-	-	0.2124	0.0633	0.2120	0.6799	6.42	91.8	5.8	14.0
33	61	-	-	0.2125	0.0633	0.2125	0.6901	6.44	92.1	5.4	13.2
34	62	-	-	0.2123	0.0633	0.2114	0.6832	6.39	91.4	6.3	12.9
35	63	-	-	0.2123	0.0635	0.2123	0.6761	6.34	90.7	7.4	13.5
36	66	-	-	0.2123	0.0632	0.2131	0.6901	6.49	92.8	4.6	14.0
37	67	-	-	0.2124	0.0632	0.2111	0.6841	6.44	92.1	5.5	13.3
38	68	-	-	0.2123	0.0631	0.2120	0.6862	6.44	92.1	5.4	13.3
Average				0.2124	0.0631	0.2117		6.43	92.0	5.2	13.2
Total							21.0961				
Dish Diameter (5 percent Sampling)				0.136 in (ave)							
Dish Height (5 percent Sampling)				0.0166 in							
Range				0.2122/0.2128	0.0629/0.0633				90.7/92.8	4.6-7.4	12.5-14

TABLE A-3. PROPERTIES OF ZIRCALOY -4 TUBE MATERIALS

Ingot Number	M-908 Rel. No. 987
Specification	ASTM-B-353-62
Tubing Properties	
H_2, ppm	22
N_2, ppm	26
Fe, percent	0.21
I.D. Avg.	0.21659
Std. Dev.	0.00057
Conc. Avg.	0.00088
Std. Dev.	0.00044
Internal Surface Conditions	Pickled
Density, gm/cm^3	6.543
Grain Size, ASTM No.	10.5
UTS, psi	81,200
Yield Strength, psi	55,800
Elongation, percent	23.5-24
Burst Test Results	
Temperature	R.T.
Pressure, psi	>11,900

TABLE A-4. PROPERTIES OF ZIRCALOY-4 END CAP MATERIAL

Ingot Number	OM 1597
Material Properties	
H_2, ppm	6-11
N_2, ppm	34-39
Fe, percent	0.19-0.24
Hardness	91 Rb
UTS, psi	(600 F Transverse) 32,740
Y.S., psi	22,315
Elongation, percent	41

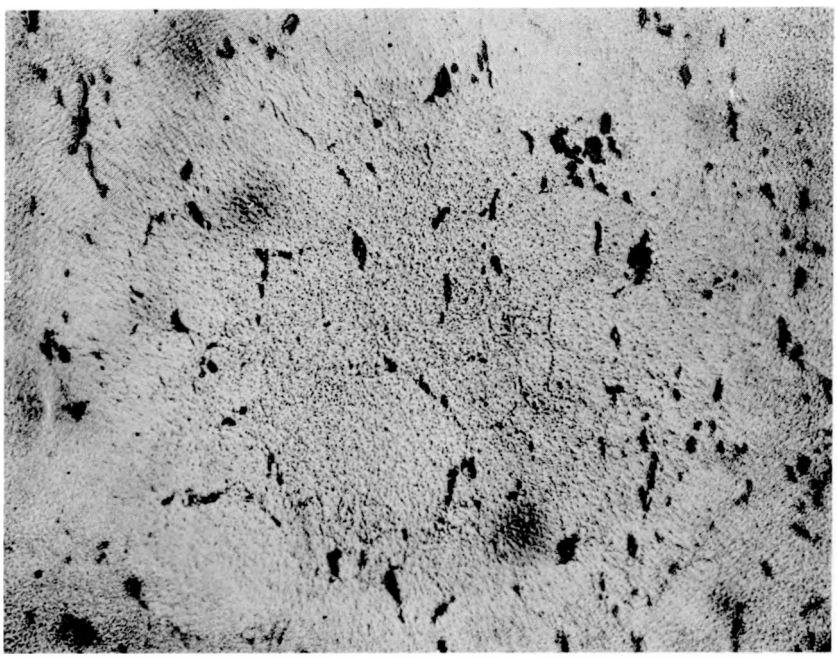

Figure A-1. Pre-Irradiation Microstructure of ZrO_2 + 29.6 w/o UO_2 Fuel-Combined Void Volume Pellets. 50X

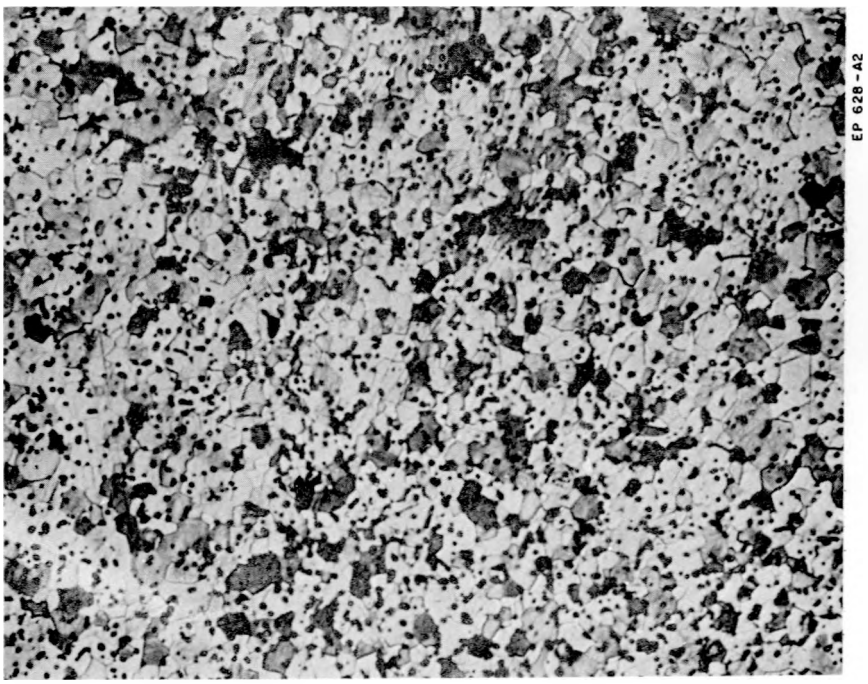

Figure A-2. Pre-Irradiation Etched Microstructure of ZrO_2 + 29.6 w/o UO_2 Fuel-Combined Void Volume Pellets. 400X

Figure A-3. Transverse Section of Tubing after Annealing at 1450 F, 4 Hours. ASTM Grain Size No. 6-8. 100X

APPENDIX B. INTERIM EXAMINATION DATA

Diameter measurements over the bulged region of rod BETT 79-64D were made on March 8 and March 30, 1965 (prior to clad rupture).

The bulge in the plenum chamber occurred in a region which was not characterized by pre-irradiation measurements. The absolute diameters were measured at ECF after the Inconel-X collar had been removed; the distance from the bottom of the rod and the corresponding measurements are illustrated in Table B-3. The pre-irradiation diameters over the bulged areas were estimated as an average between those of axial positions 11 (9.006 inches from the bottom of the rod) and 12 (9.715 inches from the bottom of the rod).

The diameter measurements at Bettis Laboratory were also made to characterize the extent of the bulge. The maximum bulge diameter was found to be located 9.249 inches from the bottom of the rod. Four diameters were then taken at this axial position, one along the "A" axis, one along the "B" axis which was 90 degrees from the "A" axis, and two were taken at radial positions of 45 degrees from the first two axes. The pre-irradiation diameters were also estimated as averages between those measured at standard positions 11 and 12 and as averages between the "A" and "B" axis. The results of this measurement are also given in Table B-3.

TABLE B-1. INTERIM EXAMINATION OPERATIONS

1. Pre-Decrud Visual Examination
2. Decrud
3. Cesium Leach or Fission Gas Leak Test
4. Post-Decrud Visual Examination
5. Diameter Measurements
6. Rod Surface Temperature Monitor
7. Length Measurement
8. Bow Measurement
9. Gamma Scan
10. Dry Weight

TABLE B-2. IRRADIATED FUEL ROD DIMENSIONS-DIAMETER

DIAMETERS-AXIS 1

INTERIM EXAM NO.		PRE-IRRAD.	1	2	3	4	5	6
DATE		4-30-64	6-22-64	11-16-64	12-14-64	3- 8-65	3-30-65	10-19-65
EFPD			10.7	78.8	88.5	112.4	112.4	121.2
FISS/CC(*10-20)			1.3	7.3	8.0	9.7	9.7	10.2
	POSIT(IN)	DIAM(IN)	DELTA	DELTA	DELTA	DELTA	DELTA	DELTA
	0.	0.	*	*	*	*	*	*
	.939	.2488	.3	-1.3	.9	1.0	.3	.3
	1.806	.2525	.4	-.6	1.2	2.1	2.0	2.0
	2.654	.2525	.2	.7	1.3	1.9	1.7	1.6
	3.502	.2526	.4	.7	1.4	1.7	1.2	1.6
	4.350	.2531	.2	.5	1.1	1.8	1.0	1.4
	5.198	.2530	.2	.3	1.0	1.7	1.2	1.5
	6.046	.2532	.3	1.0	1.0	1.7	1.5	1.7
	6.894	.2528	.2	.5	1.1	1.8	1.2	1.4
	7.742	.2516	.4	1.2	1.8	2.5	1.9	2.4
	8.590	.2528	.2	1.2	1.9	2.3	1.7	2.3
	9.006	.2527	.4	2.2	2.4	2.5	2.4	2.1
	9.715	.2526	*	*	*	*	9.7	*

INTERIM EXAM NO.		PRE-IRRAD.	1	2	3	4	5	6
DATE		4-30-64	6-22-64	11-16-64	12-14-64	3- 8-65	3-30-65	10-19-65
EFPD			10.7	78.8	88.5	112.4	112.4	121.2
FISS/CC(*10-20)			1.3	7.3	8.0	9.7	9.7	10.2
	POSIT(IN)	DIAM(IN)	DIAM(IN)	DIAM(IN)	DIAM(IN)	DIAM(IN)	DIAM(IN)	DIAM(IN)
	0.	0.	0.	0.	0.	0.	0.	0.
	.939	.2488	.2491	.2476	.2497	.2498	.2491	.2491
	1.806	.2525	.2529	.2519	.2537	.2547	.2546	.2545
	2.654	.2525	.2527	.2533	.2538	.2545	.2542	.2542
	3.502	.2526	.2530	.2534	.2541	.2543	.2538	.2542
	4.350	.2531	.2533	.2536	.2542	.2549	.2541	.2545
	5.198	.2530	.2532	.2533	.2540	.2547	.2542	.2545
	6.046	.2532	.2535	.2542	.2542	.2549	.2547	.2549
	6.894	.2528	.2530	.2533	.2539	.2546	.2540	.2543
	7.742	.2516	.2520	.2528	.2534	.2541	.2535	.2540
	8.590	.2528	.2530	.2540	.2547	.2551	.2545	.2550
	9.006	.2527	.2531	.2549	.2552	.2553	.2552	.2548
	9.715	.2526	0.	0.	0.	0.	.2623	0.

TABLE B-3. DIAMETER CHANGES MEASURED OVER BULGED REGION OF ROD BETT 79-64D

Measured at ECF, March 8, 1965, with DR-25B Optical Micrometer

Axis Track	Pos.(1)	Diameter, in. Pre-Irrad.	Diameter, in. 3-8-65	Diameter Change ΔD, mils (10^{-3} in.)
A (or) 1	9.006	0.25274	0.25554	+ 2.80
	9.167	0.25265(2)	0.27330	+ 20.65
	9.177	0.25265(2)	0.27340	+ 20.75
	9.187	0.25265(2)	0.27331	+ 20.66
B (or) 2	9.006	0.25279	0.25525	+ 2.46
	9.167	0.25269(2)	0.27433	21.64
	9.177	0.25269(2)	0.27425	+ 21.56
	9.187	0.25269(2)	0.27430	+ 21.61

Measured at Bettis Laboratory, March 30, 1965, with DR-25B Optical Micrometer

Radial Pos.(3)	Diameter, in. Pre-Irrad.	Diameter, in. 3-30-65	Diameter Change ΔD, mils (10^{-3} in.)
A	0.25265(2)	0.27341	+ 20.76
B	0.25269(2)	0.27497	+ 22.28
C	0.25267(4)	0.27412	+ 21.45
D	0.25267(4)	0.27405	+ 21.36

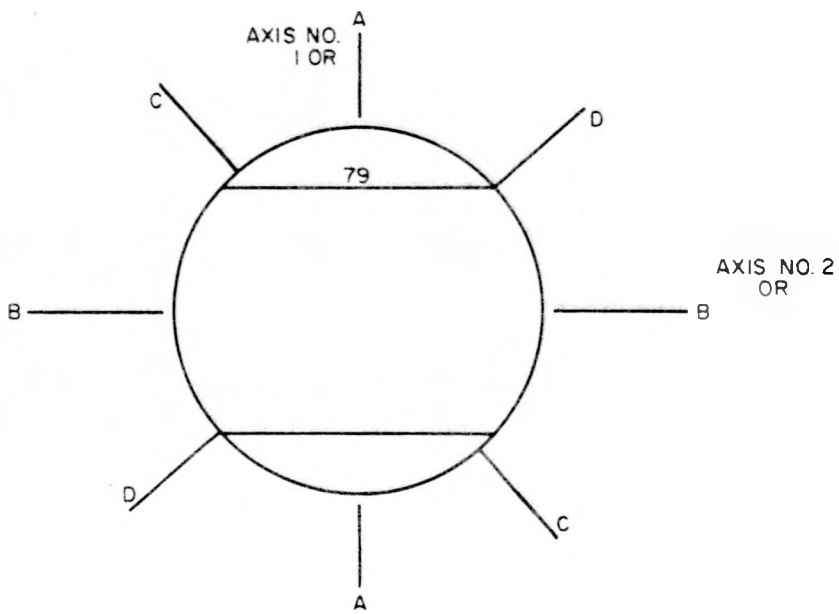

(1) Distance from bottom of fuel rod, in.
(2) Estimated as average diameter between position 11 and 12 an appropriate axis.
(3) Distance of maximum bulge diameter was 9.249 in. from bottom of rod Radial positions A, B, C, and D are identified on the above schematic
(4) Average diameters between radial positions A and B.

TABLE B-4. IRRADIATED FUEL ROD DIMENSIONS - LENGTH AND AVERAGE DIAMETER

LENGTHS

INTERIM EXAM NO.		PRE-IRRAD.	1	2	3	4	5	6
DATE		4-30-64	6-22-64	11-16-64	12-14-64	3- 8-65	3-30-65	10-19-65
EFPD			10.7	78.8	88.5	112.4	112.4	121.2
FISS/CC(*10-20)			1.3	7.3	8.0	9.7	9.7	10.2
	AXIS	DIST(IN)	DELTA	DELTA	DELTA	DELTA	DELTA	DELTA
	1	11.2088	6.2	12.2	10.0	6.9	6.6	-20.5
	2	11.2091	6.2	10.7	9.7	6.2	6.4	-20.7

AV. DIAMETER CHANGES(MILS) OVER LISTED LIMITS FOR SAMPLE 79-64D
DEVIATIONS AT 95 PERCENT CONFIDENCE LEVEL

	POS.LIMITS	1- 12		2- 11		2- 4		5- 11		5- 8		9- 12		3- 8	
	EXAM NO.	AVG.	DEV.	AVG.	DEV.	AVG.	DEV.	AVG.	DEV.	AVG.	DEV.	AVG.	DEV.	AVG.	DEV.
AXIS 1	1	.3	.1	.3	.1	.3	.1	.3	.1	.3	.1	.3	.1	.3	.1
	2	.6	.6	.8	.5	.3	.9	1.0	.5	.6	.3	1.5	.7	.6	.2
	3	1.4	.3	1.4	.3	1.3	.1	1.5	.4	1.0	.1	2.1	.4	1.1	.1
	4	1.9	.3	2.0	.2	1.9	.3	2.0	.3	1.7	.1	2.4	.1	1.8	.1
	5	2.2	1.4	1.6	.3	1.6	.5	1.6	.4	1.2	.2	3.9	3.9	1.3	.2
	6	1.7	.3	1.8	.2	1.7	.2	1.8	.3	1.5	.1	2.3	.2	1.6	.1
AXIS 2	1	.2	.1	.2	.1	.1	.4	.3	.1	.3	.0	.3	.3	.3	.1
	2	.7	.3	.8	.3	.7	.6	.8	.4	.6	.3	1.1	.7	.7	.3
	3	1.0	.3	1.1	.4	.9	.7	1.2	.4	.8	.2	1.6	.7	.9	.3
	4	1.6	.4	1.7	.4	1.4	1.2	1.8	.4	1.5	.1	2.1	.9	1.6	.5
	5	2.0	1.4	1.5	.4	1.3	1.1	1.5	.4	1.3	.2	3.7	3.8	1.4	.4
	6	1.2	.4	1.3	.4	1.3	1.2	1.3	.4	1.3	.2	1.4	1.0	1.4	.5

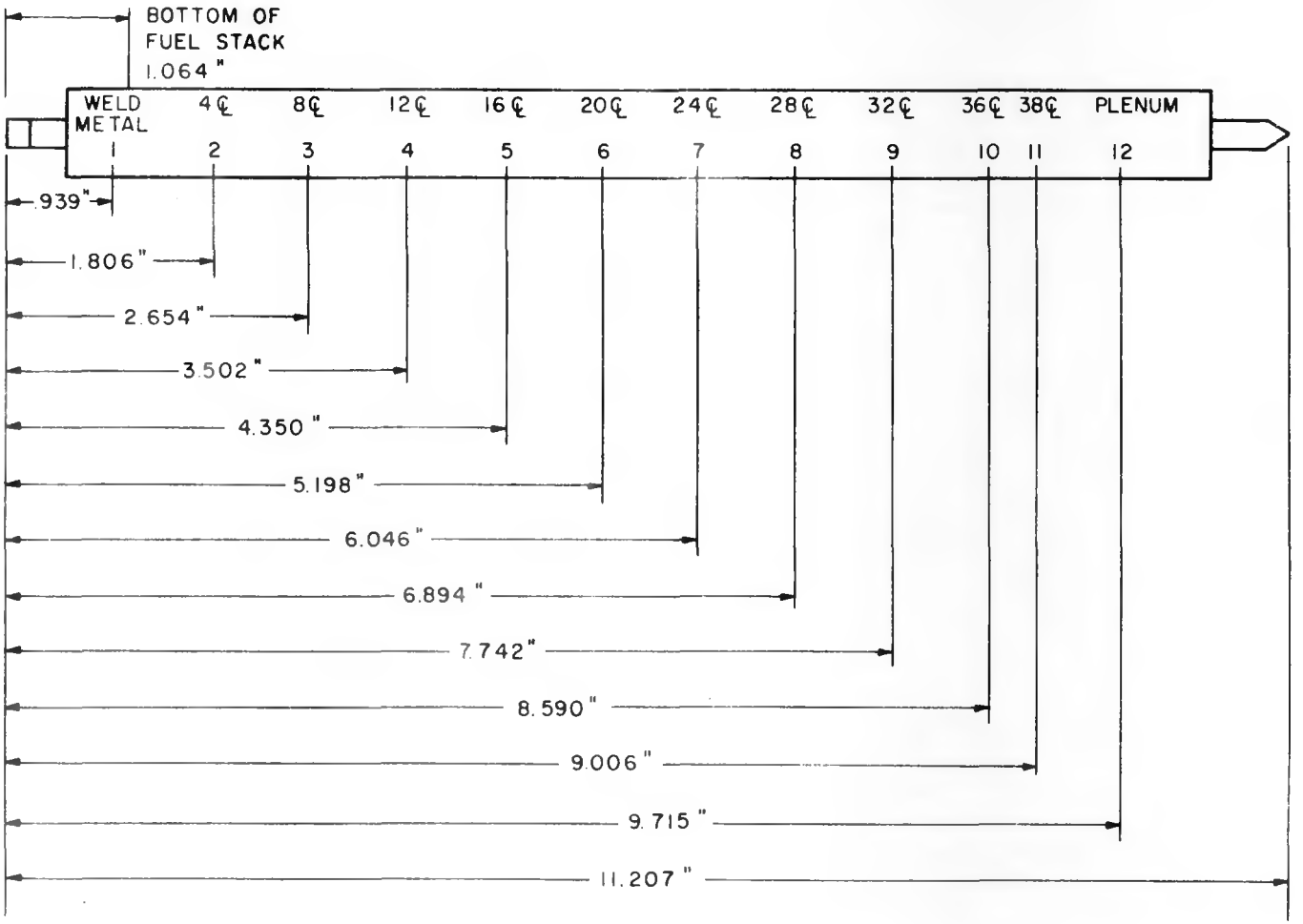

Figure B-1. Measurement Locations and Corresponding Pellet Positions for 11 Inch Long LWB Seed-Type Rods of the L12-14 Test

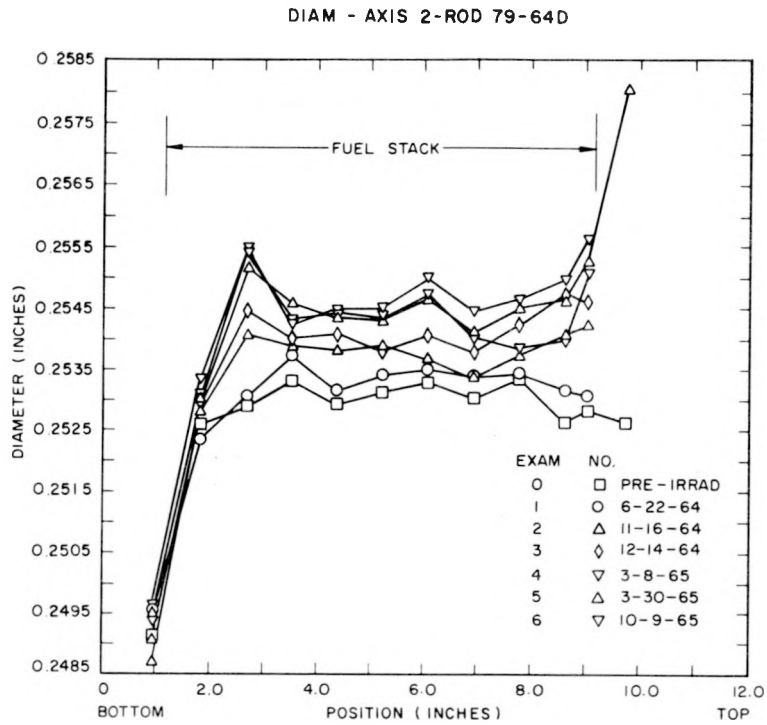

Figure B-2a. Diameter Changes for Rod BETT 79-64D Axis 2

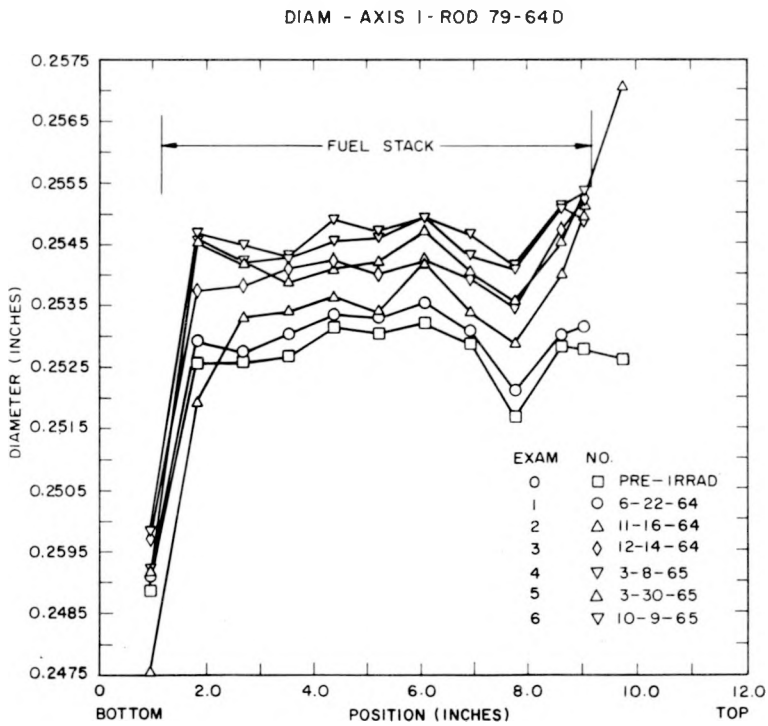

Figure B-2b. Diameter Changes for Rod BETT 79-64D Axis 1